UNIVERSIDADE FEDERAL DO CEARÁ
CENTRO DE TECNOLOGIA
DEPARTAMENTO DE ENGENHARIA DE TELEINFORMÁTICA
PROGRAMA DE PÓS-GRADUAÇÃO EM ENGENHARIA DE TELEINFORMÁTICA
DOUTORADO EM ENGENHARIA DE TELEINFORMÁTICA

DAYSE GONÇALVES CORREIA BANDEIRA

ORTHOGONAL TIME FREQUENCY SPACE MODULATION: CONTRIBUTION TO CHANNEL ESTIMATION AND DATA DETECTION IN A HIGH MOBILITY MULTIPATH WIRELESS ENVIRONMENT

FORTALEZA
2022

DAYSE GONÇALVES CORREIA BANDEIRA

ORTHOGONAL TIME FREQUENCY SPACE MODULATION: CONTRIBUTION TO CHANNEL ESTIMATION AND DATA DETECTION IN A HIGH MOBILITY MULTIPATH WIRELESS ENVIRONMENT

Tese apresentada ao Programa de Pós-Graduação em Engenharia de Teleinformática do Centro de Tecnologia da Universidade Federal do Ceará, como requisito parcial à obtenção do título de Doutora em Engenharia de Teleinformática. Área de Concentração: Sinais e Sistemas.

Orientador: Prof. Dr. João Cesar Moura Mota

Coorientador: Prof. Dr. Didier Le Ruyet

FORTALEZA
2022

Dados Internacionais de Catalogação na Publicação
Universidade Federal do Ceará
Sistema de Bibliotecas
Gerada automaticamente pelo módulo Catalog, mediante os dados fornecidos pelo(a) autor(a)

B165o Bandeira, Dayse Gonçalves Correia.
Orthogonal Time Frequency Space modulation : contribution to channel estimation and data detection in a high mobility multipath wireless environment / Dayse Gonçalves Correia Bandeira. – 2022.
147 f. : il. color.

Tese (doutorado) – Universidade Federal do Ceará, Centro de Tecnologia, Programa de Pós-Graduação em Engenharia de Teleinformática, Fortaleza, 2022.
Orientação: Prof. Dr. João Cesar Moura Mota.
Coorientação: Prof. Dr. Didier Le Ruyet.

1. OTFS. 2. Delay-Doppler domain. 3. Message passing. 4. Channel estimation. 5. FEM. I. Título.

CDD 621.38

DAYSE GONÇALVES CORREIA BANDEIRA

ORTHOGONAL TIME FREQUENCY SPACE MODULATION: CONTRIBUTION TO CHANNEL ESTIMATION AND DATA DETECTION IN A HIGH MOBILITY MULTIPATH WIRELESS ENVIRONMENT

Thesis presented to the Post-Graduation Program in Teleinformatics Engineering of the Center of Technology of the Federal University of Ceará, as a partial requirement for obtaining the title of Doctor in Teleinformatics Engineering. Area of Concentration: Signals and systems

Approved on: 28th October 2022

EXAMINATION BOARD

Prof. Dr. João Cesar Moura Mota (Advisor)
Federal University of Ceará (UFC), Brazil

Prof. Dr. Didier Le Ruyet (Co-advisor)
Conservatoire National des Arts et Métiers (CNAM), France

Prof. Dr. Charles Casimiro Cavalcante
Federal University of Ceará (UFC), Brazil

Prof. Dr. Kléber Zuza Nóbrega
Federal University of Ceará (UFC), Brazil

Prof. Dr. Marcello Luiz Rodrigues de Campos
Federal University of Rio de Janeiro (UFRJ), Brazil

Prof. Dr. Bartolomeu Ferreira Uchôa Filho
Federal University of Santa Catarina (UFSC), Brazil

To God, first of all, Who gives me strength to always move forward. To my husband Dennyson Bandeira, my daughter Danny and my family for their ability to believe in me. Their care provided me hope to follow.

ACKNOWLEDGEMENTS

I would like to extend my heartfelt gratitude to the following individuals and organizations, without whom the completion of this doctoral thesis would not have been possible:

Prof. Dr. João Cesar Moura Mota, my advisor, deserves special recognition for his exceptional guidance and the wealth of knowledge he imparted during this academic journey. I am profoundly grateful for the incredible opportunity he provided me to pursue a sandwich doctorate in Paris, France. This experience was a dream come true, and I owe it all to his support.

Dr. Didier Le Ruyet, my co-advisor, played a pivotal role in shaping the knowledge and content of this research. His important contributions were instrumental in the development of this thesis, and I extend my sincere thanks to him.

Dr. Kléber Zuza provided invaluable support in navigating the complexities of the finite element method, and I am deeply appreciative of his assistance.

To the professors who participated in the examining boards, for their valuable contributions and suggestions.

To my husband and best friend, Dennyson, I owe a debt of gratitude that words cannot adequately express. His unwavering companionship and support were vital in helping me find the time and energy needed for my research. Especially during the chaotic period following the birth of our daughter, Danny, amidst a pandemic and my return to work in another city, Dennyson stood by my side, offering unwavering encouragement. I love him more than words can convey.

To my daughter, Danny, your presence in my life has been a profound blessing. Balancing the roles of mother, professional, and student amid the constant challenges has made me stronger, and I am thankful for every moment with you.

My heartfelt appreciation goes to my parents, Zélia and Marcos Antônio, for their unwavering trust and support. They instilled in me from a young age the importance of education, especially for those not born into privilege.

I also wish to express my gratitude to my mother-in-law, Denise, and to my mother, once again, for their invaluable assistance, including caring for my daughter during her illnesses and when daycare was unavailable, enabling me to dedicate more time to my research.

I extend my thanks to all my professors who not only imparted knowledge but also exemplified the essence of education in the process of professional development. Their dedication to my growth and learning has left an indelible mark.

Lastly, I am grateful to the Coordenação de Aperfeiçoamento de Pessoal de Nível Superior (CAPES) for their financial support through the CAPES-COFECUB 830/15 Project, which made my doctoral research possible.

Each of these individuals and organizations has played a pivotal role in my academic and personal journey, and I am deeply appreciative of their contributions and support.

“Turn the stones you trip over into the stones of your stairs.”

(Socrates)

ABSTRACT

Data transmission in wireless systems brings numerous challenges, particularly in scenarios characterized by multipath propagation within rapidly changing channels in time. In this context, Orthogonal Time-Frequency Space (OTFS) modulation has recently emerged as a promising solution designed to operate effectively in doubly selective channels, encompassing variations in both time and frequency, even in high mobility scenarios. OTFS modulation entails the initial multiplexing of digital symbols in the Doppler-delay domain, subsequently transforming them into the time-frequency domain by Orthogonal Frequency Division Multiplexing (OFDM). Extensive research indicates that OTFS offers several performance advantages over conventional OFDM in many aspects, including a robust increase in data rates under high mobility conditions. Another advantage is the sparsity of the channel produced by OTFS, facilitating the utilization of low-complexity algorithms for accurate data detection. This thesis explores the performance of OTFS modulation within a doubly dispersive channel is evaluated in different versions of the message passing algorithm (MPA) in terms of computational complexity and bit error rate (BER). The findings reveal that MPA algorithms, especially their approximate versions (AMP), such as Expectation Propagation (AMP-EP) demonstrate superior performance. However, when considering the trade-off between computational complexity and BER performance, AMP simplified first-order (AMP-First Order) emerges as the optimal choice for both known and estimated channels. Methods for channel estimation are used, including the Finite Element Method (FEM) and the Natural Cubic Splines Method, both presenting good tradeo-ff between channel estimation accuracy and complexity. Comparative analyses between OTFS and OFDM are conducted, highlighting the advantages of OTFS, particularly within macrocell channel environment.

Keywords: OTFS. Delay-Doppler domain. Message passing. Channel estimation. FEM.

RESUMO

A transmissão de dados em sistemas sem fio traz inúmeros desafios, particularmente em cenários caracterizados pela propagação de múltiplos caminhos em canais que variam rapidamente no tempo. Neste contexto, a modulação *Orthogonal Time-Frequency Space* (OTFS) emergiu recentemente como uma solução promissora projetada para operar eficazmente em canais duplamente seletivos, abrangendo variações tanto no tempo quanto na frequência, mesmo em cenários de alta mobilidade. A modulação OTFS envolve a multiplexação inicial de símbolos digitais no domínio atraso-Doppler, transformando-os posteriormente no domínio tempo-frequência por *Orthogonal Frequency Division Multiplexing* (OFDM). Extensas pesquisas indicam que o OTFS oferece diversas vantagens de desempenho em relação ao OFDM convencional em muitos aspectos, incluindo um aumento robusto nas taxas de dados sob condições de alta mobilidade. Outra vantagem é a esparsidade do canal produzido pelo OTFS, facilitando a utilização de algoritmos de baixa complexidade para detecção precisa de dados. Esta tese explora o desempenho da modulação OTFS dentro de um canal duplamente dispersivo e avaliado em diferentes versões do Algoritmo de Passagem de Mensagens (*Message Passing Algorithm* - MPA) em termos de complexidade computacional e *bit error rate* (BER). Os resultados revelam que os algoritmos MPA, especialmente suas versões aproximadas (*Approximate Message Passing* - AMP), como *Expectation Propagation* (AMP-EP), demonstram desempenho superior. No entanto, ao considerar o compromisso entre a complexidade computacional e o desempenho do BER, o AMP simplificado de primeira ordem (AMP-*First order*) surge como a escolha ideal para canais conhecidos e estimados. Métodos para estimação de canal são utilizados, incluindo o Método dos Elementos Finitos (MEF) e o Método das Splines Cúbicas Naturais, ambos apresentando uma boa compensação entre precisão e complexidade da estimativa de canal. São realizadas análises comparativas entre OTFS e OFDM, destacando as vantagens do OTFS, particularmente no ambiente de canais de macrocélulas.

Palavras-chaves: OTFS. Domínio atraso-Doppler. Passagem de mensagens. Estimação de canal. MEF.

LIST OF FIGURES

LIST OF TABLES

LIST OF ALGORITHMS

LIST OF ABBREVIATIONS AND ACRONYMS

3GPP	3rd Generation Partnership Project
4G	4th Generation
5G	5th Generation
AMP	Approximate Message Passing
AMP-EP	AMP simplified by Expectation Propagation
AMP-FO	AMP simplified by First-Order
AWGN	Additive White Gaussian Noise
B5G	Beyond 5th generation
BER	Bit Error Rate
BPIC	Bayesian Parallel Interference Cancellation
bps	bits per second
CIR	Channel Impulse Response
CP	Cyclic Prefix
CP-OFDM	Cyclic Prefix - OFDM
CRLB	Cramer-Rao Low Bound
CSI	Channel State Information
DAB	Digital Audio Broadcasting
DDP	Delay-Doppler Profile
DFT	Discrete Fourier Transform
DVB	Digital Video Broadcasting
FDM	Frequency Division Multiplexing
FEM	Finite Element Method
FFT	Fast Fourier Transform
FG-GAI	Factor Graph with Gaussian Approximation of Interference
FLOP	Floating-point Operations
FN	Factor Node
GSM	Global System Mobile
ICI	Inter-carrier Interference
IDFT	Inverse Discrete Fourier Transform
IFFT	Inverse Fast Fourier Transform
IMT	International Mobile Telecommunications

IoT	Internet of Things
ISFFT	Inverse Symplectic Finite Fourier transform
ISI	Inter-symbol Interference
LLR	Log Likelihood Ratio
LMMSE	Linear Minimum Mean Square Error
LTV	Linear Time Varying
MIMO	Multiple-Input and Multiple-Output
MMSE	Minimum Mean Square Error
mmW	millimeter wave
MPA	Message Passing Algorithm
MRC	Maximal Ratio Combining
NMSE	Normalized Mean Square Error
NN	Neural Network
NOMA	Non-orthogonal Multiple Access
ODE	Ordinary Differential Equation
OFDM	Orthogonal Frequency Division Multiplexing
OMP	Orthogonal Matching Pursuit
OTFS	Orthogonal Time-Frequency Space
PAPR	peak-to-average power ratio
PDE	Partial Differential Equation
PDF	Probability Density Function
PDP	Power Delay Profile
PSK	Phase Shift Keying
QAM	Quadrature Amplitude Modulation
QoS	Quality of Service
RE	Resource Elements
SFFT	Symplectic Sinite Fourier Transform
SISO	Single-Input and Single-Output
SNR	Signal to Noise Ratio
SPA	Sum-Product Algorithm
TDL	Tap Delays Line
TTI	Transmission Time Interval

UE	User Equipments
UMa	Urban Macrocell
UQ	Uncertainty Quantification
VN	Variable Node
WLAN	Wireless Local Area Network
WSSUS	Wide Sense Stationary Uncorrelated Scattering
ZF	Zero Forcing
ZP-OFDM	Zero Padding - OFDM

LIST OF SYMBOLS

Scalars	Lowercase or uppercase letters
Vectors	Lowercase boldface letters
Matrices	Uppercase boldface letters
j	Imaginary unit $\sqrt{-1}$
$\mathbb{C}$	Set of complex numbers
$\mathbb{R}$	Set of real numbers
$\mathbb{Z}$	Set of integer numbers
$(.)^T$	Transpose operator
$(.)^H$	Hermitian transpose operator
$(.)^*$	Conjugate operator
$(.)^{-1}$	Inverse operator operator
∇^2	Laplacian operator
$\|\|.\|\|$	Euclidean norm operator
$\|.\|$	Absolute value (complex magnitude)
$[\cdot]_M$	Module operator of size M
$E\{.\}$	Expected operator
$\delta(\cdot)$	Dirac delta function
$DFT(\cdot)$	DFT operator
$IDFT(\cdot)$	IDFT operator
$DIRIC(\cdot)$	Dirichlet Kernel function
$diag\{.\}$	Transforms an input vector into a diagonal matrix
$vec(.)$	Vectorizes the input array
$unvec(.)$	Reshapes a column vector into a matrix
$\otimes$	Kronecker product
$\{Re\}$	Real part of a complex number
$\{Im\}$	Imaginary part of a complex number

$\boldsymbol{F}_N$	Unitary DFT matrix of size $N \times N$
$\boldsymbol{F}_N^H$	Unitary IDFT matrix of size $N \times N$
$\boldsymbol{f}_n$	n^{th} column of $\boldsymbol{F}_N$
$\boldsymbol{I}_N$	Identity matrix of size $N \times N$
M	Number of subcarriers
N	Number of symbols per subcarriers in OTFS
T	Pulse duration
Δf	Subcarrier spacing
$sinc$	Function $sinc(x)$
q	Index for a QAM symbol in q^{th} subcarrier
$\boldsymbol{s}$	Transmitted signal vector
$\boldsymbol{s}_{cp}$	Transmitted signal vector with CP
$\boldsymbol{r}$	Received signal vector at receiver input
$\boldsymbol{R}$	Received signal matrix at receiver input
$\boldsymbol{y}$	Received signal vector at receiver output
$\boldsymbol{x}$	Transmitted symbol vector
$\boldsymbol{w}$	AWGN noise vector
$\hat{\boldsymbol{w}}$	Effective AWGN noise vector
L	CP Length
$\boldsymbol{L}$	Insertion CP matrix
$\boldsymbol{L}_R$	Deletion CP matrix
P	Number of paths
$\boldsymbol{H}_{eff}$	Effective channel matrix
$\hat{\boldsymbol{H}}_{eff}$	Estimated effective channel matrix
$\boldsymbol{H}$	CIR matrix
$\hat{\boldsymbol{H}}$	Estimated CIR matrix
w	Noise AWGN
σ_0^2	Variance of noise AWGN

σ_d^2	Variance of signal
$\boldsymbol{G}_{tx}$	Diagonal matrix of transmitted pulse
$\boldsymbol{G}_{rx}$	Diagonal matrix of received pulse
$\hat{\boldsymbol{x}}_{MMSE}$	Estimated symbols by MMSE
$\hat{\boldsymbol{x}}_{ZF}$	Estimated symbols by ZF
$\boldsymbol{X}$	Diagonal matrix of transmitted QAM symbols
$\boldsymbol{S}$	Diagonal matrix of transmitted symbols
$\boldsymbol{S}_{cp}$	Diagonal matrix of transmitted symbols with CP
$\boldsymbol{S}_{ofdm}$	Matrix of OFDM transmitted symbols
$\boldsymbol{R}_{ofdm}$	Matrix of OFDM received symbols before receiver
$\boldsymbol{Y}_{ofdm}$	Matrix of OFDM received symbols after receiver
$\boldsymbol{s}_{ofdm}$	Vector of OFDM transmitted symbols
$\boldsymbol{r}_{ofdm}$	Vector of OFDM received symbols before receiver
$\boldsymbol{y}_{ofdm}$	Vector of OFDM received symbols after receiver
$\boldsymbol{Y}$	Matrix of received symbols
$\boldsymbol{Y}^{FT}$	Vector of received symbols in time-frequency domain
$\boldsymbol{y}^{FT}$	Diagonal matrix of received symbols in time-frequency domain
$\boldsymbol{A}_e$	Elementary matrix
$\boldsymbol{b}_e$	Elementary vector
$\boldsymbol{A}$	Global matrix of the elements
$\boldsymbol{b}$	Global vector of the elements
$\boldsymbol{\varphi}$	Interpolation samples vector by FEM
ρ	Source value of poisson equation
$\boldsymbol{\Pi}^{l_i}$	Permutation matrix for modeling l^{th} delay shift of $i-th$ path
$\boldsymbol{\Delta}^{k_i}$	Diagonal matrix for modeling k^{th} Doppler shift of $i-th$ path
Δ	Damping factor
x_i	Variables nodes
f_j	Function nodes

$n(i)$	Set of factor nodes connected to the variable node x_i
$m(j)$	Set of variable neighbors connected to factor node f_j
$d_f(j)$	Degree of the function node f_j
$d_x(i)$	Degree of the variable node x_i
μ_{x_i}	Marginal probability for a variable x_i.
$\mu_{f_j \to x_i}$	Message from factor node f_j toward variable node x_i
$\mu_{x_i \to f_j}$	Message from the variable node x_i towards the factor node f_j
$z_{f_j \to x_i}$	Mean from the the factor node f_j towards the variable node x_i
$\nu_{f_j \to x_i}$	Variance from the the factor node f_j towards the variable node x_i
$\gamma_{x_i \to f_j}$	Variance messages from variables nodes x_i to factor nodes f_j
$\zeta_{x_i \to f_j}$	Mean messages from variables nodes x_i to factor nodes f_j
$\beta(x_i)$	Symbol belief
$\boldsymbol{\alpha}_s$	QAM symbols set
$\Lambda_{b \to l}$	LLR value from the transferred messages from the b^{th} factor node to the l^{th} variable node
Δf	Frequency spacing
B	Bandwidth of system: $B = M\Delta f$
T_L	Duration of guard interval
T_u	Duration of useful symbol
T	Duration of a frame
T_s	Sampling rate
τ_{rms}	Channel delay spread
T_c	Coherence time
B_c	Coherence band
h_i	Gain of i^{th} path of channel
Λ	Grid on frequency-time domain
l	Delay shift
$\tilde{l}_i$	Fractional delay shift

k	Doppler shift
$\tilde{k}_i$	Fractional Doppler shift
Γ	Grid on delay-Doppler domain
$\Delta\tau$	Delay resolution
τ_i	Delay spread of i^{th} path of channel
τ_{max}	Maximum delay spread
$\Delta\nu$	Doppler resolution
ν_i	Doppler spread of i^{th} path of channel
ν_{max}	Maximum Doppler spread
l_p	Pilot delay position
ν_p	Pilot Doppler position
$\sqrt{P_{PLT}}$	Pilot energy
$s(t)$	Transmitted signal in time domain
$s[m]$	Transmitted signal in discrete time domain
$s_{cp}(t)$	Transmitted signal in time domain with CP
$s_{cp}[m]$	Transmitted signal in discrete time domain with CP
$x_{q'n'}$	Complex QAM symbol for a subcarrier q' at a time instant n'
$x[m]$	Transmitted symbols in discrete time domain
$x_{cp}[m]$	Transmitted symbols in discrete time domain with CP
$X[q]$	Transmitted QAM symbols in discrete frequency domain
$\hat{X}[q]$	Estimated symbols in frequency domain
$X^{FT}[m,n]$	Transmitted symbols in frequency-time domain for the m^{th} subcarrier and the n^{th} number symbol
$X[l,k]$	Transmitted symbols in delay-Doppler domain for the l^{th} delay and the k^{th} Doppler shift
$X_{cp}[l,n]$	Transmitted QAM symbols in delay-time domain with CP for l^{th} delay and n^{th} time
$h[m]$	CIR in discrete time domain

$H[q]$	CIR in discrete frequency domain
$y[m]$	Received symbols in discrete time domain
$y_{cp}[m]$	Received symbols in discrete time domain with CP
$Y[q]$	Received QAM symbols in discrete frequency domain
$Y^{FT}[m,n]$	Received symbols in frequency-time domain for the m^{th} subcarrier and the n^{th} number symbol
$Y[l,k]$	Received symbols in delay-Doppler domain for the l^{th} delay and k^{th} Doppler shift
$r(t)$	Received signal in time domain
$r_{cp}(t)$	Received signal in time domain with CP
$r[n]$	Received signal in discrete time domain
$w(t)$	AWGN noise signal in time domain
$w[m]$	AWGN noise signal in discrete time domain
$g_{tx}[m]$	Transmitter filter in discrete time domain
$g_{tx}(t)$	Transmitter filter in time domain
$g_{rx}[m]$	Receiver filter in discrete time domain
$g_{rx}(t)$	Receiver filter in time domain
$h(\tau,\nu)$	Channel impulse response on delay and Doppler spread function
$h(\tau,t)$	Channel impulse response on delay spread and time function
$A_{\tau}(\tau)$	Power delay profile of the channel
μ_{τ}	Average delay spread
τ_{rms}	Delay root mean square
f_D	Doppler frequency
f_c	Carrier frequency
v	Relative velocity
c	Speed of light in vacuum
Υ	Positive value for threshold method
Z	Constellation size of QAM

CONTENTS

1 INTRODUCTION

The escalating demand for data rates, and User Equipments (UE) restricted to a limited electromagnetic spectrum for wireless communications makes the project requirements along the evolution of the generations more challenging. Notably, the success of 4th Generation (4G) networks is attributed to their ability to deliver high data rates to a substantial user base through the utilization of the Orthogonal Frequency Division Multiplexing (OFDM) modulation (CARMON *et al.*, 2015; DIXIT; KATIYAR, 2015).

OFDM, a specialized multicarrier modulation technique, is particularly well-suited for transmissions over dispersive channels, where distinct subcarriers exhibit orthogonality. This wideband modulation scheme effectively addresses the intricacies of multipath channels. It subdivides the wideband frequency-selective fading channel into numerous narrowband subchannels. When the number of subchannels is sufficiently large, each subchannel can be treated as flat, essentially enabling the simultaneous transmission of multiple narrowband digital signals within a wideband context. Nevertheless, OFDM encounters challenges, primarily stemming from its high peak-to-average power ratio (PAPR), which can result in in-band radiation and out-of-band distortion (HARDAS; POKLE, 2017; GOPIKRISHNAN *et al.*, 2009). Researchers diligently explored various techniques to mitigate these issues (ARORA; GUPTA, 2017; KIM *et al.*, 2018).

However, while OFDM found its place in 4G mobile systems, it exhibits vulnerability in scenarios characterized by time-varying channels with substantial Doppler spread, such as high-speed rail mobile communications (RAVITEJA, 2018). Remarkably, despite these shortcomings in high mobility scenarios, OFDM modulation was chosen for the 5th Generation (5G) due to its commendable complexity-performance trade-off (GERZAGUET *et al.*, 2017). In response to this, Orthogonal Time-Frequency Space (OTFS) modulation, recently introduced by Hadani et al., emerges as a promising solution tailored to channels characterized by high Doppler spread and time-varying conditions (HADANI *et al.*, 2017). OTFS modulation is well-positioned to address the requirements of 5G mobile systems, demanding higher data rates and enhanced user equipment speeds.

OTFS exhibits considerable advantages over OFDM in the context of doubly dispersive channels, as demonstrated in previous studies (WIFFEN *et al.*, 2018a; REYHANI *et al.*, 2017; ZEMEN *et al.*, 2017). delay-Doppler domain provides an alternative representation for modeling Linear Time Varying (LTV) channels arising from moving objects within multipath environments. To achieve this, the OTFS modulator disperses each symbol, such as Quadrature Amplitude Modulation (QAM), over a set of two-dimensional orthogonal basis functions spanning the frequency-time resources needed to transmit a burst. This basis function set is purposefully designed to accommodate the dynamics of time-varying multipath channels.

By employing two-dimensional transformations, OTFS effectively transforms a doubly dispersive channel into an almost non-fading channel within the delay-Doppler domain (MURALI; CHOCKALINGAM, 2017). Consequently, each symbol within a frame experiences nearly constant fading, resulting in significant performance improvements over existing modulation schemes that are susceptible to strong Doppler effects, such as OFDM. Additionally, given the typically limited number of physical reflectors with associated Doppler shifts and delays in multipath channels, channel modeling and estimation in the delay-Doppler domain require fewer parameters.

The impulse response of the channel in the delay-Doppler domain is inherently sparse, represented as a sparse matrix (SHEN *et al.*, 2019), This characteristic facilitates the utilization of low-complexity detection algorithms, such as the Message Passing Algorithm (MPA), and bears significance for channel estimation, prediction, and tracking (HADANI *et al.*, 2017).

The primary objective of this thesis is to investigate, assess, and compare various low-complexity MPA-based detectors designed for OTFS systems operating within time-frequency selective channels characterized by high Doppler shifts. This evaluation encompasses both the Bit Error Rate (BER) performance and complexity analysis of the considered algorithms. The algorithms under examination include: i) Factor Graph with Gaussian Approximation of Interference (FG-GAI) proposed in (SOM *et al.*, 2011) known for its linear complexity, making it particularly appealing for detection in large-dimension channels; ii) AMP (Approximate Message Passing) using Gaussian Approximation (AMP-GA), wherein probability messages are updated through mean and variance calculations between nodes iii) AMP simplified by Expectation Propagation (AMP-EP) and iv) AMP simplified by First-Order (AMP-FO), as proposed in (WU *et al.*, 2014).

Furthermore, given that the channel is typically unknown to the system in practical scenarios, we introduce an interpolation method distinct from the spline method presented in (DAS *et al.*, 2020). This method relies on one-dimensional finite element techniques to solve the Poisson equation, accounting for the waveform's characteristics, and effectively estimates the impulse response of the channel in the time domain.

1.1 State of the art of OTFS

The concept of OTFS modulation was first introduced by Hadani in 2016 (HADANI *et al.*, 2017) and since then, it has garnered substantial attention, resulting in numerous studies exploring its applications across various domains. These applications span vehicular communications (CHENG *et al.*, 2020; BLAZEK; RADOVIC, 2020; YUAN *et al.*, 2021b), millimeter-wave communication (AL., 2017; WIFFEN *et al.*, 2018a), satellite communication (AL., 2022; SHI *et al.*, 2022), mobile communication (AN; RYU, 2019; TUSHA *et al.*, 2022; LIU, 2020; ALBATAINEH *et al.*, 2020), underwater acoustic communication (BOCUS *et al.*, 2019; JING *et al.*, 2022), Internet of Things (IoT) networks (WU *et al.*, 2021; MA *et al.*, 2022), radar systems (RAVITEJA *et al.*, 2019; GAUDIO *et al.*, 2019; DEHKORDI *et al.*, 2022; KESKIN *et al.*, 2021), and Non-orthogonal Multiple Access (NOMA) (DEKA *et al.*, 2020; DEKA *et al.*, 2021; DING *et al.*, 2019; DING, 2020).

Many of the referenced works employ a rectangular pulse-shaping waveform that theoretically satisfies the conditions of orthogonality in both time and frequency. However, in practical implementations, these conditions are often challenging to meet due to Heisenberg's uncertainty principle. To address this limitation, numerous researchers have delved into the study of various waveforms within the context of OTFS. For instance, in (RAVITEJA *et al.*, 2018), the authors compare rectangular pulses with prolate spheroidal waveforms and propose a block-circulant matrix decomposition method for arbitrary pulse-shaping waveforms to facilitate reduced cyclic prefix OTFS. This work also introduces a vector analysis of the modulation, a methodology adopted in this thesis that simplifies OTFS implementation. Additionally, a circular Dirichlet pulse-shaped OTFS waveform is proposed in (TIWARI; DAS, 2019), which effectively reduces out-of-band radiation when compared to rectangular pulses in OTFS systems. In (WEI *et al.*, 2021), another approach is presented, involving the use of a Dolph-Chebyshev window either at the transmitter or at the receiver. This approach is particularly useful when channel state information is unavailable at the transmitter but can be estimated at the receiver, enhancing the sparsity of the channel in the delay-Doppler domain.

Numerous other applications and waveform shaping proposals exist for OTFS modulation, alongside receiver and transmitter designs for OTFS systems (SHAN; WANG, 2020; GE *et al.*, 2021; CAO *et al.*, 2021). However, the primary focus of this thesis is the evaluation of data detection techniques. Here, the emphasis is on low-complexity algorithms, capitalizing on the channel's inherent sparsity in the delay-Doppler domain. Additionally, a novel channel estimation method for OTFS is proposed, distinct from existing approaches found in the literature. Consequently, the subsequent subsections, 1.1.1 and 1.1.2, delve into these specific areas of study applied to OTFS modulation..

1.1.1 Data detection

Given the remarkable sparsity observed in OTFS systems, research pertaining to data detection focuses on the application of low-complexity algorithms. Among these, the MPA stands out, with variations such as Approximate Message Passing (AMP) gaining considerable attention. These variants aim to further reduce the computational complexity associated with the original MPA.

One noteworthy study on MPA-based detection was conducted by Raviteja at al. in their 2017 paper titled "Low-Complexity Iterative Detection for Orthogonal Time-Frequency Space Modulation" (RAVITEJA *et al.*, 2017). In this work, the authors adapt the MPA to compensate for inter-Doppler interference, thereby enhancing BER performance. The following year, they released another article along similar lines, this time addressing interference cancellation techniques (RAVITEJA, 2018). Besides providing a comprehensive mathematical analysis of OTFS, they developed a novel low-complexity message passing algorithm for joint interference cancellation and symbol detection. In both works, the authors demonstrate significant error performance advantages of OTFS over OFDM under identical channel conditions.

Towards the end of 2019, three works concerning data detection emerged. The first (CHENG *et al.*, 2019) presents a comparative study between the linear equalizers based on Zero Forcing (ZF) and Minimum Mean Square Error (MMSE) applied to a double block circulant feature of the OTFS channel representation in the delay-Doppler domain. The authors efficiently implement these equalizers using two-dimensional fast Fourier transforms and demonstrate that their proposal offers lower computational complexity without compromising performance when compared to other existing linear equalizers. The second work (YUAN *et al.*, 2019) introduces a simple variational Bayesian approach as an approximation of maximum a *posteriori* detection to reduce receiver complexity for OTFS. The authors illustrate the performance gains of this technique compared to conventional MPA. The third work (TIWARI *et al.*, 2019) introduces a low-complexity linear MMSE receiver that exploits the sparse structure of the OTFS channel matrix during the demodulation process through a factorization of singular matrices from the received signal. This proposed receiver achieves significant complexity reduction compared to conventional MMSE without any performance degradation.

From 2020 onwards, various novel proposals have emerged, including: 1. a low-complexity iterative rake detector proposed by (THAJ; VITERBO, 2020), which extracts and combines received multipath components in the delay-Doppler domain using a scheme similar to Maximal Ratio Combining (MRC). BER performance comparisons with MPA and MMSE demonstrate that the MRC detector can achieve similar performance as MPA but with lower complexity; 2. a low-complexity Neural Network (NN)-based detector developed from a Bayesian Parallel Interference Cancellation (BPIC) method as proposed in (KOSASIH *et al.*, 2022), and referred to as BPICNet; and 3. a 2D convolutional NN detector that employ data augmentation techniques based on MPA to enhance learning as proposed in (ENKU *et al.*, 2021). Results indicate that the NN-based approach outperforms conventional MPA with lower complexity. It is noteworthy that a majority of recent publications explore various low-complexity message passing algorithms (LI *et al.*, 2022a; WANG *et al.*, 2022; LONG *et al.*, 2022; LIU *et al.*, 2022).

1.1.2 Channel estimation

The literature already boasts a considerable number of publications addressing channel estimation within the OTFS system. From 2017 to 2022, approximately forty works have explored this topic across various scenarios and applications. These applications encompass millimeter wave (mmW) communication (LI *et al.*, 2022b; SRIVASTAVA *et al.*, 2022), radar systems (GAUDIO *et al.*, 2022), massive Multiple-Input and Multiple-Output (MIMO) setups (SHEN *et al.*, 2019; RAMACHANDRAN; CHOCKALINGAM, 2018; SHI *et al.*, 2021), and high-mobility mobile communication systems (DAS *et al.*, 2020; HASHIMOTO *et al.*, 2021), for example.

Many of the channel estimation techniques under investigation employ a pilot scheme. In this scheme, higher power is allocated to pilot points distributed across the delay-Doppler grid of transmitted symbols. A threshold-based method is often applied to facilitate the identification of scattered pilot samples within the received signal, taking into account the interference encountered when propagating through the doubly-selective channel. Once the scattered pilot points are recognized, the goal is to estimate the necessary parameters for channel estimation, following the adopted model's formulation.

The earliest works on channel estimation emerged in 2018 with the publication of Raviteja at al., titled "Embedded Pilot-Aided Channel Estimation for OTFS in Delay–Doppler Channels" (RAVITEJA *et al.*, 2019), though it was officially published in 2019. Since then, this study has garnered significant attention due to its straightforward approach and detailed mathematical explanations, which greatly facilitate comprehension. The method revolves around a simple arrangement of transmitted symbols, relying on just one pilot symbol positioned near the center of the delay-Doppler grid. The resolution of this pilot symbol depends on the number of subcarriers employed and the quantity of symbols utilized in the system. In this configuration, the pilot symbol is enclosed by guard symbols, and the remaining grid positions are filled with useful symbols. The symbols being transmitted, as these symbols propagate, they experience multipath scattering. The primary objective is to incorporate a sufficient number of guard symbols to identify scattered pilot symbol points within the guard region. This identification process provides information about delays, Doppler shifts, coefficient estimation, and tap counts. Subsequently, these estimates are used to model the channel based on the estimated parameters. The proposed threshold-based scheme plays a vital role in discerning the pilot symbol's spread within the grid.

Shen et al. (SHEN *et al.*, 2019) were among the pioneers in implementing a compressive sensing method based on the Orthogonal Matching Pursuit (OMP) algorithm. They introduced a channel estimation technique named "3D-structured orthogonal matching pursuit," designed to address downlink channel estimation, particularly in scenarios involving a substantial number of base station antennas within OTFS massive MIMO systems. The term "3D-structured" relates to the type of sparsity considered in this context: regular sparsity along the delay dimension, block sparsity along the Doppler dimension, and burst sparsity along the angle dimension. This approach effectively frames downlink channel estimation as a problem of sparse signal recovery.

Another innovative proposal for channel estimation through compressed sensing in practical environments, which the authors refer to as the "non-integer delay-Doppler domain," is presented in Gómez-Cuba's work (GóMEZ-CUBA, 2021). This approach relies on the OMP algorithm coupled with binary-division refinement. It aims to estimate delay and Doppler shifts within a continuous domain, substantially reducing estimation errors while maintaining reasonable computational complexity.

Jian Pan's work (PAN, 2021) takes a different approach by introducing the Cramer-Rao Low Bound (CRLB) estimation perspective. This perspective serves as a benchmark for evaluating various channel estimation algorithms within the framework of a discrete-time system model, focusing on non-ideal pulse-shaping OTFS scenarios. In this work, he derives the CRLB for channel estimation in both single cyclic prefix and multiple cyclic prefix cases, providing valuable insights into the achievable estimation performance.

Efforts to improve practical channel estimation, particularly in scenarios involving fractional Dopplers, have led to the development of various techniques aimed at better approximating the original channel while reducing estimation complexity. In one study (SHI *et al.*, 2021), authors propose a downlink Channel State Information (CSI) acquisition scheme for massive MIMO-OTFS systems, featuring a deterministic pilot design structured around a pilot matrix. This approach minimizes pilot overhead and memory consumption by employing a modified sensing matrix technique for channel estimation. Another work (HASHIMOTO *et al.*, 2021) tackles fractional Doppler scenarios with lower computational complexity than conventional channel estimation methods. Using a pseudo-random sequence in the delay-Doppler domain, this approach achieves performance comparable to conventional MMSE equalization with matrix inversion. In (LI *et al.*, 2021), channel gains and fractional Doppler shifts are estimated from identified pilots within the received signal. However, in (DAS *et al.*, 2020), the channel estimation under multiple fractional Dopplers performed in time domain is sparser than delay-Doppler domain channel matrix in the presence of fractional Doppler. For this comprehension, our study about channel estimation in the thesis, in Chapter 5, was based on this work, that is, in time domain, where the authors apply an interpolation method to obtain the estimation of the others channel coefficients from pilot samples of received signal.

Lastly, it is noteworthy that while previous proposals sought to minimize the use of pilot symbols within the delay-Doppler grid of transmitted symbols, Mishra et al. (MISHRA *et al.*, 2022) and Yuan et al. (YUAN *et al.*, 2021a) introduced a novel framework for channel estimation and data detection. Their approach involves superimposing low-powered pilots onto data symbols, effectively freeing up slots for pilots. This innovation leads to significantly improved spectral efficiency.

1.2 Motivation and objectives

Meeting the growing demand from users for high data rates and ensuring Quality of Service (QoS) guarantees in wireless communication systems represent significant contemporary challenges. Overcoming channel diversity within the constraints of limited bandwidth and available resources, particularly in high mobility scenarios, presents a complex undertaking.

Furthermore, the advent of 5G, an evolutionary step beyond 4G technology, introduces even more demanding requirements. While 5G aims to enhance data transmission rates, it extends its focus beyond mere speed enhancement. This technology introduces specifications that impact access infrastructure, consequently enabling new applications and services. Its objectives extend to connecting not only people but also objects, including the glsIoT.

Within the parameters defined by the International Mobile Telecommunications (IMT) for 5G, which encompass increased transmission rates and higher speeds, the new technology demands low latency, denoting the minimal time between transmission and network response. Additionally, it demands a higher density of connections, representing a surge in the number of devices interconnected within a given area. The pursuit of greater spectral efficiency is also crucial, implying an upsurge in the volume of data transmitted per unit of electromagnetic spectrum. Furthermore, there is an emphasis on enhanced energy efficiency, marked by reduced energy consumption and a resultant boost in sustainability.

Despite the selection of OFDM modulation for this new generation of wireless technology, it faces substantial challenges in terms of BER performance and spectral efficiency, especially when contemplating an evolution towards environments characterized by ultra-high speeds Beyond 5th generation (B5G). In this context, the OTFS modulation, as proposed by (HADANI *et al.*, 2017), emerges as a solution to tackle channel diversity, particularly in addressing Doppler and delay scattering. It offers the promise of achieving greater success in data recovery.

In light of this motivation, this thesis is dedicated to a comprehensive study of OTFS modulation, specifically focusing on BER performance within high-mobility multipath wireless systems. It involves the exploration of low-complexity detection techniques based on message passing, comparing them with linear techniques. Additionally, the thesis proposes a time-domain channel estimation methodology utilizing the Finite Element Method (FEM). This channel estimation approach aligns with an empirically tested and standardized channel model specified by the 3rd Generation Partnership Project (3GPP) for urban environments, particularly urban macrocells.

1.3 Methodology

The core of this work revolves around evaluating low-complexity detection techniques employing message passing and other approximations, even in comparison with linear filters. Additionally, the thesis proposes a novel channel estimation technique based on interpolation, utilizing a one-dimensional FEM approach, grounded in solving the Poisson equation within each subinterval to be interpolated. This approach differs from the one proposed by (DAS *et al.*, 2020), which relies on cubic spline interpolation and does not take into account the inherent nature of the signal. Notably, the proposed one-dimensional FEM, involving Ordinary Differential Equation (ODE) calculations, offers a less complex alternative.

Regarding detection techniques, owing to the high sparsity of the wireless channel's impulsive response, which effectively represents a channel matrix, capturing the input-output relationship of the system concerning delay and Doppler scattering associated with each multipath, this thesis conducts a comprehensive comparison of various message passing approximations, including an unprecedented study of OTFS with AMP-FO. The latter approach proves more advantageous, albeit with a cost-benefit analysis.

The methodology employed in this work relies on computer simulations conducted using the Matlab® program. These simulations are aimed at generating performance curves for BER concerning Signal to Noise Ratio (SNR) for the evaluation of detector algorithms. Additionally, the methodology involves generating curves for the Normalized Mean Square Error (NMSE) as a function of SNR, facilitating the assessment of channel estimation approximations, comparing the FEM method with cubic spline interpolation.

1.4 Scientific production and contributions

The thesis contributes to scientific knowledge and research through several publications and ongoing work:

- A published article in the Journal of Communication and Information Systems (JCIS) authored by D. G. C. Bandeira, D. L. Ruyet, M. Pischella and J. C. M. Mota: "Performance evaluation of low-complexity algorithms for orthogonal time-frequency space modulation," Vol. 35, No. 1, pp. 138-149, June 2020. DOI: 10.14209/jcis.2020.15.

- A published article in the proceedings of the XXXVIII Brazilian Symposium on Telecommunications and Signal Processing (SBrT 2020) authored by D. G. C. Bandeira, D. L. Ruyet, M. Pischella and J. C. M. Mota: "Study of low-complexity detectors for MIMO-OTFS systems". https://www.sbrt.org.br/sbrt2020/papers/1570649889.pdf.

- An article currently in preparation, authored by D. G. C. Bandeira, D. L. Ruyet, K. Z. Nóbrega and J. C. M. Mota: "Time domain channel estimation based on FEM-Poisson Method for orthogonal time-frequency space modulation under multiple fractional Dopplers", scheduled for release in 2023.

1.5 Work structure

The subsequent chapters of this thesis are structured as follows:

- **Chapter 2** - This chapter provides an extensive review of fundamental concepts within a wireless communication system, focusing on the influence of Doppler scattering and delay effects. It introduces a foundational model of the system and the associated channel, primarily in the context of a high-mobility urban environment. The chapter also expounds upon OFDM modulation, elucidating key principles such as orthogonality and Cyclic Prefix (CP). Furthermore, it presents empirical findings on the performance of OFDM within a high-mobility channel, incorporating linear equalizers.

- **Chapter 3** - This chapter delves into the essentials of OTFS modulation. It commences with a comprehensive survey of applications related to modulation and subsequently defines the core principles of processing in the delay-Doppler domain. The chapter introduces the concept of precoding, founded on the Symplectic Sinite Fourier Transform (SFFT), for QAM symbol allocation. Additionally, it outlines the system architecture employed in the modulation process. The chapter culminates with a vector analysis of OTFS and OFDM, underpinning the computational processing of the ensuing results.

- **Chapter 4** - This chapter unveils low-complexity algorithms rooted in message passing techniques. These algorithms are integral to the evaluation of BER performance for OTFS. The chapter's primary objective is to identify the algorithm that exhibits the optimal complexity-BER trade-off across the SNR range under scrutiny.

- **Chapter 5** - Within this chapter, the thesis takes on the subject of channel estimation, concentrating specifically on the time domain and employing interpolation methods. The results are presented through the measured NMSE of the urban macrocell channel, estimated using cubic spline interpolation and the proposed method, which employs FEM to solve Poisson's equation within each interpolation subinterval.

- **Chapter 6** - The concluding chapter offers a synthesis of the contributions made throughout the thesis and articulates the key conclusions drawn from the results presented herein. Moreover, it proffers recommendations for future research endeavors.

2 FUNDAMENTALS OF WIRELESS COMMUNICATION SYSTEM

The bedrock of wireless communication entails the transmission and reception of data via electromagnetic waves. Cellular technology, pioneered by Bell Laboratories during the 1960s and 1970s (MACDONALD, 1979; NOBLE, 1962), introduced the challenge of mobility. This implies that a user's receiving device must maintain a connection to the network, even when in motion. This challenge has intensified over time, driven by the demands of 5G and B5G networks.

Numerous global standards for mobile radio systems have been established. A comprehensive understanding of channel characteristics to mitigate interference is a pivotal tool in the realm of wireless communication solutions (ROHLING, 2011).

In the subsequent sections, we will delve into the system model in Section 2.1, followed by an exploration of wireless communication channel characteristics in Section 2.2. Here, we will elucidate the channel model's significance and the pivotal role of channel equalization in signal reception. Finally, Section 2.3 will provide an in-depth explanation of OFDM modulation, as it has held significant relevance across multiple generations of Global System Mobile (GSM) technology and has even been adopted for 5G networks.

2.1 System model

In a communication system, data bits resulting from message or information encoding undergo transmission via a physical medium known as a communication channel. This channel facilitates the propagation of data from the transmitter's output to the receiver's input. In the context of multicarrier systems, which is our focal point, the transmitter can be conceptualized as consisting of two primary components: one that converts input bits into data symbols, and another that modulates these symbols to impart robustness to the signal for transmission. The channel itself may encompass either guided communication (where the signal travels through a cable) or unguided communication (where the signal is emitted by an antenna and propagates through free space or wirelessly). At the receiver, the inverse process is executed for data retrieval. This involves demodulation of the received signal, followed by conversion of the demodulated symbols into data bits, which are subsequently decoded to reconstruct the original message.

Understanding the characteristics of the channel is of paramount importance in this process. This understanding aids in combatting signal interference during propagation and facilitates optimization of transmitter and receiver designs for the specific channel conditions to which the signal will be subjected. In our context, the study focuses on wireless systems, where the signal is transmitted from a transmitting antenna and, after propagating through a time-varying channel, it reaches a receiving antenna. Along this journey, the signal incurs delays (τ) and Doppler shifts (ν), associated to the multipaths of the trajectory.

Figure 1 serves as a general illustration of the system model for the wireless system under discussion. Here, $x[m]$ represents the transmitted symbols for each subcarrier m, and $s(t)$ signifies the transmitted signal following modulation. This signal experiences interference from channel $h(\tau, \nu)$. The interaction between the transmitted signal and the channel yields the received signal $r(t)$, which is subsequently demodulated by the receiver. The resulting received symbols $y[m]$ are then converted into output bits.

Figure 1 – Basic wireless system model

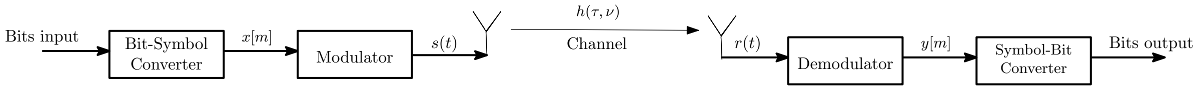

Source: adapted by author from (RAPPAPORT, 2002).

While Figure 1 can depict an ideal scenario when considering a single, direct line-of-sight path between the transmitter and receiver, the reality is far more complex due to electromagnetic wave propagation, which involves phenomena such as reflection, diffraction, and scattering. When multipath scenarios come into play, the situation becomes considerably more complex. According to (RAPPAPORT, 2002), the interaction of these waves induces multipath fading at specific locations, with wave strengths diminishing as the distance between the transmitter and receiver increases.

Furthermore, the channel introduces additional elements, including Additive White Gaussian Noise (AWGN) and potentially carrier frequency shifts if either the transmitter or receiver is in motion (Doppler effect). These complexities are exacerbated in high-mobility scenarios. Intersymbol interference, delay spread, and other forms of interference further contribute to the variability in link quality. A comprehensive understanding of these effects is imperative for applying techniques that can enhance data detection performance.

2.2 Wireless communication channel

According to (GOLDSMITH, 2005), electromagnetic signals experience random fluctuations over time when either the transmitter, receiver, or surrounding objects are in motion during wireless channel propagation. These fluctuations arise due to changing reflections and attenuation caused by phenomena such as reflection, refraction, and diffraction, which result in both power attenuation and phase variation of the transmitted signal (CHO *et al.*, 2010). These signal variations lead to a phenomenon known as multipath fading, which characterizes the random fluctuations in the envelope of the transmitted signal as it travels from the transmitter to the receiver.

Multipath fading occurs because multiple versions of the transmitted signal arrive at the receiver with different time delays. Each of these paths exhibits distinct characteristics, including amplitude, phase, time of arrival, and angle of arrival. These multiple signals may experience constructive or destructive interference at the receiver and can also cause Inter-symbol Interference (ISI) because the transmitted signal, arriving at different times, can overlap with one another (RAPPAPORT, 2002).

As per (TSE; VISWANATH, 2004), fading, or variations in channel strength over time and frequency, can be broadly categorized into two types:

- Large-scale fading: This type pertains to path loss or signal power decay with respect to distance and shadowing caused by large reflectors.

- Small-scale fading: This type deals with the constructive and destructive interference of multipath signals between the transmitter and receiver.

Furthermore, according to (TSE; VISWANATH, 2004), large-scale fading is more pertinent to concerns such as cell-site planning, whereas small-scale fading is of greater significance in designing reliable and efficient communication systems.

Modeling a channel for a specific study scenario, whether large-scale or small-scale, necessitates defining parameters that closely approximate the channel's characteristics through which the transmitted signal propagates. Among these parameters are the time scale and frequency of channel variation, known as coherence time and coherence bandwidth, respectively. These parameters are inherently linked to Doppler spread and delay spread, as explained below.

2.2.1 Delay spread and coherence band

Multipath fading can be described in two domains: the frequency response in the frequency domain and the impulse response in the time domain (YUAN, 2007). The impulse response of a multipath channel typically exhibits a delay spread, which is defined by considering a maximum excess delay (τ_{max}) that must be less than the inverse of the bandwidth. This is done to prevent ISI, which occurs when delayed multipath signals overlap with subsequent symbols. ISI can introduce significant errors, particularly in high-bit-rate digital systems (PROAKIS; SALEHI, 2008). The level of ISI increases as the transmitted bit rate rises.

As elucidated in Chapter 5, the two-dimensional delay-Doppler channel response, denoted as $h(\tau, \nu)$, can be derived from the two-dimensional delay-time varying response, $h(\tau, t)$ by applying a Fourier transform in the Doppler domain ν. . In this context, the values for the Channel Impulse Response (CIR) represent samples of a random process defined with respect to time t and multipath delay τ. Similarly to (GOLDSMITH, 2005) any random process, the general autocorrelation function is given by:

$$R_h(\tau_1, \tau_2; t_1, t_2) = E\{h(\tau_1, t_1)h^*(\tau_2, t_2)\}. \tag{2.1}$$

where t_1 and t_2 denote time instants, $\Delta t = t_2 - t_1$ is the time difference between instants, and τ_1 and τ_2 are delays associated with multipaths 1 and 2, respectively, composing the CIR multipath set, each associated with different scatterers.

Based on this generic autocorrelation function (Eq. (2.1)), we can narrow down the channel model to a specific category. In this instance, we consider the 2D delay-time response to be Wide Sense Stationary Uncorrelated Scattering (WSSUS), implying that it depends solely on the temporal difference of two time instants, and that there is no correlation between different multipath delays ($\tau_1 = \tau_2 = \tau$). Consequently, the channel is modeled as random using the autocorrelation function:

$$R_h(\tau;\Delta t) = E\{h(\tau,t_1)h^*(\tau,t_1+\Delta t)\}. \tag{2.2}$$

According to (GOLDSMITH, 2005), when $R_h(\tau;\Delta t) = R_h(\tau;0)$, Eq. (2.2) is denoted as the Power Delay Profile (PDP) of the channel. The PDP is a function that delineates the signal intensity received over a multipath channel as a function of propagation delays and can be expressed as:

$$A_h(\tau) = R_h(\tau;0) = E\{|h(\tau,t)|^2\}. \tag{2.3}$$

Then, the average delay spread μ_τ and its root mean square (rms) value are given by (GHOSH *et al.*, 2010):

$$\mu_\tau = \frac{\int_0^\infty \tau A_h(\tau)d\tau}{\int_0^\infty A_h(\tau)d\tau} \tag{2.4}$$

$$\tau_{rms} = \sqrt{\frac{\int_0^\infty (\tau-\mu_\tau)^2 A_h(\tau)d\tau}{\int_0^\infty A_h(\tau)d\tau}}. \tag{2.5}$$

where the largest non-negligible value of $A_h(\tau)$ is referred to as the maximum delay spread, τ_{max}.

Another crucial concept is the coherence bandwidth, which represents the range of frequencies where the channel exhibits nearly flat characteristics. In other words, for two frequencies, f_1 and f_2, located within the coherence bandwidth, the correlation between the channel's frequency responses at these frequencies is high. Therefore, the channel behaves very similarly at these frequencies in terms of gain and phase. A channel is considered frequency-selective if its frequency response undergoes significant changes within the transmitted signal's bandwidth, while it is considered flat fading if these changes are negligible. The coherence bandwidth B_c is defined as (RAPPAPORT, 2002):

$$B_c \approx \frac{1}{\tau_{max}} \approx \frac{1}{5\tau_{rms}}. \tag{2.6}$$

Hence, coherence bandwidth is inversely related to delay spread. A shorter delay spread corresponds to a larger coherence bandwidth. When the symbol duration significantly exceeds the delay spread, ISI can be expected to be minimal, ensuring effective communication.

2.2.2 *Doppler spread and coherence time*

The Doppler effect comes into play when a receiver experiences relative motion with respect to the transmitter, leading to a shift in the frequency of the received signal compared to the source frequency. This frequency shift, denoted as f_D, hinges on factors such as the relative motion between the transmitter and receiver, the wave's propagation speed, and the angle θ between the direction of motion of the mobile device and the propagation direction of the multipath signal. It can be expressed as:

$$f_D = \pm \frac{f_c v}{c} cos\theta. \tag{2.7}$$

where, f_c denotes the carrier frequency, θ represents the angle between the direction of motion of the mobile and the direction of incidence of propagation of the signal of the multipath, v is the relative velocity and c is the speed of light.

The Doppler power spectrum provides insight into the distribution of channel power across frequencies for the transmitted signal. The Doppler spread effect can be problematic, particularly for transmission techniques sensitive to carrier frequency offsets or higher relative speeds, as seen in the case of OFDM (TSE; VISWANATH, 2004).

On the other hand, coherence time represents the temporal period during which the channel maintains a high degree of correlation. The relationship between the Doppler effect and coherence time is given by (GHOSH *et al.*, 2010):

$$T_c \approx \frac{1}{f_D}. \tag{2.8}$$

In summary, both delay spread and coherence bandwidth are essential parameters in digital communications. For optimal system performance, it is desirable for τ_{max} to be significantly smaller than the symbol time to prevent ISI. Conversely, the parameter B_c should be significantly larger than the bandwidth of the transmitted signal to qualify as flat fading. Otherwise, frequency-selective fading occurs, leading to varying signal degradation across different frequencies within the transmitted band.

2.2.3 Channel model

This thesis centers on the OTFS modulation designed for high-mobility scenarios, which implies a time-varying channel, commonly referred to as an LTV channel. Our study adopts the same channel model as presented in (HADANI *et al.*, 2017), which describes the channel impulse response concerning Doppler spread and delay spread, as follows:

$$h(\tau, \nu) = \sum_{i=1}^{P} h_i \delta(\tau - \tau_i) \delta(\nu - \nu_i) \tag{2.9}$$

where P denotes the number of propagation paths, h_i, τ_i and ν_i represent the path gain, delay, and Doppler shift (or frequency) associated with i^{th} path, respectively, and $\delta(\cdot)$ denotes the Dirac delta function.

By performing an inverse Fourier transform within the Doppler domain ν, spanning from $[-\nu_{max}, \nu_{max}]$, on Eq. (2.9), we can derive $h(\tau, t)$, as follows:

$$\begin{aligned} h(\tau, t) &= \int_{\nu=-\infty}^{+\infty} h(\tau, \nu) e^{j2\pi\nu t} d\nu. \\ &= \int_{\nu=-\nu_{max}}^{\nu_{max}} h(\tau, \nu) e^{j2\pi\nu t} d\nu. \end{aligned} \tag{2.10}$$

This equation, denoted as the time-varying impulse response of the LTV channel (GHOSH *et al.*, 2010), demonstrates that the impulse response $h(\tau, t)$ changes over time t. This model is also known as the Tap Delays Line (TDL), which provides information about the gain and delay associated with each path P (JAIN, 2007).

However, real-world environments are far too intricate to create precise channel models, especially in high-mobility scenarios. In practice, most simulation studies employ empirical models developed based on measurements conducted in various real-world scenarios, commonly known as empirical models (ERCEG, 2001). These models are standardized by groups and institutions interested in obtaining results that closely resemble real-world scenarios for digital signal processing in the telecommunications field.

For practical comparisons with 5G technology in urban environments, we have chosen the channel model standardized by 3GPP, known as urban macrocell

(UMa), as presented in (AL-JZARI; IVIVA, 2015). The power delay profile parameters aligned with the channel TDL are outlined in Table 1:

Table 1 – Power Delay Profile for 3GPP channel - UMa

Tap No.	**Delay** (μs)	**Power** (dB)
1	0	0
2	0.36	-2.22
3	0.25	-1.72
4	1.04	-5.72
5	2.7	-9.05
6	4.59	-12.50

Source: AL-JZARI and IVIVA (2015).

In this macrocell model, as per Table 1, six taps or paths are considered, with each having an associated power in dB for delays in the order of microseconds (μs).

2.3 OFDM modulation

In the realm of telecommunications, wireless communication applications in multipath scenarios are commonplace, especially in the presence of high mobility. As discussed in Section 2.2, terrestrial propagation environments can be challenging due to factors like reflected waves, leading to selective fading of the transmitted signal, among other effects. Many solutions have been explored, particularly equalization techniques at the receiver. However, practical challenges arise, including the design of compact, cost-effective hardware, especially when dealing with high bit rates.

Modern applications demand ever-increasing data rates and grapple with issues related to selective fading. Traditional serial transmission systems that rely on a single carrier require equalization techniques to combat ISI, a common degradation type in multipath propagation channels. As the bit rate increases, the complexity of the equalizer also increases (CRUZ-ROLDáN *et al.*, 2020). To address these challenges, multicarrier modulation, sometimes called parallel or multiplexed transmission, emerges as an alternative. A significant advantage of multicarrier transmission over single-carrier systems, and perhaps the most prominent one, is its ability to reduce the impact of channel delay scattering and ISI (BAHAI; SALTZBERG, 1999). The concept involves dividing the high-rate input signal into lower-rate signals, each transmitted by multiple subcarriers. These new signals experience approximately flat fading in frequency.

In this context, where the goal is to transmit a large number of bits per second (bps) while maintaining service quality, various modulation techniques have been explored. One extensively studied candidate that eliminates the need for complex equalizers is Orthogonal Frequency Division Multiplexing (OFDM) (GOPIKRISHNAN *et al.*, 2009; ANJU; AHLAWAT, 2016; HARDAS; POKLEB, 2017).

OFDM was first introduced by Chang and Gibby in 1968 (CHANG; GIBBY, 1968) in 1968 and patented in 1970 (R. W. CHANG, 1970). It evolved from the Frequency Division Multiplexing (FDM) technique, which used guard bands to separate signal frequencies, resulting in spectrum wastage. OFDM remains a subject of extensive research in various wireless communication applications, including Wireless Local Area Network (WLAN), Digital Audio Broadcasting (DAB), Digital Video Broadcasting (DVB), vehicular communications, and cellular systems. It addresses several key challenges, including combating ISI and Inter-carrier Interference (ICI) through the insertion of the CP in multipath channels, as well as its straightforward and efficient implementation via the Inverse Fast Fourier Transform (IFFT).

OFDM is a data transmission technique that divides a given bandwidth into M orthogonal subcarriers while maintaining orthogonality among them. Each subcarrier carries QAM or Phase Shift Keying (PSK) symbols. Consequently, the transmission rate per subcarrier is lower than that of the serial data input. In essence, OFDM converts a high-rate serial data stream into multiple low-rate parallel sub-streams. The summation of these bandlimited OFDM subcarriers efficiently utilizes the available bandwidth, maximizing the number of transmitted symbols (DINIZ *et al.*, 2012). Additionally, the reduction in transmission rate, i.e., an increase in the duration of symbols transmitted on each subcarrier, leads to reduced sensitivity to frequency selectivity (time dispersion) caused by multipath effects (GUPTA; MEHRA, 2008).

It is worth noting that while the term "multiplexing" is part of OFDM's name, the actual multiplexing does not occur in an OFDM system. Instead, it entails the parallel transmission of an originally singular sequence of bits.

2.3.1 Orthogonality

Given ideal synchronization, the fundamental principle underlying OFDM modulation is the isolation of information transmitted by each subcarrier through appropriate correlators. The output of these correlators corresponds to the projection of the received OFDM signal onto its respective carrier (ROHLING, 2011). In essence, the concept revolves around achieving orthogonality among subcarriers. This is accomplished by selecting a uniform subcarrier spacing, typically represented as Δf, which is generally set to the inverse of the symbol duration T, i.e., $\Delta f = 1/T$.

Orthogonality enables spectral overlap, ensuring efficient utilization of the allocated bandwidth. One approach to achieve this objective is by using rectangular pulses for transmitting each subcarrier. According to the properties of the Fourier transform, the spectrum of each subchannel takes the shape of a $sinc$ function centered on the subcarrier frequency. Crucially, the zero crossings of the $sinc$ function occur precisely at intervals of $1/T$. Since all subcarriers are multiples of this spacing, no spectrum overlap occurs at the central frequencies containing the information. This design allows for complete information recovery through modulation and equalization in the frequency domain.

Figure 2 illustrates an example of the frequency spectrum of a baseband OFDM signal, highlighting the superposition of three orthogonal subcarriers that collectively form the overall spectrum. These subcarriers assume the shape of $sinc$ functions, with zero crossings at multiples of $1/T$. Notably, each normalized frequency value on the horizontal axis of this figure corresponds to the frequency of a subcarrier.

Figure 2 – Orthogonality in the frequency domain

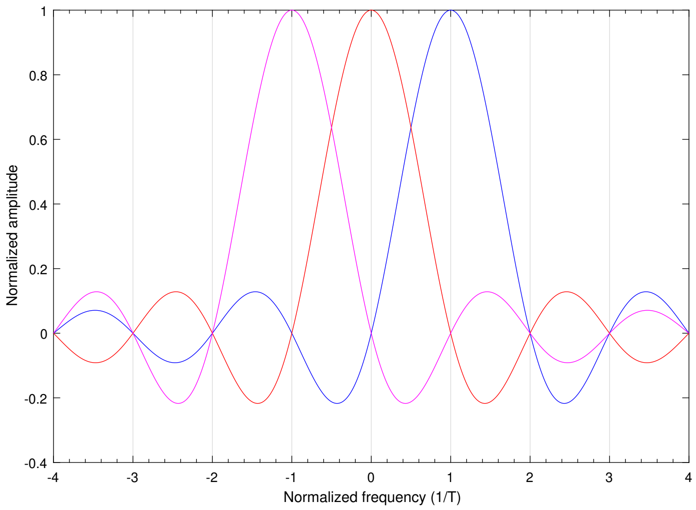

Source: the author.

In the time domain, orthogonality is a fundamental principle that ensures that each subcarrier precisely completes an integer number of cycles within the interval of an OFDM symbol duration. This phenomenon arises because the subcarriers are separated in frequency by a multiple of $1/T$. Consequently, in the time domain, it becomes evident that any two subcarriers within the baseband OFDM transmission signal exhibit a difference equal to an integer number of cycles, as visually depicted in Figure 3.

Figure 3 – Orthogonality in the time domain

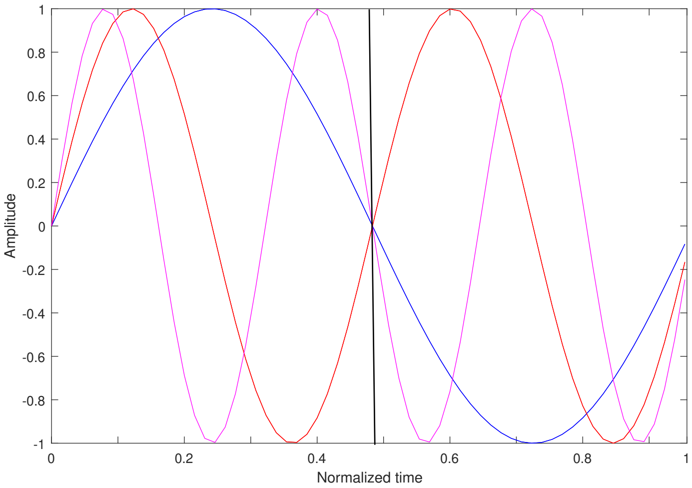

Source: the author.

Next, we discuss OFDM modulation and the particularities of a classical system model.

2.3.2 Discrete-time OFDM system model

In essence, the direct generation and subsequent demodulation of an OFDM signal traditionally requires the deployment of coherent oscillators, leading to a complex and costly implementation, especially when a substantial number of subcarriers are involved (ROHLING, 2011). Nevertheless, the complexity of these modulation and demodulation processes can be significantly mitigated through the employment of IFFT and Fast Fourier Transform (FFT) algorithms, respectively. In this context, Figure 4 provides an illustrative depiction of the fundamental block diagram of a conventional OFDM system.

Figure 4 – OFDM system model

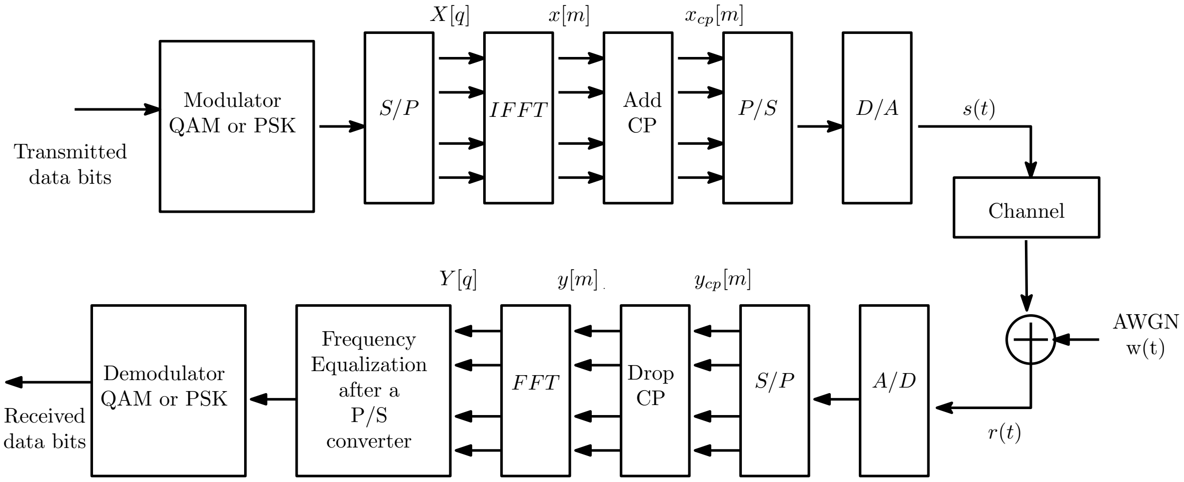

Source: adapted by author from (ROHLING, 2011).

As previously mentioned, the core concept of OFDM involves partitioning the transmission bandwidth into M sub-bands, each capable of carrying a complex symbol. As illustrated in Figure 4, the initial step involves modulating the input data stream using either QAM or PSK modulation techniques. These modulation symbols are systematically mapped onto a constellation diagram using Gray coding, wherein only a single bit differs between adjacent symbols (HAYKIN; MOHER, 2005). Subsequently, this collection of complex symbols undergoes processing through a serial-to-parallel converter, yielding a set of M parallel QAM or PSK symbols denoted as $X[q]$, $q = 0, 1, ..., M-1$, each corresponding to the symbols transmitted over individual subcarriers. At this stage, it is important to note that the symbols are assumed to be shaped by a rectangular window, and cyclic prefix (CP) is not yet considered (as will be discussed in the following section), To generate the time-domain signal $s(t)$, the frequency components are transformed into time samples by employing an IDFT (IFFT algorithm) on these N symbols. Consequently, the transmitted signal $s(t)$ in base-band ($s[m']$), is given by:

$$\begin{aligned} s[m'] &= \frac{1}{\sqrt{M}} \sum_{q=0}^{M-1} \sum_{n'} X_{qn'} g_{tx}[m' - n'M] e^{j2\pi \frac{qm'}{M}} \\ &= \frac{1}{\sqrt{M}} \sum_{q=0}^{M-1} X[q] e^{j2\pi \frac{qm'}{M}} \end{aligned} \tag{2.11}$$

where $X[q] = \sum_{n'} X_{qn'} g_{tx}[m' - n'M]$ is a complex symbol stream, X_{qn} represents the set of symbols transmitted on subcarrier q at a discrete time instant $n \in \mathbb{Z}$, and $g_{tx}[m']$ is the transmitter filter, which assumes a value of 1 if $0 \leq m' \leq M-1$ and 0 otherwise.

Subsequent to the modulation process, the signal undergoes conversion into a parallel format, resulting in M separate data streams denoted as $X[q]$. Each of these individual signals modulates a subcarrier, giving rise to a vector of M sub-symbols that collectively constitute the OFDM symbol. These $X[q]$ subcarriers are then combined through a computational implementation of the Inverse Discrete Fourier Transform (IDFT), commonly referred to as IFFT. This process yields samples in the time domain, represented as $x[m]$, which subsequently pass through a serial-to-parallel converter. Following this conversion, an analog-to-digital conversion takes place, preparing the signal for transmission over a channel. Our study focuses on the transmission over time-varying channels.

As a result, when the receiver is in synchronization with the transmitter, the received signal can be sampled at a rate of $1/T$. The DFT algorithm is applied to each block of M received samples. Under ideal propagation channel conditions, this operation yields the estimated values $\hat{X}[q]$ or $Y[q]$ from the received signal $y[m]$, as expressed by:

$$\begin{aligned} Y[q] &\equiv DFT(y[m]) \\ &\equiv \frac{1}{M}\sum_{m=0}^{M-1} y[m]e^{-j2\pi\frac{qm}{M}} \end{aligned} \tag{2.12}$$

Subsequently, during the reception phase, the inverse operations of those performed at the transmitter are carried out to facilitate the recovery of binary data at the output of the QAM demodulator. Nevertheless, in multipath fading channels, especially in scenarios characterized by high mobility, the time variation of a fading channel across an OFDM symbol's duration directly influences the orthogonality between subchannels, thus giving rise to the issue of ICI (LI; KAVEHRAD, 1999). The incorporation of a CP to each OFDM symbol effectively mitigates the challenges posed by both ISI and ICI, a topic that will be explored in the subsequent subsection.

2.3.3 Cyclic prefix

In classical OFDM, maintaining the orthogonality between subcarriers is a fundamental requirement for generating OFDM symbols accurately. Achieving this demands not only appropriate spacing between the carriers but also the synchronization of the receiver and transmitter, along with the incorporation of guard intervals.

The guard interval can be established by cyclically extending the symbol or by filling it with zeros. In the former scenario, the guard interval is affixed at the outset of each OFDM symbol, giving rise to Cyclic Prefix - OFDM (CP-OFDM) transmission. In the latter approach, zeros are inserted at the end of each OFDM symbol, resulting in Zero Padding - OFDM (ZP-OFDM) transmission.

For the purposes of this work, we refer to the guard interval utilized in classical OFDM as CP-OFDM (HE; SCHMEINK, 2015). From here, we will just call CP-OFDM of OFDM. Therefore, we primarily focus on this variant for the purpose of comparison with the subject of this study, OTFS modulation.

One of the notable advantages of employing OFDM transmission is its robustness against channel delay scattering, denoted as τ_{rms}, (ZHANG; LIU, 2006). The increasing symbol duration enhances the system's ability to withstand with the effects of this dispersion, as it reduces the τ_{rms}-to-T, rendering the system less susceptible to ISI.

To mitigate interference effects on the received signal, a guard interval duration, denoted as T_L, is introduced within each OFDM symbol. This duration must be carefully chosen to ensure that the convolution response between the transmitted signal and the propagation channel does not interfere with the reception of the subsequent symbol (AL-JZARI; IVIVA, 2015). To achieve this goal, the CP length must exceed the delay spread of the multipath channel (SHAH *et al.*, 2010). An OFDM symbol (of duration T_{ofdm}) thus consists of the useful OFDM symbol with duration $T_u = 1/\Delta f$ and the guard interval of duration T_L, i.e., $T_{ofdm} = T = T_u + T_L$.

However, it is essential to note that the inclusion of the CP comes at a cost. It reduces bandwidth efficiency and diminishes the data rate (system capacity) because it carries no information, thereby dispersing the transmitter's energy, and thus impacting the SNR. To optimize the choice of CP length, it is typically selected based on the duration of the multipath channel in a specific operational environment (NESS *et al.*, 2002).

As shown in Figure 4, during OFDM transmission, the CP is inserted immediately following the IFFT-derived signal, denoted as $x_{cp}[m]$. This sequence comprises the last L samples of the $x[m]$ sequence, where L is the length of the CP, and then, each useful symbol was allocated in a subcarrier. According to (GOLDSMITH, 2005), we can express $x_{cp}[m]$ for the range $-L \leq m \leq M-1$, as follows:

$$
\begin{aligned}
x_{cp}[-L], ..., x_{cp}[M-1] = x[M-L], ..., x[M-1], x[0], ..., x[M-1] \\
x_{cp}[m] = x[m]_M \implies x_{cp}[m-n] = x[m-n]_M.
\end{aligned} \tag{2.13}
$$

where $-L \leq [m-n] \leq M-1$, and $[.]_M$ is the module operator of size M.

T_u represents the duration of an OFDM symbol, and each OFDM symbol comprises a collection of M subsymbols generated through QAM or PSK modulation. Therefore, cyclic extension entails inserting a duplicate of the block formed by the last $L = T_L/T_{sb}$ samples of this OFDM symbol at the beginning of each OFDM symbol. At the receiver, the information contained within the guard interval is discarded (WEN *et al.*, 2021), and only the M samples, confined within the T_u interval, are employed in the DFT operation.

With CP insertion, Eq. (2.11) for the baseband transmitted signal can be reformulated simply by adding the last L samples of symbols allocated at the start of the OFDM useful frame ($q = 0, 1, ..., M-1$). This results in a transmitted signal $s_{cp}[m]$ comprising $M+L$ samples, as expressed below:

$$
s_{cp}[m] = \frac{1}{\sqrt{M}} \sum_{q=0}^{M-1} \sum_{n'} X_{qn'} g[m - n'(M+L)] e^{j2\pi \frac{qm}{M}} \tag{2.14}
$$

As illustrated in Figure 4, during reception and following the A/D and S/P conversion processes of the signal $r(t)$, we obtain $y_{cp}[m]$, where $m = 0, 1, ..., M+L-1$. The CP length L is subsequently removed to yield $y[m]$. An M-point FFT is then applied to $y[m]$, followed by an equalization process, resulting in a block of M complex QAM symbols $Y[q]$, as detailed in Eq. (2.12).

In this context, recognizing that the multipath channel functions as a transmitted linear filter on the OFDM symbols $s_{cp}[m]$, mathematically in discrete domain, these symbols undergo linear convolution with the CIR $h[m]$ and are affected by AWGN ($w[m]$) (MALIK; TRIPATHI, 2017). Denoting linear convolution as "$*$", the received signal in discrete time can be represented, disregarding the noise, as: $y[m] = h[m] * s[m]$. Within this context, the primary objective behind introducing CP is to transform this linear convolution into a circular convolution (denoted by $\circledast$). This transformation can be observed in Eq. (2.13), where $x_{cp}[m] \equiv s_{cp}[m]$ and ignoring the noise, resulting in:

$$\begin{aligned} y[m] &= x_{cp}[m] * h[m] \\ &= \sum_{n=0}^{L} h[n] x_{cp}[m-n] \\ &= \sum_{n=0}^{L} h[n] x[m-n]_M \\ &= x[m] \circledast h[m] \end{aligned} \tag{2.15}$$

Subsequently, following the removal of the CP at the reception and the application of a DFT, we have:

$$\begin{aligned} Y[q] &= DFT(x[m] \circledast h[m]) \\ &= X[q]H[q] \end{aligned} \tag{2.16}$$

Consequently, the adverse effects of the channel can be effectively mitigated at the receiver using a straightforward frequency domain equalizer. This equalizer essentially inverts the estimated Channel Impulse Response (CIR) and multiplies it by the frequency response of the received signal, yielding a robust estimation of the OFDM symbols $Y[q]$, consistent with the equalizer described in Eq. (2.17).

As previously mentioned, as long as the delay spread of the channel remains smaller than the guard interval, it can be ensured that delayed replicas of the OFDM symbol will consistently exhibit an integer number of cycles within the FFT calculation interval, thereby preserving orthogonality conditions. It is worth noting that high constellation modulations (e.g., QAM-64, QAM-128, and beyond) are more susceptible to ICI and ISI, compared to lower-order modulations (PRASAD; NEE, 2000). In such scenarios, the adoption of more intricate error correction codes becomes essential to effectively manage the interference effects.

2.4 Equalization

The fundamental objective within a telecommunication system revolves around the detection of each transmitted symbol from the received signal, a process known as equalization (TSE; VISWANATH, 2004).

Moreover, considering that channel characteristics are typically either unknown or subject to change over time, the primary aim of an equalizer is to mitigate ISI to facilitate the recovery of transmitted symbols (PROAKIS; SALEHI, 2008). In this context, the equalization techniques implemented at the receiver are designed to counteract the impairments introduced by the multipath propagation inherent in wireless channels. In addition, equalizers restore the frequency spectrum of the transmitted signal.

This aspect underscores one of the significant advantages of OFDM systems, as elaborated upon in Section 2.3. OFDM's distinctive feature is its capacity to conduct equalization in the frequency domain. Through equalization, it becomes possible to estimate the transmitted symbols after applying the FFT, provided that the complex gain of the channel for each subcarrier is known. The symbols estimated by the equalizer in the frequency domain are mathematically represented as follows (GOLDSMITH, 2005):

$$\hat{X}[q] = \frac{Y[q]}{\hat{H}[q]}. \tag{2.17}$$

where q designates the q-th subcarrier, $Y[q]$ represents the received signal, and $\hat{H}[q]$ is the complex response of the estimated channel. The equalizer outlined in Eq. (2.17) is a linear filter, commonly referred to as ZF per subcarrier. This filter essentially provides an approximate inverse of the channel's response. Notably, despite the channel inversion, there is no amplification of noise, as both the channel and the noise experience power scaling by the inverse of the estimated channel (GHOSH *et al.*, 2010).

When the channel response exhibits variations across time and frequency, it becomes feasible to apply ZF over a set of OFDM frames. In this scenario, it is essential to construct a vector $\boldsymbol{y}$ representing the received signal with dimensions $MN \times 1$ and a matrix $\boldsymbol{H}$ characterizing the channel with dimensions $MN \times MN$. This can be expressed as follows:

$$\begin{aligned} \hat{\boldsymbol{x}}_{ZF} &= \left(\boldsymbol{H}^H \boldsymbol{H}\right)^{-1} \boldsymbol{H}^H \boldsymbol{y} \\ &= \boldsymbol{H}^{-1} \boldsymbol{y} \end{aligned} \tag{2.18}$$

When considering the transmission of M subcarriers and N OFDM symbols, where: σ_0^2 signifies noise variance, σ_d^2 represents signal variance, $\boldsymbol{H}$ represents the channel matrix, and $\boldsymbol{y}$ corresponds to the received signal vector excluding the CP.

One limitation of the ZF equalizer is the phenomenon known as noise enhancement, particularly when the received signal is weak at certain frequencies (PROAKIS; SALEHI, 2008). This limitation can be mitigated by replacing the ZF equalizer with a linear MMSE equalizer (HAYKIN; MOHER, 2005). The MMSE equalizer optimizes its coefficients to minimize both ISI and the effects of AWGN by employing the minimum mean squared error (MMSE) criterion. The MMSE equalizer is derived as follows:

$$\hat{\boldsymbol{x}}_{MMSE} = \left(\frac{\sigma_0^2}{\sigma_d^2}\boldsymbol{I}_M + \boldsymbol{H}^H\boldsymbol{H}\right)^{-1}\boldsymbol{H}^H\boldsymbol{y} \tag{2.19}$$

The results detailed in 2.5 present the BER performance of OFDM in a high mobility scenario, considering the macrocell channel.

2.5 Simulations: OFDM under high mobility

While OFDM modulation offers numerous advantages, it is not without its challenges, particularly concerning the occurrence of high-amplitude peaks that result in a high PAPR. These peaks can potentially lead to amplifier saturation, consequently causing ICI (ANN *et al.*, 2016). Furthermore, as the signal propagates through a channel, issues related to system synchronism loss arise, introducing complexity into the transmission of symbols. This complexity can manifest as phase rotations, interference, and additional degradation imposed by the channel on the subcarriers. These complications are further exacerbated when the signal is transmitted through a time-varying channel, especially one characterized by high mobility.

Numerous studies have explored proposals in both time and frequency domains aimed at mitigating the effects of a doubly selective channel on the performance of OFDM systems, particularly when multipaths exhibit high-speed motion (YALCIN *et al.*, 2008; GOPALA; SLOCK, 2014; SOULEYMANE *et al.*, 2016; PATRA; SINGH, 2017). To facilitate a comparison with OTFS modulation, we have chosen to consider the Urban Macrocell (UMa), commonly referred to as a macrocell channel, which represents a high-mobility scenario and is based on a practical channel model standardized by 3GPP. This model is characterized by its PDP, as outlined in Table 1. The parameters utilized in simulations of the OFDM system within a macrocell channel are detailed in Table 2:

Table 2 – Simulation Parameters for OFDM

Parameter	**Value**
Carrier frequency (f_c)	4 GHz
Subcarrier spacing (Δf)	15 kHz
Number of subcarriers (M)	16 and 600
Number of OFDM symbols (N)	8 and 12
CP length (L)	4 and 255
Channel model	Urban macrocell
Modulation scheme	4-QAM and 16-QAM
UE speed	330 and 500 km/h
Channel estimation	ideal

Source: the author.

Figures 5, 6, 7 and 8 provide insights into the BER performance within the SNR range [5dB, 25dB] for the classical OFDM system. Additionally, the figures showcase the OFDM scheme employing a similar vector analysis methodology presented for OTFS modulation in Appendix A. These figures also incorporate the performance of OFDM on an AWGN channel. In this modified OFDM system, we obtain the channel input-output relation for application in ZF and MMSE linear filters for data detection. The detailed calculations for this 2D analysis for OFDM are provided in Appendix A.

The results for OFDM were conducted using two modulation schemes, 4-QAM and 16-QAM, assuming knowledge of the channel. These evaluations were performed for two configurations: one with 16 active subcarriers and the other with 600 active subcarriers. As anticipated, the results align with the expected trends (PRASAD; NEE, 2000). Specifically, with an increase in the constellation order, the 4-QAM modulation scheme outperforms the 16-QAM scheme under the same parameter settings.

The BER values were determined from the outcomes of two detectors: ZF ((2.18)), illustrated as the continuous blue curve, and MMSE ((2.19)), depicted as the dashed red curve. These detectors were employed in a 2D processing framework, as detailed in Appendix A, where the channel matrix $\boldsymbol{H} => \boldsymbol{H}_{eff}^{ofdm}$ has dimensions $MN \times MN$. For comparative purposes, the theoretical BER was also calculated for the case of an AWGN channel, represented by the magenta curve. In this scenario, white noise is simply added to the transmitted signal, and demodulation using QAM is applied after discarding the CP during reception.

In the simulation, employing 4-QAM modulation (Fig. 5) and 16-QAM modulation (Fig. 6), assuming a subcarrier spacing of $\Delta f = 15KHz$, we transmit $N = 8$ OFDM symbols each with $M = 16$ active subcarriers and a CP of length equal to 4. It is evident that the BER exceeds 10^{-4} for classic OFDM and 10^{-5} with MMSE and ZF estimators at an SNR of 15dB. Beyond an SNR of 15dB, the results exhibit negligible errors within the considered range. In the case of the 16-QAM scenario, MMSE and ZF estimators reach an approximate BER of 10^{-4} at 20dB, while conventional OFDM exhibits a BER of 10^{-2}, which does not reduce 10^{-3} even when SNR increases to 25dB. This worsening of results is well-documented in the literature and stems from the increased difficulty of decision-making as the QAM constellation size grows, consequently leading to more errors.

Figure 5 – BER Performance in OFDM system on macrocell channel (4-QAM; $M = 16; N = 8; CP = 4$)

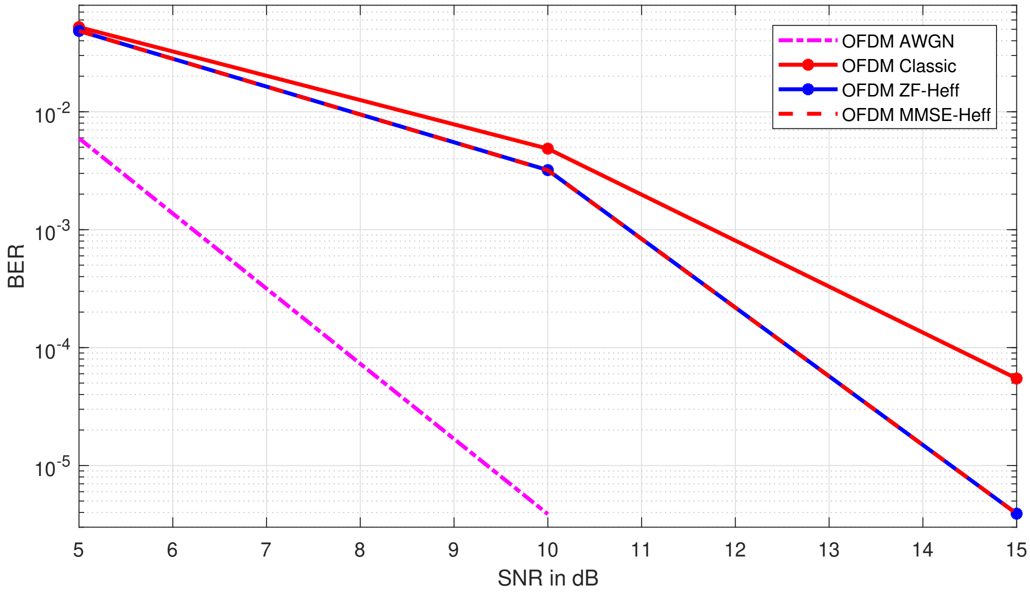

Source: the author.

It's essential to emphasize that when considering 16 subcarriers, the results for OFDM yield a sampling rate of $4.17\mu s = 1/(16.\Delta f)$. At this rate, the generated multipath channel synthesizes only two taps. However, when the number of subcarriers is increased to 600, resulting in a sampling rate of $0.11\mu s = 1/(600.\Delta f)$, the channel is modeled with 6 taps, following the UMa in TDL model. Consequently, as depicted in Figures 7 and 8, the performance significantly deteriorates compared to the 2-tap scenario.

Figure 6 – BER Performance in OFDM system on macrocell channel (16-QAM; $M = 16; N = 8; CP = 4$)

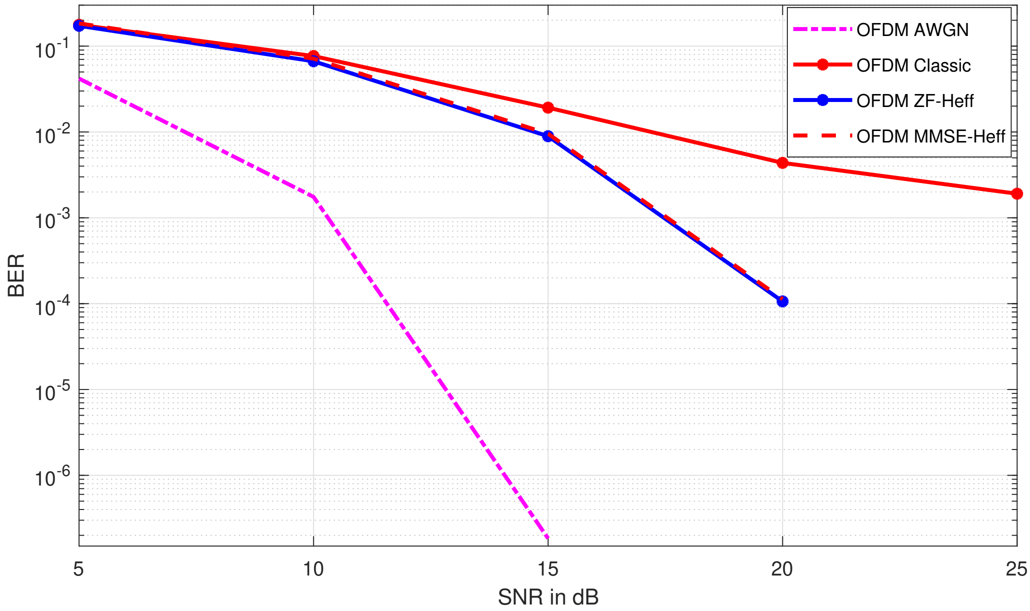

Source: the author.

In this particular scenario involving 1000 frames, we transmit $N = 12$ OFDM symbols per frame, each containing $M = 600$ active subcarriers along with a Cyclic Prefix (CP) of length equal to 255. The results indicate that, across all three detection techniques, the BER does not drop below the order of 10^{-3}, even at an SNR of 25dB. Particularly noteworthy is the degradation in performance with the increase in constellation size, especially evident in the case of 16-QAM under high-mobility channels. With an SNR of 25dB, the BER surpasses 10^{-2}, a notably low rate for a system aiming to deliver high data rates.

Figure 7 – BER Performance in OFDM system on macrocell channel (4-QAM; $M = 600; N = 12; CP = 255$)

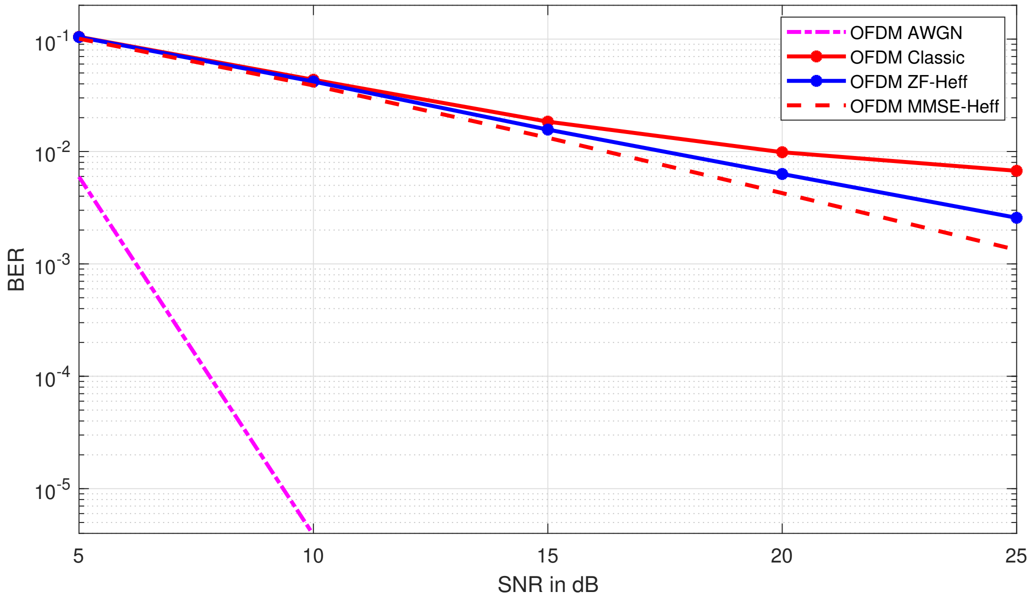

Source: the author.

Figure 8 – BER Performance in OFDM system on macrocell channel (16-QAM; $M = 600; N = 12; CP = 255$)

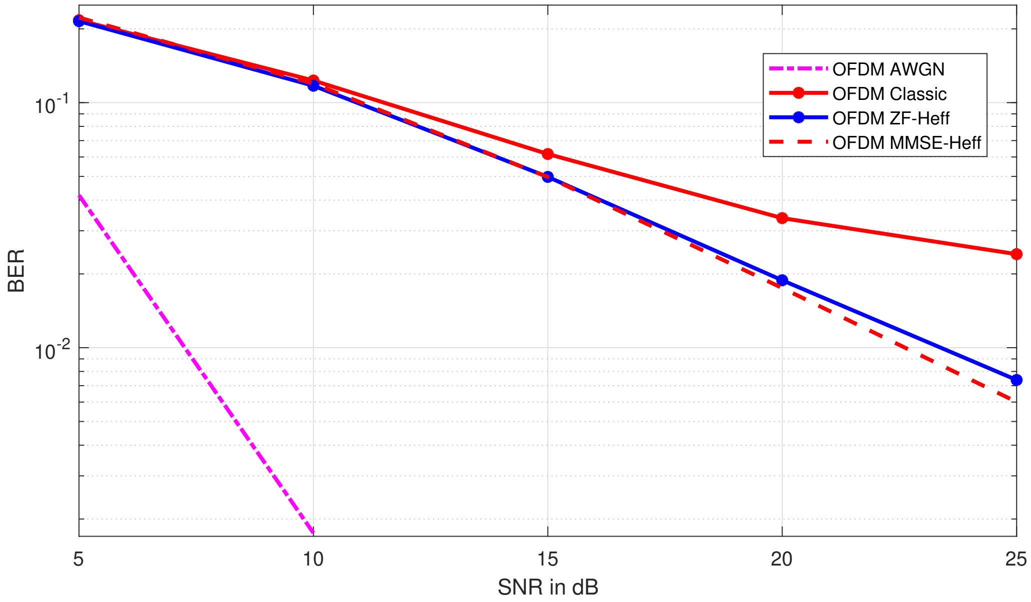

Source: the author.

The augmentation in complexity, stemming from an increased number of subcarriers, the incorporation of the CP into a multipath channel, and the expansion of the number of symbols, reveals that OFDM systems struggle to perform optimally in high-mobility scenarios. This challenge arises because the channel cannot fluctuate significantly during the transmission of a single symbol. While various techniques and adaptations have been proposed to enhance modulation and performance (GUPTA; MEHRA, 2008), the results underscore the limitations of the OFDM system in high-mobility environments.

In light of these constraints, the OTFS modulation emerges as a promising alternative to address the challenges posed by rapidly varying channels. The subsequent section will delve into the details of this modulation technique.

3 OTFS MODULATION FUNDAMENTALS

Traditional OFDM modulation primarily operates in the frequency-time domain, where each OFDM Resource Elements (RE) corresponds to one subcarrier within a particular OFDM symbol. In contrast, OTFS modulation operates within the Delay-Doppler domain, a concept interrelated with frequency and time via the Symplectic Finite Fourier Transform (SFFT), a two-dimensional Discrete Fourier Transform (DFT) (HADANI *et al.*, 2017; HADANI; MONK, 2018). The OTFS modulation framework can be conceptualized as a time-frequency multicarrier modulation, augmented by a preprocessing transformation that shifts from the delay-Doppler domain to the time-frequency domain of information symbols through the Inverse Symplectic Finite Fourier transform (ISFFT). Consequently, OTFS can be integrated as a preprocessing step on top of an underlying OFDM signal (86BIS, 2002).

3.1 Delay-Doppler Domain

Within the OTFS framework, the quadrature amplitude modulation (QAM) symbols are associated with grid points within the Delay-Doppler domain. The Inverse Symplectic Finite Fourier Transform (ISFFT) facilitates the weighting of each QAM symbol to a two-dimensional (2D) basis function defined in the Time-Frequency domain. The dimensions of the delay-Doppler resource grid are directly linked to the characteristics of the frequency-time plane, including properties such as bandwidth (B), Transmission Time Interval (TTI), pulse time duration (T), subcarrier spacing (Δf), number of subcarriers (M), and symbol block length (N).

Consequently, the delay-Doppler grid comprises M points (representing the number of subcarriers) along the delay axis, with a spacing of $\Delta\tau = \frac{1}{M\Delta f}$, and N points (representing the number of symbols) along the Doppler axis, with a spacing of $\Delta\nu = \frac{1}{NT}$. The reciprocal time-frequency grid consists of M points along the frequency axis, with a spacing of $\Delta f = \frac{B}{M}$, and N points along the time axis, with a spacing of $T = \frac{TTI}{N}$ (RAVITEJA, 2018). This results in a time-frequency grid composed of N multicarrier symbols, each housing M subcarriers. The transmission bandwidth B inversely relates to the delay resolution $\Delta\tau$, while the TTI inversely relates to the Doppler resolution $\Delta\nu$. Both grids are visualized in Figure 9.

Figure 9 – OTFS Transform: Delay-Doppler grid vs Time-Frequency

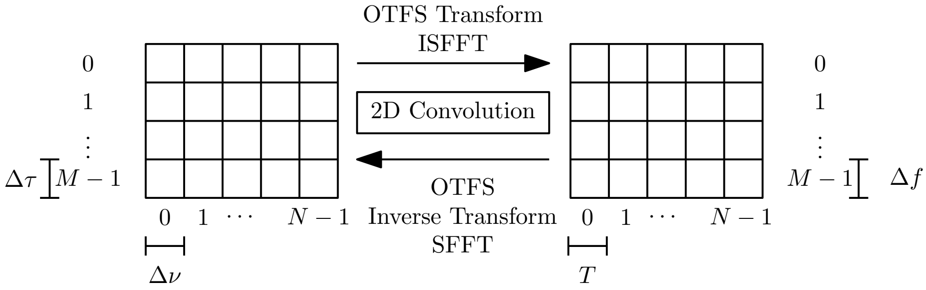

Source: adapted by author from (RAVITEJA, 2018).

In essence, based on these definitions, the time-frequency plane becomes discretized, achieved by sampling the time and frequency axes at intervals of T (in seconds) and Δf (in Hz):

$$\Lambda = \{(m\Delta f, nT),\ m = 0, ..., M-1;\ n = 0, ..., N-1\}, \tag{3.1}$$

Consequently, the delay-Doppler plane undergoes discretization as follows:

$$\Gamma = \left\{\left(\frac{l}{M\Delta f}, \frac{k}{NT}\right), l = 0, ..., M-1; k = 0, ..., N-1\right\}. \tag{3.2}$$

3.2 ISFFT

This scheme primarily revolves around the 2D ISFFT, which maps the information symbols $X[l,k]$ to a grid Γ (3.2) in the delay-Doppler domain, resulting in a sequence of complex numbers $X^{FT}[m,n]$ within a grid Λ (3.1) in the time-frequency domain. This transformation takes the form:

$$X^{FT}[m,n] = \frac{1}{\sqrt{MN}} \sum_{l=0}^{M-1} \sum_{k=0}^{N-1} X[l,k]\ e^{j2\pi\left(\frac{nk}{N} - \frac{ml}{M}\right)}. \tag{3.3}$$

Following this pre- and post-processing procedure, one can implement conventional OFDM modulation and demodulation. Figure 10 illustrates the SISO-OTFS system diagram, comprising a single transmitter antenna and one receiver antenna.

The OFDM modulator is employed to process time-frequency symbols $X^{FT}[m,n]$, converting them into a time-domain signal $s(t)$ suitable for transmission over

Figure 10 – SISO-OTFS system diagram

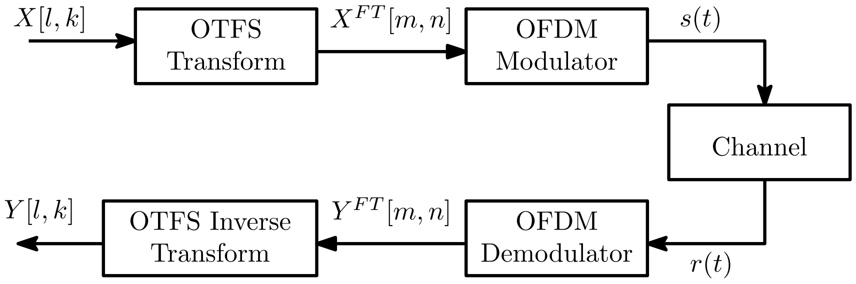

Source: adapted by author from (RAVITEJA, 2018).

the channel. Therefore, the output signal of the OTFS transmitter is represented as:

$$s(t) = \sum_{m=0}^{M-1}\sum_{n=0}^{N-1} X^{FT}[m,n]\; e^{j2\pi m\Delta f(t-nT)}\; g_{tx}(t-nT), \tag{3.4}$$

where $g_{tx}(t)$ denotes the pulse shaping used in the transmitter. In the following we will consider rectangular pulses of amplitude equal to 1 and duration T.

In equation (3.4) it is evident that each OTFS QAM symbol extends across the entire time-frequency grid, allowing for the exploitation of all available channel diversity.

The transmitted signal $s(t)$ propagates through a time-varying channel characterized by a complex baseband channel impulse response $h(\tau,\nu)$ and noise $w(t)$. After going through the channel, the received signal $r(t)$ is defined as:

$$r(t) = \int_{\tau}\int_{\nu} h(\tau,\nu)s(t-\tau)\; e^{j2\pi\nu(t-\tau)}d\tau d\nu + w(t). \tag{3.5}$$

Channel modeling can be characterized by deriving the Delay-Doppler Profile (DDP) of the channel (RAMACHANDRAN; CHOCKALINGAM, 2018), which encapsulates the delay and Doppler paths associated with each multipath reflector. Given the sparsity of the channel representation, it is practical to express the response $h(\tau,\nu)$ as per Eq. (2.9). Consequently, the delay and Doppler taps for the i^{th} path are described by:

$$\tau_i = \frac{l_i + \tilde{l}_i}{M\Delta f},\; \nu_i = \frac{k_i + \tilde{k}_i}{NT}, \tag{3.6}$$

where l_i denotes the integer delay, $\tilde{l}_i$ denotes the fractional delay, k_i represents the integer Doppler, and $\tilde{k}_i$ signifies the fractional Doppler shift. NT and $M\Delta f$ correspond to the total duration and bandwidth of the transmitted signal frame, respectively. Fractional delay and fractional Doppler shift-induced interference can be effectively suppressed when M and N are suitably large to approximate ideal OTFS resolution. Under these circumstances, it is reasonable to consider $\tilde{l}_i = \tilde{k}_i = 0$ (DING *et al.*, 2019).

The received signal $r(t)$ is sampled at a rate $f_s = M\Delta f$, resulting in the formation of a signal $r[n]$. From Eq. (3.5) and Eq. (2.9), it is clear that the entries are expressed as:

$$r[n] = \sum_{i=1}^{P} h_i \, e^{j2\pi \frac{(k_i+\tilde{k}_i)(n-l_i)}{MN}} (s[n-l_i]_{MN}) + w[n]. \tag{3.7}$$

where $[.]_B$ means the module B operation.

Subsequently, at the receiver, the time-domain received signal can be mapped into the time-frequency domain by an OFDM demodulator, and then into the delay-Doppler domain using the SFFT.

3.3 OTFS versions in SISO system

In the context of Single-Input and Single-Output (SISO) systems, OTFS has been explored with two distinct versions, as described in (ZHOU *et al.*, 2022), addressing the challenge of Inter-Symbol Interference (ISI). These versions are referred to as the "standalone" or "underlay" version and the "overlay" version.

In the standalone or underlay version, illustrated at the bottom of Figure 11, a simplified approach in respect to overlay version is taken. In standalone case, we consider that the OFDM system without CP based OTFS system with a single transmitting antenna and single receiving antenna, i.e., a Single-Input and Single-Output (SISO) model, as described in (HASHIMOTO *et al.*, 2021).

All N OFDM symbols, each containing M subsymbols, are concatenated to form the OTFS frame. Subsequently, a Cyclic Prefix (CP) is added at the beginning of each OTFS frame. This simplification is possible because half of the pre- and post-processing operations, such as ISFFT and SFFT, can be effectively cancelled out by FFT and IFFT operations (ZHOU *et al.*, 2022). The schematic representations of both versions are depicted in Figure 11.

The standalone version, discussed in (RAVITEJA *et al.*, 2018), significantly enhances the spectral efficiency of the overall system, especially when N is large or the

Figure 11 – Time-domain frame of OTFS: the top one is the overlay, and the bottom one is the standalone version

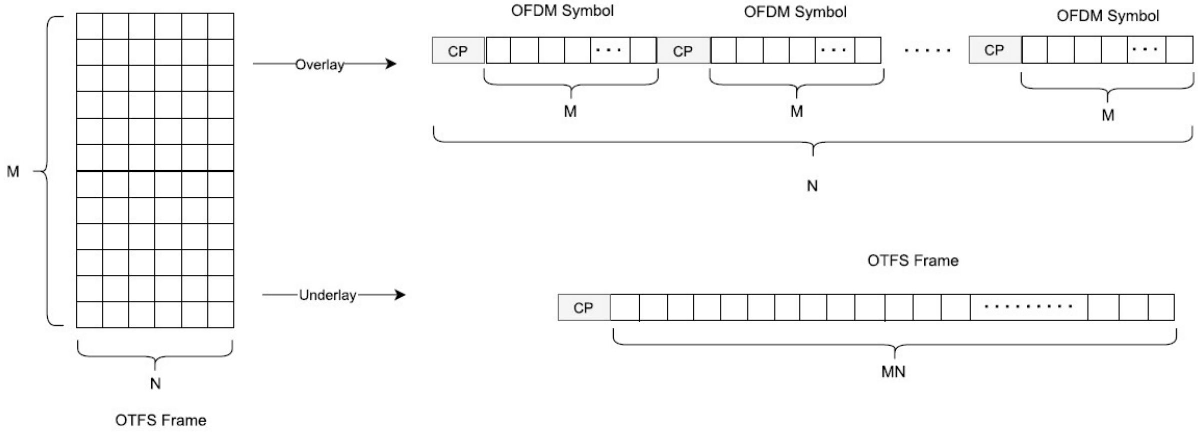

Source: adapted by author from (ZHOU *et al.*, 2022).

CP overhead is substantial, requiring at least 25% CP. In this design, a CP of length L is appended to $s(t)$ before transmission.

The overlay version, seen at the top of Figure 11, implements OTFS as an overlay on top of an OFDM system. While this approach provides more flexibility, it introduces added complexity to the system, as each OTFS symbol requires the addition of a CP. Both standalone and overlay versions will be analyzed in vector form in the following subsections: 3.3.1 and 3.3.2, respectively.

3.3.1 Vector analysis for standalone OTFS

Building on the mathematical foundation described in Section 3.2, the authors in (RAVITEJA *et al.*, 2018) leverage vector properties and identities to analyze the standalone OTFS system in the discrete domain. Using notation conventions, with lowercase letters representing vectors ($\boldsymbol{a}$), uppercase letters for matrices ($\boldsymbol{A}$), and $\boldsymbol{A}^H$ indicating the Hermitian transpose, and considering that $T = T_u \implies T\Delta f = 1 \implies T_u = 1/\Delta f$, the transmitted signal can be expressed as:

$$\begin{aligned}\boldsymbol{S} &= \boldsymbol{G}_{tx}\boldsymbol{F}_M^H(\boldsymbol{F}_M\boldsymbol{X}\boldsymbol{F}_N^H)\\ &= \boldsymbol{G}_{tx}\boldsymbol{X}\boldsymbol{F}_N^H,\end{aligned} \tag{3.8}$$

where $\boldsymbol{S} \in \mathbb{C}^{M\times N}$ represents the transmitted symbols in the time-frequency domain, and $\boldsymbol{X} \in \mathbb{C}^{M\times N}$ denotes the two-dimensional information symbols transmitted in the delay-Doppler domain. Additionally, $\boldsymbol{F}_n = \left\{\frac{1}{\sqrt{n}}e^{2\pi jkl/n}\right\}_{k,l=0}^{n-1}$ and $\boldsymbol{F}_n^H = \boldsymbol{F}_n^{-1}$ are the

n-point Discrete Fourier Transform (DFT) and the Inverse Discrete Fourier Transform (IDFT) matrices, respectively. $\boldsymbol{G}_{tx}$ is the diagonal matrix of size $M \times M$ that contains transmission pulse samples with a duration $[0, T]$, repeated N times in a frame. Consequently, the column-wise vectorization of the $\boldsymbol{S}$ matrix in Eq. (3.8) yields the $MN \times 1$ vector $\boldsymbol{s}$, the transmit vector:

$$\boldsymbol{s} = vec(\boldsymbol{S}) = (\boldsymbol{F}_N^H \otimes \boldsymbol{G}_{tx})\boldsymbol{x}, \tag{3.9}$$

where $\boldsymbol{x} = vec(\boldsymbol{X})$ and $\otimes$ denotes the Kronecker product.

As a result, the received signal vector **r**, of size $MN \times 1$, can be expressed using samples from Eq. (3.7):

$$\boldsymbol{r} = \boldsymbol{H}\boldsymbol{s} + \boldsymbol{w}, \tag{3.10}$$

where $\boldsymbol{w}$ represents the noise vector and $\boldsymbol{H}$ is an $MN \times MN$ matrix defined as:

$$\boldsymbol{H} = \sum_{i=1}^{P} h_i \boldsymbol{\Pi}^{l_i} \boldsymbol{\Delta}_{k_i, l_i}, \tag{3.11}$$

with $\boldsymbol{\Pi}^{MN \times MN}$ the permutation matrix (forward cyclic shift),

$$\boldsymbol{\Pi} = \begin{bmatrix} 0 & \dots & 0 & 1 \\ 1 & \ddots & 0 & 0 \\ \vdots & \ddots & \ddots & \vdots \\ 0 & \dots & 1 & 0 \end{bmatrix}, \tag{3.12}$$

and $\boldsymbol{\Delta}$ the $MN \times MN$ diagonal matrix:

$$\boldsymbol{\Delta}_{k_i, l_i} = diag[z^{-l_1}, z^{-l_1+1}, ..., z^{MN-l_i-1}], \tag{3.13}$$

where $z = e^{\frac{j2\pi(k_i+\tilde{k}_i)}{MN}}$. The matrices $\boldsymbol{\Pi}$ and $\boldsymbol{\Delta}$ model the delays and the Doppler shifts in eq. (3.5), respectively.

At the receiver, the received signal samples $\boldsymbol{r}$ are transformed into time-frequency domain symbols, $\boldsymbol{R} = vec^{-1}(\boldsymbol{r})$, and further into delay-Doppler domain symbols, as follows:

$$\boldsymbol{Y} = \boldsymbol{F}_M^H(\boldsymbol{F}_M \boldsymbol{G}_{rx} \boldsymbol{R})\boldsymbol{F}_N. \tag{3.14}$$

To achieve this, an M-point FFT followed by an SFFT is applied. $\boldsymbol{G}_{rx} \in \mathbb{C}^{M \times M}$ is a diagonal matrix containing the receiver pulse. In vector form, the received signal in the delay-Doppler domain can be expressed as:

$$\boldsymbol{y} = (\boldsymbol{F}_N \otimes \boldsymbol{G}_{rx})\boldsymbol{r}. \tag{3.15}$$

Substituting the transmitted signal vector $\boldsymbol{r}$ into Eq. (3.10), we obtain:

$$\begin{aligned}\boldsymbol{y} &= (\boldsymbol{F}_N \otimes \boldsymbol{G}_{rx})(\boldsymbol{H}\boldsymbol{s} + \boldsymbol{w}) \\ &= (\boldsymbol{F}_N \otimes \boldsymbol{G}_{rx})\boldsymbol{H}(\boldsymbol{F}_N^H \otimes \boldsymbol{G}_{tx})\boldsymbol{x} + (\boldsymbol{F}_N \otimes \boldsymbol{G}_{rx})\boldsymbol{w} \\ &= \boldsymbol{H}_{eff}\boldsymbol{x} + \widetilde{\boldsymbol{w}},\end{aligned} \tag{3.16}$$

where $\widetilde{\boldsymbol{w}} = (\boldsymbol{F}_N \otimes \boldsymbol{G}_{rx})\boldsymbol{w}$ represents the AWGN noise vector with zero mean and variance σ_0^2 and $\boldsymbol{H}_{eff}$ is a sparse matrix representing the effective channel matrix, as:

$$\boldsymbol{H}_{eff} = (\boldsymbol{F}_N \otimes \boldsymbol{G}_{rx})\boldsymbol{H}(\boldsymbol{F}_N^H \otimes \boldsymbol{G}_{tx}) \tag{3.17}$$

Due to the sparsity of $\boldsymbol{H}_{eff}$, low-complexity detector algorithms can be implemented to estimate symbols effectively (RAVITEJA *et al.*, 2018). These algorithms, primarily based on message passing, are well-suited for this purpose. In our case, it used a representation of the matrix $\boldsymbol{H}_{eff}$ by a factor graph. Section 4 provides further details on the various message passing algorithms employed in this thesis.

3.3.2 Vector analysis for overlay OTFS

When incorporating cyclic prefixes (CP) after each OFDM symbol, we have $T = T_u + T_L$. Knowing that $T = 1/\Delta f + T_L$, which leads to $T\Delta f = 1 + \Delta f T_L = 1 + L/M$, the signal output of the OTFS transmitter can be expressed as:

$$s(t) = \sum_{m=0}^{M-1}\sum_{n=0}^{N-1} X^{FT}[m,n]\, e^{j2\pi m\Delta f(t-T_L-nT)}\, g_{tx}(t-nT) \tag{3.18}$$

In this case, as depicted in Fig. 11, we consider the OFDM system with CP-based OTFS, featuring a single transmit antenna and a single receive antenna—essentially a SISO model (HASHIMOTO *et al.*, 2021). To achieve this, we append a CP of size L to each OFDM symbol by incorporating the matrix $\boldsymbol{L}$ into the equation of the transmitted signal (3.8), which is rewritten as $\boldsymbol{S}_{cp}$:

$$\boldsymbol{S}_{cp} = \boldsymbol{L}\boldsymbol{G}_{tx}\boldsymbol{X}\boldsymbol{F}_N^H, \tag{3.19}$$

where the $(M+L)\times M$ matrix $\boldsymbol{L} = \begin{bmatrix} \mathbf{0}_{L\times M-L} & \boldsymbol{I}_L \\ \multicolumn{2}{c}{\boldsymbol{I}_M} \end{bmatrix}$ denotes the operator for appending the CP. By employing the identity $vec(\boldsymbol{A}_{K\times L}\boldsymbol{B}_{L\times M}) = (\boldsymbol{I}_M \otimes \boldsymbol{A})\boldsymbol{b} = (\boldsymbol{B} \otimes \boldsymbol{I}_M)\boldsymbol{a}$, for parallel-to-serial conversion, the transmitted signal vector can be expressed as:

$$\begin{aligned} \boldsymbol{s}_{cp} &= vec(\boldsymbol{L}\boldsymbol{G}_{tx}\boldsymbol{X}\boldsymbol{F}_N^H) \\ &= (\boldsymbol{I}_N \otimes \boldsymbol{L}\boldsymbol{G}_{tx})vec(\boldsymbol{X}\boldsymbol{F}_N^H) \\ &= \boldsymbol{L}_{cp}\boldsymbol{x}. \end{aligned} \tag{3.20}$$

where $\boldsymbol{L}_{cp} = (\boldsymbol{I}_N \otimes \boldsymbol{L}\boldsymbol{G}_{tx})(\boldsymbol{F}_N^H \otimes \boldsymbol{I}_M)$.

At the receiver, the received vector $\boldsymbol{r}$ undergoes transformation into the time-frequency domain, resulting in an $(M+L)\times N$ matrix $\boldsymbol{R} = vec^{-1}(\boldsymbol{r})$.

Subsequently, we apply the CP removal operation to obtain the received matrix:

$$[\boldsymbol{r}_0, \boldsymbol{r}_1, \ldots, \boldsymbol{r}_{N-1}] = \boldsymbol{L}_R\boldsymbol{R} \tag{3.21}$$

where the $M\times(M+L)$ matrix $\boldsymbol{L}_R = \begin{bmatrix} \mathbf{0}_{M\times L} & \boldsymbol{I}_M \end{bmatrix}$ is used to eliminate all the CP.

The n^{th} received OFDM symbol $\boldsymbol{r}_n \in \mathbb{C}^M$ after CP removal can be expressed as:

$$\boldsymbol{r}_n = \boldsymbol{H}_n\boldsymbol{s}_n + \boldsymbol{w}_n \tag{3.22}$$

where $\boldsymbol{H}_n$ represents n^{th} circulant channel matrix of size the $M\times M$.

Matrix $\boldsymbol{H}_n$ can be expressed as

$$\boldsymbol{H}_n = \sum_{i=1}^{P} h_i \boldsymbol{\Delta}_{n,k_i,l_i}\boldsymbol{\Pi}^{l_i} \tag{3.23}$$

with $\boldsymbol{\Pi}$ the $M\times M$ permutation matrix (forward cyclic shift),

$$\mathbf{\Pi} = \begin{bmatrix} 0 & \dots & 0 & 1 \\ 1 & \ddots & 0 & 0 \\ \vdots & \ddots & \ddots & \vdots \\ 0 & \dots & 1 & 0 \end{bmatrix} \tag{3.24}$$

and $\mathbf{\Delta}_{n,k_i,l_i}$ is the $M \times M$ diagonal matrix defined as follows:

$$\mathbf{\Delta}_{n,k_i,l_i} = diag\left[z^{(M+L)n+L-l_i}, z^{(M+L)n+L-l_i+1}, ..., z^{(M+L)(n+1)-l_i-1}\right] \tag{3.25}$$

where $z = e^{\frac{j2\pi(k_i+\tilde{k}_i)}{(M+L)N}}$.

The matrices $\mathbf{\Pi}$ and $\mathbf{\Delta}$ model the delays and the Doppler shifts, respectively.

At each symbol n, the receiver performs an M-point DFT to obtain the frequency domain vector $\boldsymbol{y}_n^{FT}$

$$\begin{aligned} \boldsymbol{y}_n^{FT} &= \boldsymbol{F}_M \boldsymbol{G}_{rx} \boldsymbol{r}_n \\ &= \boldsymbol{F}_M \boldsymbol{G}_{rx} (\boldsymbol{H}_n \boldsymbol{s}_n + \boldsymbol{w}_n) \end{aligned} \tag{3.26}$$

Let us stack the vectors $\boldsymbol{y}_n^{FT}$ in the matrix $\boldsymbol{Y}^{FT}$ as follows :

$$\boldsymbol{Y}^{FT} \triangleq [\boldsymbol{y}_0^{FT}, \boldsymbol{y}_2^{FT}, \dots, \boldsymbol{y}_{N-1}^{FT}] \tag{3.27}$$

This results in:

$$\begin{aligned} \boldsymbol{Y} &= \boldsymbol{F}_M^H \boldsymbol{Y}^{FT} \boldsymbol{F}_N \\ &= \boldsymbol{G}_{rx}[\boldsymbol{H}_0 \boldsymbol{s}_0, \boldsymbol{H}_1 \boldsymbol{s}_1, \dots, \boldsymbol{H}_{N-1} \boldsymbol{s}_{N-1}] \boldsymbol{F}_N + \boldsymbol{G}_{rx}[\boldsymbol{w}_0, \boldsymbol{w}_1, \dots, \boldsymbol{w}_{N-1}] \boldsymbol{F}_N \end{aligned} \tag{3.28}$$

With the following relation

$$\boldsymbol{S} = \boldsymbol{G}_{tx} \boldsymbol{X} \boldsymbol{F}_N^H \tag{3.29}$$

or equivalently:

$$\boldsymbol{s}_n = \boldsymbol{G}_{tx} \boldsymbol{X} \boldsymbol{f}_n^* \qquad \forall n \in \{0, ...N-1\} \tag{3.30}$$

where $\boldsymbol{f}_n$ is the n^{th} column of $\boldsymbol{F}_N$.

Replacing equation (3.30) into equation (3.28), we obtain:

$$\boldsymbol{Y} = \sum_{n=0}^{N-1} (\boldsymbol{G}_{rx}\boldsymbol{H}_n\boldsymbol{G}_{tx}\boldsymbol{X}\boldsymbol{f}_n^*\boldsymbol{f}_n^T + \boldsymbol{G}_{rx}\boldsymbol{w}_n\boldsymbol{f}_n^T) \tag{3.31}$$

Similarly to the standalone case, we can express the vectorized version of $\boldsymbol{Y}$ from equation (3.28) as follows:

$$\begin{aligned}\boldsymbol{y} &= vec(\boldsymbol{Y})\\ &= (\boldsymbol{F}_N \otimes \boldsymbol{G}_{rx})(\boldsymbol{H}\boldsymbol{s} + \boldsymbol{w})\\ &= (\boldsymbol{F}_N \otimes \boldsymbol{G}_{rx})\boldsymbol{H}(\boldsymbol{F}_N^H \otimes \boldsymbol{G}_{tx})\boldsymbol{x} + (\boldsymbol{F}_N \otimes \boldsymbol{G}_{rx})\boldsymbol{w}\\ &= \boldsymbol{H}_{eff}\boldsymbol{x} + \tilde{\boldsymbol{w}} \end{aligned} \tag{3.32}$$

where we have defined the $MN \times MN$ matrix $\boldsymbol{H} = blkdiag(\boldsymbol{H}_0, \boldsymbol{H}_1, \ldots, \boldsymbol{H}_{N-1})$. $\boldsymbol{s}$ represents the vector obtained from the vectorization of $\boldsymbol{S}$, $\boldsymbol{s} = vec(\boldsymbol{S})$ and $\boldsymbol{w} = [\boldsymbol{w}_0^T, \boldsymbol{w}_1^T, \ldots, \boldsymbol{w}_{N-1}^T]^T$.

The matrix $\boldsymbol{H}_{eff} \triangleq (\boldsymbol{F}_N \otimes \boldsymbol{G}_{rx})\boldsymbol{H}(\boldsymbol{F}_N^H \otimes \boldsymbol{G}_{tx})$ denotes the effective channel matrix and $\tilde{\boldsymbol{w}} = (\boldsymbol{F}_N \otimes \boldsymbol{G}_{rx})\boldsymbol{w}$.

Disregarding the noise term $\boldsymbol{w}_n\boldsymbol{f}_n^T$ and assuming a rectangular pulse ($\boldsymbol{G}_{tx} = \boldsymbol{I}_M$), we can derive each element $Y[l,k]$ of the $M \times N$ matrix $\boldsymbol{Y}$ using equations (3.23) and (3.31).

First, with these constraints in mind, we develop equation (3.31) as follows:

$$\begin{aligned}\boldsymbol{Y} &= \sum_{n=0}^{N-1} \boldsymbol{H}_n\boldsymbol{X}\boldsymbol{f}_n^*\boldsymbol{f}_n^T\\ &= \sum_{n=0}^{N-1} \boldsymbol{\Xi}_n\boldsymbol{\Lambda}_n \end{aligned} \tag{3.33}$$

where

$$\boldsymbol{\Xi}_n[l,k'] \triangleq \sum_{l'=0}^{M-1} \boldsymbol{H}_n[l,l']\boldsymbol{X}[l',k'] \tag{3.34}$$

and

$$\begin{aligned}\boldsymbol{\Lambda}_n[k',k] &\triangleq e^{j2\pi\frac{nk'}{N}}e^{-j2\pi\frac{nk}{N}}\\ &= e^{-j2\pi\frac{n(k-k')}{N}} \end{aligned} \tag{3.35}$$

As a result, each element of the matrix $\boldsymbol{Y}$ can be determined as:

$$\begin{aligned}\boldsymbol{Y}[l,k] &= \sum_{n=0}^{N-1}\sum_{k'=0}^{N-1} \boldsymbol{\Xi}_n[l,k']\boldsymbol{\Lambda}_n[k',k] \\ &= \sum_{n=0}^{N-1}\sum_{k'=0}^{N-1}\sum_{l'=0}^{M-1} \boldsymbol{H}_n[l,l']\boldsymbol{X}[l',k']e^{-j2\pi\frac{n(k-k')}{N}} \\ &= \sum_{k'=0}^{N-1}\sum_{l'=0}^{M-1} \boldsymbol{X}[l',k']\sum_{n=0}^{N-1}\boldsymbol{H}_n[l,l']e^{-j2\pi\frac{n(k-k')}{N}} \\ &= \sum_{k'=0}^{N-1}\sum_{l'=0}^{M-1} \boldsymbol{X}[l',k']\boldsymbol{H}_{l',k'}[l,k] \end{aligned} \tag{3.36}$$

where

$$\begin{aligned}\boldsymbol{H}_{l',k'}[l,k] &\triangleq \sum_{n=0}^{N-1}\boldsymbol{H}_n[l,l']e^{-j2\pi\frac{n(k-k')}{N}} \\ &= \sum_{n=0}^{N-1}\sum_{i=1}^{P} h_i\delta((l-l')_M - l_i)e^{j2\pi(k_i+\tilde{k}_i)\frac{(M+L)n+L-l_i+l}{(M+L)N}}e^{-j2\pi\frac{n(k-k')}{N}} \\ &= \sum_{i=1}^{P} h_i\delta((l-l')_M - l_i)\underbrace{\sum_{n=0}^{N-1} e^{j2\pi(k_i+\tilde{k}_i)\frac{n}{N}}e^{-j2\pi\frac{n(k-k')}{N}}}_{DIRIC(k_i+\tilde{k}_i-(k-k'),N)} e^{j2\pi(k_i+\tilde{k}_i)\frac{L-l_i+l}{(M+L)N}} \\ &= \sum_{i=1}^{P} h_i\delta((l-l')_M - l_i)DIRIC(k_i+\tilde{k}_i-(k-k'),N)e^{j2\pi(k_i+\tilde{k}_i)\frac{L-l_i+l}{(M+L)N}} \end{aligned} \tag{3.37}$$

where $DIRIC(a,N)$ represents the variant of the Dirichlet Kernel function (the sum is only over non-negative integers) and is defined as follows:

$$\begin{aligned}DIRIC(a,N) &\triangleq \sum_{n=0}^{N-1} e^{j2\pi a\frac{n}{N}} \\ &= e^{j\pi a\frac{N-1}{N}}\frac{\sin(\pi a)}{\sin(\pi a/N)}\end{aligned} \tag{3.38}$$

3.4 Simulations: OTFS under high mobility channel

A recent thesis by Gaudio (GAUDIO, 2022) presents a comprehensive comparison between OTFS and OFDM. In this context, we evaluate OTFS modulation in the overlay version and compare it with OFDM modulation in the same high-mobility macrocell channel, assuming that the channel is known to the receiver.

Table 3 outlines the simulation parameters for OTFS to facilitate a comparison with the OFDM system described in the preceding section.

Table 3 – Simulation Parameters for OTFS vs OFDM

Parameter	**Value**
Carrier frequency (f_c)	4 GHz
Subcarrier spacing (Δf)	15 kHz
Number of subcarriers (M)	600
Number of symbols for OTFS (N)	12
CP length (L)	255
Channel model	Urban macrocell
Modulation scheme	4-QAM and 16-QAM
UE speed	330 km/h
Channel estimation	ideal

Source: the author.

As established in the previous section's results for the OFDM system under the Macrocell channel, configuring 600 active subcarriers already provides an adequate sampling rate to generate the channel with all six taps from the adopted model. Therefore, for the purpose of comparing OFDM modulation with OTFS modulation, we exclusively consider this configuration. The results presented in Figures 12 and 13 are derived from simulations involving the transmission of 1000 frames, each containing 12 QAM symbols per subcarrier, and the insertion of a CP with a length of 255 for each frame. Both 4-QAM and 16-QAM modulation schemes are utilized.

Figure 12 illustrates the performance results using a 4-QAM modulation scheme. Data detection techniques are assessed, including ZF, MMSE, and AMP-FO. The choice of the AMP-FO detector was motivated by its favorable complexity-BER trade-off, as elaborated in the subsequent section. Using Eq. (2.19) and (2.18), we compute the estimated symbols in ZF and MMSE employing $\boldsymbol{H}_{eff}$ as follows:

$$\hat{\boldsymbol{x}}_{MMSE} = \left(\frac{\sigma_0^2}{\sigma_d^2}\boldsymbol{I}_M + \boldsymbol{H}_{eff}^H\boldsymbol{H}_{eff}\right)^{-1}\boldsymbol{H}_{eff}^H\boldsymbol{y} \tag{3.39}$$

$$\begin{aligned}\hat{\boldsymbol{x}}_{ZF} &= \left(\boldsymbol{H}_{eff}^H\boldsymbol{H}_{eff}\right)^{-1}\boldsymbol{H}_{eff}^H\boldsymbol{y} \\ &= \boldsymbol{H}_{eff}^{-1}\boldsymbol{y}\end{aligned} \tag{3.40}$$

According to the results shown in Figure 12, OTFS consistently outperforms OFDM modulation across all evaluated detection techniques. The AMP-FO detector stands out, achieving an SNR of 15 dB for a BER of 10^{-6}, whereas the MMSE detector requires an SNR of approximately 19 dB for similar performance. The ZF detector exhibits the poorest performance.

Figure 12 – BER Performance in OFDM and OTFS system on macrocell channel (4-QAM; $M = 600; N = 12; CP = 255$)

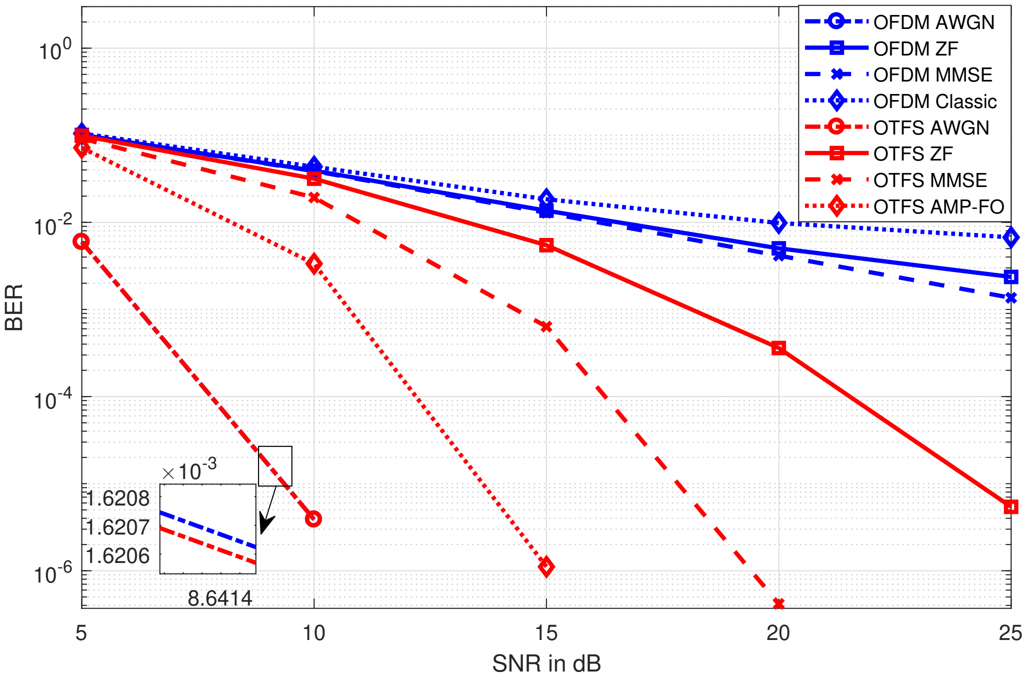

Source: the author.

In the case of 16-QAM modulation, as demonstrated in Figure 13, OTFS once again outperforms OFDM. Due to the higher efficiency of the modulation scheme, the BER performance is naturally worse compared to the 4-QAM case. Nevertheless, in all evaluated detection techniques, OTFS yields superior results to those of OFDM. Once more, the AMP-FO detector surpasses the MMSE and ZF detectors.

This section underscores that OTFS effectively mitigates channel diversity through pre- and post-processing stages in the delay-Doppler domain. While this complexity is increased, it is justified in systems designed for channels with high mobility,

Figure 13 – BER Performance in OFDM and OTFS system on macrocell channel (16-QAM; $M = 600; N = 12; CP = 255$)

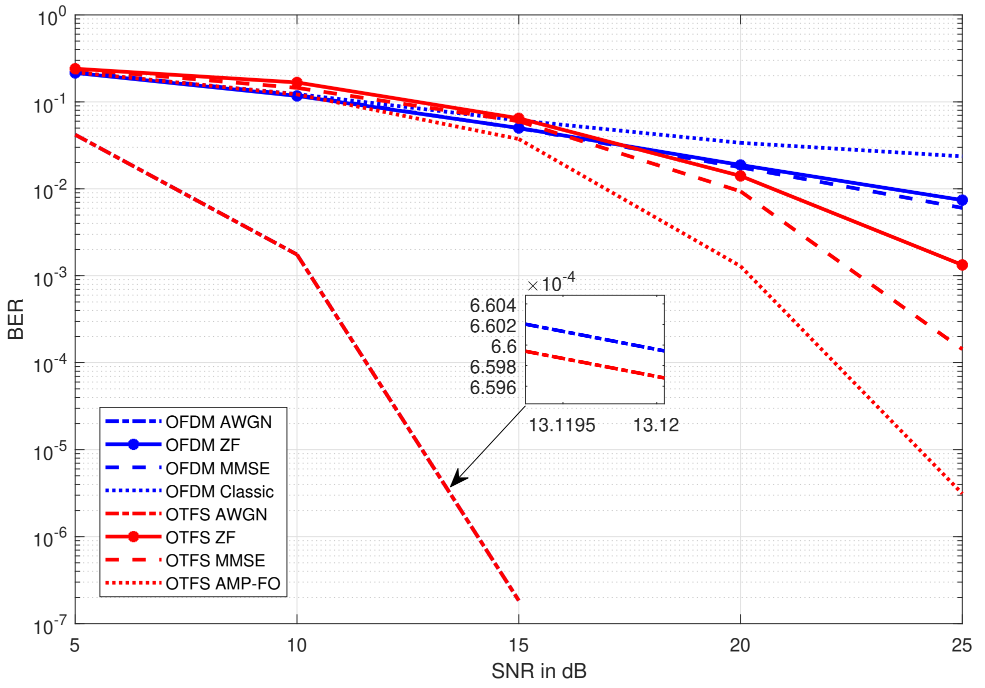

Source: the author.

a crucial requirement for applications in mobile communication systems, such as B5G.

Given the escalating complexity of OTFS modulation and the channel's sparsity, much research is dedicated to identifying low-complexity detectors to address this issue. The following chapter conducts an evaluative study of message-passing-based algorithms to determine the optimal complexity-BER trade-off.

4 LOW-COMPLEXITY ALGORITHMS FOR DATA DETECTION

This chapter focuses on assessing low-complexity techniques tailored to address the high sparsity of the channel's impulse response. Specifically, we delve into message-passing algorithms designed for data detection in a time-varying channel, often referred to as an integer channel. In this scenario, the delay and Doppler scattering values of the channel align well with the Γ grid, enabling the use of OTFS modulation without the need for a guard interval, thereby reducing computational costs. The system model for OTFS, as discussed previously, is given by:

$$\boldsymbol{y} = \boldsymbol{H}_{eff}\, \boldsymbol{x} + \hat{\boldsymbol{w}} \tag{4.1}$$

where $\boldsymbol{y} \in \mathbb{C}^{MN \times 1}$, $\boldsymbol{H}_{eff} \in \mathbb{C}^{MN \times MN}$, $\boldsymbol{x} \in \mathbb{C}^{MN \times 1}$ and $\hat{\boldsymbol{w}} \in \mathbb{C}^{MN \times 1}$

Many estimation and inference challenges in the field of digital communications are effectively represented using graphical models such as Bayesian networks or factor graphs (KSCHISCHANG *et al.*, 2001). A factor graph, a type of bipartite graph, delineates the joint distribution of random variables x_i belonging to a given domain. It consists of two sets of vertices or nodes and a set of branches or edges. These two sets of nodes encompass:

- Variable nodes x_i, symbolized as circles in Figure 14
- Function nodes f_j, represented by squares in Figure 14

An illustrative factor graph is provided in Figure 14.

Figure 14 – Factor graph to MPA

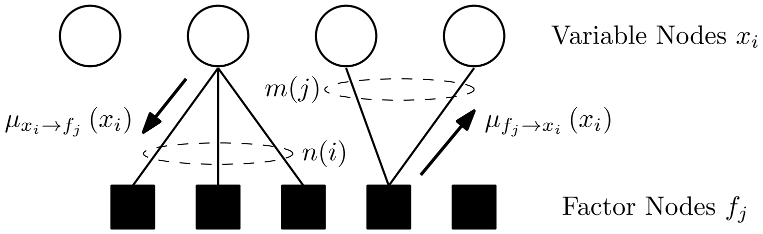

Source: the author.

In this graph, $m(j)$ denotes the set of variable neighbors linked to the factor node f_j, while $n(i)$ signifies the set of factor nodes associated with the variable node x_i.

Given the sparsity of the matrix $\boldsymbol{H}_{eff}$ of size $MN \times MN$, the Eq. equation

(3.16) can be graphically represented using a factor graph comprising $MN = O$ variable nodes and O factor nodes.

The number of branches $d_f(j) = |m(j)|$ converging on a specific function node is denoted as the degree of the factor node f_j. Correspondingly, the number of branches $d_x(i) = |n(i)|$ converging on a particular variable node is referred to as the degree of the variable node x_i. . In our context, since the number of nonzero elements in the rows and columns of $\boldsymbol{H}_{eff}$ equals the number of propagation paths P, the factor graph exhibits regularity, and we have $d_f(j) = d_x(i) = P \; \forall i, j$.

In this context, this chapter's primary contribution lies in introducing a low-complexity algorithm for OTFS data detection based on AMP with first-order (AMP-FO) and assessing its performance in terms of BER and computational complexity compared to other low-complexity algorithms proposed by various authors. The objective is to identify which algorithm offers the most favorable complexity-BER trade-off for OTFS modulation. Additionally, as a secondary contribution, we evaluate the performance in both the SISO and MIMO scenarios. In the subsequent subsections, we provide detailed explanations of the following algorithms based on MPA: the original MPA, AMP with Factor Graph using Gaussian Approximation of Interference (FG-GAI) (SOM *et al.*, 2011), AMP using Gaussian Approximation (AMP-GA), AMP using expectation propagation (AMP-EP), and the introduced AMP-FO algorithm (WU *et al.*, 2014).

4.1 MPA

The fundamental goal of the Message Passing Algorithm (MPA) is to estimate the marginal probabilities μ_{x_i} for all variables x_i.

In MPA, during each iteration, the algorithm computes messages or beliefs that travel from the variable nodes to the factor nodes and then back from the factor nodes to the variable nodes. Typically, these messages are propagated in parallel, moving from one factor node to the next. This order of message passing, when interpreted in the context of a factor graph and the Sum-Product Algorithm (SPA), leads to the message update schedule.

The notations used to describe MPA-based algorithms include: $\mu_{f_j \to x_i}$ representing messages from factor node f_j towards variable node x_i, and $\mu_{x_i \to f_j}$ representing messages from variable nodes x_i towards factor nodes f_j.

These messages or beliefs are functions of variable nodes x_i, either in one direction or the other. The message from x_i to f_j represents the probability that x_i has a specific value, given the observed value of this variable and the values received from the other factor nodes connected to x_i, except for f_j. For a QAM constellation (with Z possible values), the messages typically have Z distinct values, each corresponding to a possible value of x_i.

To initiate this algorithm, we first compute the probability mass functions for each factor node, based on corresponding variable nodes for each value of $\boldsymbol{\alpha_s}$, in the context of a system model $\boldsymbol{y} = \boldsymbol{H}_{eff}\boldsymbol{x} + \boldsymbol{w}$:

$$f_j(y_j|\boldsymbol{x}) \propto \exp\left(\frac{-|y_j - \sum_{l\in m(j)} h_{j,l}\, x_l|^2}{\sigma_0^2}\right), \tag{4.2}$$

where $\boldsymbol{x} \in \mathcal{A}^P$, $h_{j,l}$ represents the element of the j^{th} row and l^{th} column of matrix $\boldsymbol{H}_{eff}$ (channel transfer matrix), σ_0^2 denotes the noise variance, and y_j is the correlated received signal term.

The computation of all messages from factor node f_j to the corresponding variable nodes x_i begins by assuming that all symbols in the alphabet $\mathcal{A}$ have equal probabilities. Then, each message is computed following the sum-product rule (KSCHISCHANG *et al.*, 2001), where the previous product of all messages sent from variable node x_i is combined for each associated factor node f_j:

$$\mu^t_{f_j\to x_i}(x_i = \alpha_s) = \sum_{\sim\, \boldsymbol{x}} \left(f_j(y_j|\boldsymbol{x}) \prod_{l\in m(j)\setminus i} \mu^{t-1}_{x_l\to f_j}(x_l) \right). \tag{4.3}$$

Subsequently, the messages from variable nodes to factor nodes are updated by computing the product of the messages from factor nodes to variable nodes, as follows:

$$\mu^t_{x_i\to f_j}(x_i = \alpha_s) = \prod_{b\in n(i)\setminus j} \mu^t_{f_b\to x_i}(x_i). \tag{4.4}$$

During the message exchange, a normalization process is applied, followed by the introduction of a damping factor (Δ). In this process, the values of the transmitted messages from variable nodes to factor nodes are normalized ($\boldsymbol{\mu}_{x_i\to f_j}$) by adding the corresponding x_i for each QAM symbol. The damping factor is calculated at each iteration (t) by considering the total of normalized messages with an applied weight, as shown in Eq. (4.5).

The application of the damping factor is a technique used to minimize the Bit Error Rate (BER) when determining the optimal number of iterations for the decoding algorithm, based on the density of the $\boldsymbol{H_{eff}}$ matrix.

$$\mu^{t}_{x_i \to f_j}(x_i = \alpha_s) = (1 - \Delta).\mu^{t-1}_{x_i \to f_j}(x_i) + \Delta.\mu^{t}_{x_i \to f_j}(x_i). \tag{4.5}$$

At iteration t, the marginal distribution $\mu^{t}_{x_i}(x_i = \alpha_s)$ can be estimated using the set of incoming messages $\mu^{t}_{f_b \to x_i}(x_i)$

$$\mu^{t}_{x_i}(x_i = \alpha_s) = \frac{\prod_{b \in n(i)} \mu^{t}_{f_b \to x_i}(x_i = \alpha_s)}{\sum_{x_i \in A} \prod_{b \in n(i)} \mu^{t}_{f_b \to x_i}(x_i)}. \tag{4.6}$$

Next, the Log Likelihood Ratio (LLR) calculation is employed to perform a test based on the ratio of probabilities, allowing inference regarding the detection of the received bit sequence. The LLR calculation $\Lambda_{b \to l}$ $(b, l \to f_j, x_i)$ is based on the principles outlined in (110150664.0, 2011) and is tailored for QAM symbols. The complete MPA is provided in pseudo-code in Algorithm 1.

Algorithm 1: MPA algorithm

```
Initialization;
Set $\mu_{f_j \to x_i}(x_i = \alpha_s) = 0$,$\forall x_i \in \mathcal{A}$;
Compute $f_j(y_j|x_i)$ using (4.2), $\forall i \in m(j)$, $\forall x_i \in \mathcal{A}$;
// T iterations
) for $t = 1$ to T do
    for $j = 1$ to $O$ do
        // Computation of messages from Factor Node (FN) to Variable
           Node (VN)
        Compute $\mu^t_{f_j \to x_i}(x_i)$ using (4.3), $\forall i \in m(j)$, $\forall x_i \in \mathcal{A}$;
    end
    for $i = 1$ to $O$ do
        // Computation of messages from VN to FN
        Compute $\mu^t_{x_i \to f_j}(x_i)$ using (4.4), $\forall j \in n(i)$, $\forall x_i \in \mathcal{A}$;
    end
    for $i = 1$ to $O$ do
        // Normalisation of messages from VN to FN
        $\mu_{x_i \to f_j}(x_i) = \frac{\mu_{x_i \to f_j}(x_i)}{\sum_{\alpha_s \in Z} \mu_{x_i \to f_j}(x_i = \alpha_s)}$, $\forall j \in n(i)$, $\forall x_i \in \mathcal{A}$;
        Damping calculation by using equation (4.5);
    end
end
Decision calculation;
```

4.2 Gaussian Approximation of Interference (FG-GAI)

In FG-GAI (SOM *et al.*, 2011), the traditional messages $\mu^t_{f_j \to x_i}(x_i)$ are replaced with Gaussian approximations of the interference. The received signal y_j is expressed as:

$$y_j = h_{j,i}x_i + \underbrace{\sum_{l \in m(j) \backslash i} h_{j,l}x_l + w_j}_{w_{f_j \to x_i}}, \tag{4.7}$$

The interference term $w_{f_j \to x_i}$ is then modeled as a Gaussian variable, characterized by a mean $z_{f_j \to x_i}$ and a variance $\nu_{f_j \to x_i}$.

As in the MPA, the iteration starts with the calculation of messages from the factor node f_j to the variable nodes x_i. The means $z_{f_j \to x_i}$ and variances $\nu_{f_j \to x_i}$ are calculated as follows:

$$\begin{aligned} z^t_{f_j \to x_i} &= \mathbb{E}\{w_{f_j \to x_i}\} \\ &= \sum_{l \in m(j) \backslash i} h_{j,l} \mathbb{E}\{x_l\} \\ &= \sum_{l \in m(j) \backslash i} h_{j,l} \sum_{s=1}^{Z} \mu^{t-1}_{x_l \to f_j}(x_l = \alpha_s) \alpha_s, \end{aligned} \tag{4.8}$$

$$\nu^t_{f_j \to x_i} = \sum_{l \in m(j) \backslash i} |h_{j,l}|^2 \sigma^2(x_l) + \sigma_0^2, \tag{4.9}$$

where $\alpha_s \in \mathcal{A}$, $h_{j,l}$ represents the element of the j^{th} row and l^{th} column of matrix $\boldsymbol{H_{eff}}$, $\mathbb{E}\{x\}$ denotes the expectation of x and $\sigma^2(x_l)$ represents equal the variance of x_l, defined as:

$$\sigma^2(x_l) = \sum_{s=1}^{Z} \mu^{t-1}_{x_l \to f_j}(x_l) |\alpha_s|^2 - \left| \sum_{s=1}^{Z} \mu^{t-1}_{x_l \to f_j}(x_l) \alpha_s \right|^2. \tag{4.10}$$

Subsequently, the variable node x_i updates its probability function, which is conditioned on the corresponding value of the $\boldsymbol{y}$ vector (y_b) for each x_i elonging to a valid symbol in the constellation (alphabet $\mathcal{A}$). It then sends this information to f_j, which responds with the mean and variance of the other x_i values.

Next, the messages from the variable nodes to the factor nodes are updated. The probabilities for each possible symbol $\mu^t_{x_i \to f_j}(x_i = \alpha_s)$ are calculated based on the means and variances corresponding to the factor nodes linked to x_i, as follows:

$$\mu^t_{x_i \to f_j}(x_i = \alpha_s) \propto \prod_{b \in n(i) \backslash j} \exp\left(\frac{-|y_b - z^t_{f_b \to x_i} - h_{b,i}\alpha_s|^2}{\nu^t_{f_b \to x_i}} \right). \tag{4.11}$$

The marginal distribution $\mu^t_{x_i}(x_i)$ can be calculated by considering all the incoming messages:

$$\mu^t_{x_i}(x_i) \propto \prod_{b \in n(i)} \exp\left(\frac{-|y_b - z^t_{f_b \to x_i} - h_{b,i}\alpha_s|^2}{\nu^t_{f_b \to x_i}} \right). \tag{4.12}$$

Algorithm 2: FG-GAI algorithm

```
Initialization;
Set $\{\mu_{x_i \to f_j}(x_i) = 1/Z,\ z_{f_j \to x_i} = 0, \nu_{f_j \to x_i} = 0\}$;
// T iterations
for $t = 1$ to T do
    for $j = 1$ to $O$ do
        // Computation of messages from FN to VN
        Compute $z^t_{f_j \to x_i}$ using (4.8), $\forall i \in m(j)$;
        Compute $\nu^t_{f_j \to x_i}$ using (4.9), $\forall i \in m(j)$;
    end
    for $i = 1$ to $O$ do
        // Computation of messages from VN to FN
        Compute $\mu^t_{x_i \to f_j}(x_i)$ using (4.11), $\forall j \in n(i)$;
        Damping calculation by (4.5);
    end
    for $i = 1$ to $O$ do
        // Normalization of messages from VN to FN
        $\mu_{x_i \to f_j}(x_i) = \frac{\mu_{x_i \to f_j}(x_i)}{\sum_{\alpha_s \in Z} \mu_{x_i \to f_j}(x_i = \boldsymbol{\alpha}_s)}$, $\forall j \in n(i)$;
    end
end
Computation of LLR;
Decision calculation;
```

4.3 Approximate Message Passing using Gaussian Approximation (AMP-GA)

Another simplification of MPA utilizing Gaussian Approximation is presented by (WU *et al.*, 2014), known as Approximate Message Passing Using Gaussian Approximation (AMP-GA). In AMP-GA, the messages containing means and variances of the variable nodes are updated from the messages of factor nodes through the calculation of a complex Gaussian function.

Let us denote $\mu^t_{x_i \to f_j}(x_i)$ as the message sent from the variable node x_i to the factor node f_j in the t^{th} iteration, and let us denote $\mu^t_{f_j \to x_i}(x_i)$ as the message from the factor node f_j to the variable node x_i. Then, the message update rules are given by Eq. (4.3) and Eq. (4.4).

Given that symbols belong to a discrete set of QAM symbols ($\boldsymbol{\alpha}_s \in \mathcal{A}$), calculating the messages typically involves significant complexity in marginalizing a random vector $\boldsymbol{x}\backslash x_i$. To address this complexity, as proposed in (WU *et al.*, 2014), AMP-GA applies the Kullback-Leibler divergence criterion to calculate parameters $\hat{x}^t_{x_i \to f_j}$ (mean of the projection distribution) and $\hat{\tau}^t_{x_i \to f_j}$ (variance of the projection distribution). The updated messages from the factor nodes to variable nodes are then given by:

$$\hat{x}^t_{x_i \to f_j} = \sum_{\boldsymbol{\alpha}_s \in A} \boldsymbol{\alpha}_s \mu^t_{x_i \to f_j}(x_i = \boldsymbol{\alpha}_s). \tag{4.13}$$

$$\hat{\tau}^t_{x_i \to f_j} = \sum_{\boldsymbol{\alpha}_s \in A} |\boldsymbol{\alpha}_s|^2 \mu^t_{x_i \to f_j}(x_i = \boldsymbol{\alpha}_s) - |\hat{x}^t_{x_i \to f_j}|^2. \tag{4.14}$$

Treating x_i as a continuous random variable and approximating the message as a complex Gaussian function, $\mu^t_{f_j \to x_i}(x_i)$ can be determined through integration in Eq. equation (4.3), as follows:

$$\begin{aligned} \mu^t_{f_j \to x_i}(x_i) &= \sum_{\boldsymbol{x}\backslash x_i} f_j(y_j|\boldsymbol{x}) \prod_{l \in m(j)\backslash i} \mathcal{N}_{\mathbb{C}}\left(x_l; \hat{x}^t_{x_l \to f_j}, \hat{\tau}^t_{x_l \to f_j}\right) \\ &\approx \mathcal{N}_{\mathbb{C}}\left(h_{j,i} x_i; z^t_{f_j \to x_i}, \nu^t_{f_j \to x_i}\right), \end{aligned} \tag{4.15}$$

where $\mathcal{N}_{\mathbb{C}}(x; \hat{x}; \hat{\tau}) \triangleq (\pi\hat{\tau})^{-1} \exp(-|x - \hat{x}|^2/\hat{\tau})$ denotes a complex Gaussian function. The parameters $z^t_{f_j \to x_i}$ (mean messages from factor nodes to variable nodes) and $\nu^t_{f_j \to x_i}$ (variance messages from factor nodes to variable nodes) are defined as:

$$z^t_{f_j \to x_i} = y_j - \sum_{l \in m(j)\backslash i} h_{j,l} \hat{x}^t_{x_l \to f_j}. \tag{4.16}$$

$$\nu^t_{f_j \to x_i} = \sigma_n^2 + \sum_{l \in m(j)\backslash i} |h_{j,l}|^2 \hat{\tau}^t_{x_l \to f_j}. \tag{4.17}$$

Now, by substituting $\mu^t_{f_j \to x_i}(x_i) = \mathcal{N}_{\mathbb{C}}\left(h_{j,i} x_i; z^t_{f_j \to x_i}, \nu^t_{f_j \to x_i}\right)$ into Eq. (4.4), the messages $\mu^t_{x_i \to f_j}(x_i)$ can be normalized as follows:

$$\mu^t_{x_i \to f_j}(x_i) = \frac{\mathcal{N}_{\mathbb{C}}\left(x_i; \zeta^{t-1}_{x_i \to f_j}, \gamma^{t-1}_{x_i \to f_j}\right)}{\sum_{x_i \in A} \mathcal{N}_{\mathbb{C}}\left(x_i; \zeta^{t-1}_{x_i \to f_j}, \gamma^{t-1}_{x_i \to f_j}\right)}, \tag{4.18}$$

where $\gamma^{t-1}_{x_i \to f_j}$ (variance messages from variables nodes to factor nodes) and $\zeta^{t-1}_{x_i \to f_j}$ (means messages from variables nodes to factor node) are given by:

$$\gamma^t_{x_i \to f_j} = \left(\sum_{b \in n(i) \backslash j} \frac{|h_{b,i}|^2}{\nu^t_{f_b \to x_i}} \right)^{-1}. \tag{4.19}$$

$$\zeta^t_{x_i \to f_j} = \gamma^t_{x_i \to f_j} \sum_{b \in n(i) \backslash j} \frac{h^*_{b,i} z^t_{f_b \to x_i}}{\nu^t_{f_b \to x_i}}. \tag{4.20}$$

The marginal distribution $\mu_{x_i}^t(x_i)$ can be determined as follows:

$$\mu^t_{x_i}(x_i = \boldsymbol{\alpha}_s) \propto \exp\left(-\frac{|\alpha_s \; - \; \zeta^t_{x_i}|^2}{\gamma^t_{x_i}} \right), \tag{4.21}$$

where $\gamma^t_{x_i}$ and $\zeta^t_{x_i}$ represent the estimated mean and variance of x_i:

$$\gamma^t_{x_i} = \left(\sum_{b \in n(i)} \frac{|h_{b,i}|^2}{\nu^t_{f_b \to x_i}} \right)^{-1}. \tag{4.22}$$

$$\zeta^t_{x_i} = \gamma^t_{x_i} \sum_{b \in n(i)} \frac{h^*_{b,i} z^t_{f_b \to x_i}}{\nu^t_{f_b \to x_i}}. \tag{4.23}$$

Algorithm 3: AMP-GA algorithm

```
Initialization;
Set $\left\{\zeta^0_{x_i\to f_j}(x_i) = 0,\ \gamma^0_{x_i\to f_j} = 1000\right\}$;
Set $\left\{\hat{x}^0_{x_i\to f_j} = 0,\ \hat{\tau}^0_{x_i\to f_j} = 0,\ z^0_{f_j\to x_i} = 0, \nu^0_{f_j\to x_i} = 0\right\}$;
// T iterations
for $t = 1$ to T do
    for $i = 1$ to $O$ do
        // Computation of messages from VN to FN
        Compute $\mu^t_{x_i\to f_j}(x_i)$ using (4.18), $\forall j \in n(i)$;
        Compute $\hat{x}^t_{x_i\to f_j}$ using (4.13), $\forall j \in n(i)$;
        Compute $\hat{\tau}^t_{x_i\to f_j}$ using (4.14), $\forall j \in n(i)$;
    end
    for $j = 1$ to $O$ do
        // Computation of messages from FN to VN
        Compute $z^t_{f_j\to x_i}$ using (4.16), $\forall i \in m(j)$;
        Compute $\nu^t_{f_j\to x_i}$ using (4.17), $\forall i \in m(j)$;
    end
    for $i = 1$ to $O$ do
        // Computation of messages from VN to FN
        Compute $\gamma^t_{x_i\to f_j}$ using (4.19), $\forall j \in n(i)$;
        Compute $\zeta^t_{x_i\to f_j}$ using (4.20), $\forall j \in n(i)$;
        Damping calculation by (4.5);
    end
end
Computation of LLR;
Decision calculation;
```

4.4 AMP simplified by Expectation Propagation (AMP-EP)

AMP-EP, proposed by (WU *et al.*, 2014), offers an alternative to reduce the computational complexity found in AMP-GA when calculating messages from variable nodes to factor nodes, $\mu^t_{x_i\to f_j}(x_i)$, as shown in Eq. (4.18). Instead of these messages, AMP-EP introduces the concept of "symbol belief" ($\beta^t(x_i)$), approximated as a Gaussian probability density function (PDF) as follows:

$$\begin{aligned}\beta^t(x_i) &\triangleq \frac{\prod_{b\in n(i)} \mu^{t-1}_{f_b\to x_i}(x_i)}{\sum_{x_i\in A}\prod_{b\in n(i)} \mu^{t-1}_{f_b\to x_i}(x_i)}\\ &\approx \frac{\prod_{b\in n(i)} \mathcal{N}_{\mathbb{C}}\left(h_{b,i}x_i; z^{t-1}_{f_b\to x_i}, \nu^{t-1}_{f_b\to x_i}\right)}{\sum_{x_i\in A}\prod_{b\in n(i)} \mathcal{N}_{\mathbb{C}}\left(h_{b,i}x_i; z^{t-1}_{f_b\to x_i}, \nu^{t-1}_{f_b\to x_i}\right)}.\end{aligned} \tag{4.24}$$

Thus, in this approach, the message $\mu^t_{x_i\to f_j}(x_i)$ is replaced by the symbol belief that is based on a Gaussian Probability Density Function (PDF). Essentially, we have an approximate message $\mu^t_{x_i\to f_j}(x_i)$ calculated from an approximate symbol belief $\beta^t(x_i)$. Once the symbol beliefs for each variable node are calculated, the algorithm proceeds to compute parameters $\hat{x}^t_{x_i}$ (means messages) and $\hat{\tau}^t_{x_i}$ (variance messages), followed by the exchange of messages from variable nodes to factor nodes ($\hat{x}^t_{x_i\to f_j}$ and $\hat{\tau}^t_{x_i\to f_j}$). The calculation of these parameters involves updating their values using the calculated belief symbols as follows:

$$\hat{x}^t_{x_i} = \sum_{\boldsymbol{\alpha}_s\in A} \boldsymbol{\alpha}_s \beta^t(\boldsymbol{\alpha}_s). \tag{4.25}$$

$$\hat{\tau}^t_{x_i} = \sum_{\boldsymbol{\alpha}_s\in A} |\boldsymbol{\alpha}_s|^2 \beta^t(\boldsymbol{\alpha}_s) - |\hat{x}^t_{x_i}|^2. \tag{4.26}$$

Finally, $\hat{x}^t_{x_i\to f_j}$ and $\hat{\tau}^t_{x_i\to f_j}$, the mean and variance messages from the variable nodes to the factor nodes are obtained as follows:

$$\hat{\tau}^t_{x_i\to f_j} = \left(\frac{1}{\hat{\tau}^t_{x_i}} - \frac{|h_{j,i}|^2}{\nu^{t-1}_{f_j\to x_i}}\right)^{-1}. \tag{4.27}$$

$$\hat{x}^t_{x_i\to f_j} = \hat{\tau}^t_{x_i\to f_j}\left(\frac{\hat{x}^t_{x_i}}{\hat{\tau}^t_{x_i}} - \frac{h^*_{j,i} z^{t-1}_{f_j\to x_i}}{\nu^{t-1}_{f_j\to x_i}}\right). \tag{4.28}$$

The messages from the factor nodes to the variable nodes are updated with the values of $\hat{\tau}^t_{x_i\to f_j}$ and $\hat{x}^t_{x_i\to f_j}$ previously computed. As a result, the messages of variance ($\nu^t_{f_j\to x_i}$) and means ($z^t_{f_j\to x_i}$) will be used as input parameters for the calculation of the Gaussian PDF and thus will update the symbols belief $\beta^t(x_i)$ that will be the basis of calculation of the next iteration. The messages $z^t_{f_j \to x_i}$ and $\nu^t_{f_j \to x_i}$ are computed by Eq. (4.16) and Eq. (4.17).

Then, the marginal distribution $\mu^t_{x_i}(x_i)$ can be derived directly from the symbol belief $\beta^t(x_i)$ and the LLR can be obtained as in the MPA.

Algorithm 4: AMP-EP algorithm

```
Initialization;
Set $\left\{z^0_{f_j \to x_i} = 0, \nu^0_{f_j \to x_i} = 1000\right\}$;
Set $\left\{\hat{x}^0_{x_i} = 0,\ \hat{\tau}^0_{x_i} = 0, \hat{x}^0_{x_i \to f_j} = 0,\ \hat{\tau}^0_{x_i \to f_j} = 0\right\}$;
// T iterations
for $t = 1$ to T do
    for $i = 1$ to $O$ do
        Compute $\beta^t(x_i)$ using (4.24), $\forall j \in n(i)$;
    end
    for $j = 1$ to $O$ do
        // Computation of messages from FN to VN
        Compute $\hat{x}^t_{x_i}$ using (4.25), $\forall i \in m(j)$;
        Compute $\hat{\tau}^t_{x_i}$ using (4.26), $\forall i \in m(j)$;
        Compute $\hat{x}^t_{x_i \to f_j}$ using (4.27), $\forall i \in m(j)$;
        Compute $\hat{\tau}^t_{x_i \to f_j}$ using (4.28), $\forall i \in m(j)$;
    end
    for $i = 1$ to $O$ do
        // Computation of messages from VN to FN
        Compute $z^t_{f_j \to x_i}$ using (4.16), $\forall j \in n(i)$;
        Compute $\nu^t_{f_j \to x_i}$ using (4.17), $\forall j \in n(i)$;
        Damping calculation by (4.5);
    end
end
Computation of LLR;
Decision calculation;
```

4.5 AMP simplified by First-Order (AMP-FO)

AMP-FO represents a further simplification of AMP-EP, the last alternative of MPA for the reduction of complexity proposed by (WU *et al.*, 2014) is the AMP-FO. In this algorithm, messages are rewritten following recursive updates, with negligible terms omitted in the large system limit.

To adapt to OTFS decoding, the standard messages in Eq. (4.18) are rewritten as follows:

$$\mu_{x_i}^{t}(x_i) = \frac{\mathcal{N}_{\mathbb{C}}\left(x_i; \zeta_{x_i}^{t-1}, \gamma_{x_i}^{t-1}\right)}{\sum_{x_i \in A} \mathcal{N}_{\mathbb{C}}\left(x_i; \zeta_{x_i}^{t-1}, \gamma_{x_i}^{t-1}\right)}, \tag{4.29}$$

where $\gamma_{x_i}^{t-1}$ (variance messages from variables nodes) and $\zeta_{x_i}^{t-1}$ (means messages from variables nodes) are the messages exchanged from variables nodes to factor nodes are given by:

$$\gamma_{x_i}^{t} = \left(\sum_{b \in n(i)} \frac{|h_{b,i}|^2}{\nu_{f_b}^{t}}\right)^{-1}. \tag{4.30}$$

$$\zeta_{x_i}^{t} = \hat{x}_{x_i}^{t} + \gamma_{x_i}^{t} \sum_{b \in n(i)} \frac{h_{b,i}^{*}\, z_{f_b}^{t}}{\nu_{f_b}^{t}}. \tag{4.31}$$

with $z_{f_b}^{t}$ and $\nu_{f_b}^{t}$ the means and variance messages from factor nodes to variable nodes, respectively. To initiate the message exchange from factor nodes to variable nodes, Eq. (4.29) is updated for all variable nodes. Then, the mean and variance of the projection distribution for each symbol in the QAM alphabet are calculated as:

$$\hat{x}_{x_i}^{t} = \sum_{\boldsymbol{\alpha}_s \in A} \boldsymbol{\alpha}_s \mu_{x_i}^{t}(x_i = \boldsymbol{\alpha}_s). \tag{4.32}$$

$$\hat{\tau}_{x_i}^{t} = \sum_{\boldsymbol{\alpha}_s \in A} |\boldsymbol{\alpha}_s|^2 \mu_{x_i}^{t}(x_i = \boldsymbol{\alpha}_s) - |\hat{x}_{x_i}^{t}|^2. \tag{4.33}$$

Next, the means and variances of the messages exchanged from factor nodes to variable nodes are calculated as follows:

$$z_{f_j}^t = y_j - \sum_{l \in m(j)} h_{j,l}\, \hat{x}_{x_l}^t + z_{f_j}^{t-1} \frac{\sum_{l' \in m(j)} \hat{\tau}_{x_{l'}}^t |h_{j,l'}|^2}{\nu_{f_j}^{t-1}}. \tag{4.34}$$

$$\nu_{f_j}^t = \sigma_n^2 + \sum_{l \in m(j)} |h_{j,l}|^2\, \hat{\tau}_{x_l}^t. \tag{4.35}$$

Algorithm 5: AMP-FO algorithm

```
Initialization;
Set $\left\{z^0_{f_j \to x_i} = 0, \nu^0_{f_j \to x_i} = 1000\right\}$;
Set $\{\zeta^0_{x_i} = 0, \gamma^0_{x_i} = 1000\}$;
// T iterations
for $t = 1$ to T do
    for $i = 1$ to $O$ do
        // Computation of messages of FN
        Compute $\mu^t_{x_i(x_i)}$ using (4.29);
        Compute $\hat{x}^t_{x_i}$ using (4.32);
        Compute $\hat{\tau}^t_{x_i}$ using (4.33);
    end
    for $j = 1$ to $O$ do
        // Computation of messages of VN
        Compute $z^t_{f_j}$ using (4.34);
        Compute $\nu^t_{f_j}$ using (4.35);
    end
    for $i = 1$ to $O$ do
        // Computation of messages of FN
        Compute $\gamma^t_{x_i}$ using (4.30);
        Compute $\zeta^t_{x_i}$ using (4.31);
        Damping calculation by (4.5);
    end
end
Computation of LLR;
Decision calculation;
```

4.6 Complexity Analysis

In this section, we analyze the complexity of the considered algorithms by counting the required number of Floating-point Operations (FLOP). FLOP counts are obtained by adding the arithmetic operations associated with the most deeply nested statements in an algorithm (GOLUB; LOAN, 1996). We have previously presented the simplifications introduced by each algorithm, starting from MPA, followed by FG-GAI, AMP-GA, AMP-EP, and AMP-FO (from the most complex to the least complex algorithm). We evaluate the complexity of the algorithms based on the size of the used Z-QAM modulation, the number of paths P and the number of VNs and FNs O.

All the message passing algorithms have a preprocessing step to compute the square norms $|h_{j,l}|^2$, which requires $3PO$ FLOPs.

The complexity of MPA and FG-GAI primarily arises from the message exchange between VNs and FNs. However, MPA also includes an additional preprocessing step for calculating $f_j(y_j|x_i)$, which requires $(14P-15)ZO$ FLOPs. The processing of the $\mu^t_{f_j \to x_i}$ messages requires $(Z^{(P-1)}-1)(P-1)ZPO$ FLOPs, while the calculation $\mu^t_{x_i \to f_j}$ requires $(P-2)ZPO$ FLOPs for each iteration. The FG-GAI needs $[6Z^2-4Z+(2Z+2)P-7]PO$ FLOPs to calculate $z^t_{f_j \to x_i}$ and $\nu^t_{f_j \to x_i}$, as well as $[(15P-1)Z-1]PO$ FLOPs to compute $\mu^t_{x_i}(x_i)$.

The algorithms AMP-GA, AMP-EP, and AMP-FO each consist of three steps following the preprocessing step. In the VN messages step, AMP-GA requires $15ZPO$ FLOPs to compute $\{\mu^t_{x_i \to f_j}, \hat{x}^t_{x_i \to f_j}, \hat{\tau}^t_{x_i \to f_j}\}$, AMP-EP requires $(16P+Z-1)O$ FLOPs to compute $\beta(x_i)^t$ and AMP-FO needs $(15Z+2)O$ FLOPs to compute $\{\mu_{x_i}(x_i)^t, \hat{x}^t_{x_i}, \hat{\tau}^t_{x_i}\}$. In the FNs step, calculating $\{z^t_{f_j \to x_i}, \nu^t_{f_j \to x_i}\}$ in AMP-GA needs $(10P-10)PO$ FLOPs, computing $\{\hat{x}^t_{x_i}, \hat{\tau}^t_{x_i}, \hat{x}^t_{x_i \to f_j}, \hat{\tau}^t_{x_i \to f_j}\}$ AMP-EP needs $(16P+Z-1)O$ FLOPs and AMP-FO $(12P+4)O$ FLOPs to calculate $\{z^t_{f_j}, \nu^t_{f_j}\}$. Finally, in the update of messages from VNs, AMP-GA needs $(12P-12)PO$ FLOPs to compute $\{\gamma^t_{x_i \to f_j}, \zeta^t_{x_i \to f_j}\}$, AMP-EP needs $(10P-10)PO$ FLOPs to evaluate $\{z^t_{f_j \to x_i}, \nu^t_{f_j \to x_i}\}$, and AMP-FO needs $(12P+2)O$ FLOPs to calculate $\{\gamma^t_{x_i}, \zeta^t_{x_i}\}$.

Table 4 displays the number of total FLOPs per iteration for each algorithm.

Table 4 – Complexity by Total Number of FLOPs per Iteration

Algorithm	**FLOPs**
MPA	$[(Z^{P-1})(P-1)+P+12]ZPO-15ZO$
FG-GAI	$[6Z^2+(15P-5)Z+(2Z+2)P-5]PO$
AMP-GA	$(15Z+22P-19)PO$
AMP-EP	$(7Z+16P)O+(10P+11)PO$
AMP-FO	$(15Z+24P+8)O+3PO$

Source: the author.

Based on the expressions in Table 4, Figure 15 illustrates the complexity in terms of FLOPs as a function of the constellation size Z for each algorithm. This evaluation assumes $P = 4$ paths, 64 subcarriers with 64 symbols ($O = 4096$). The same set of parameters will be used to evaluate the bit error rate performance in this study.

Figure 15 – Complexity evaluation of the studied algorithms

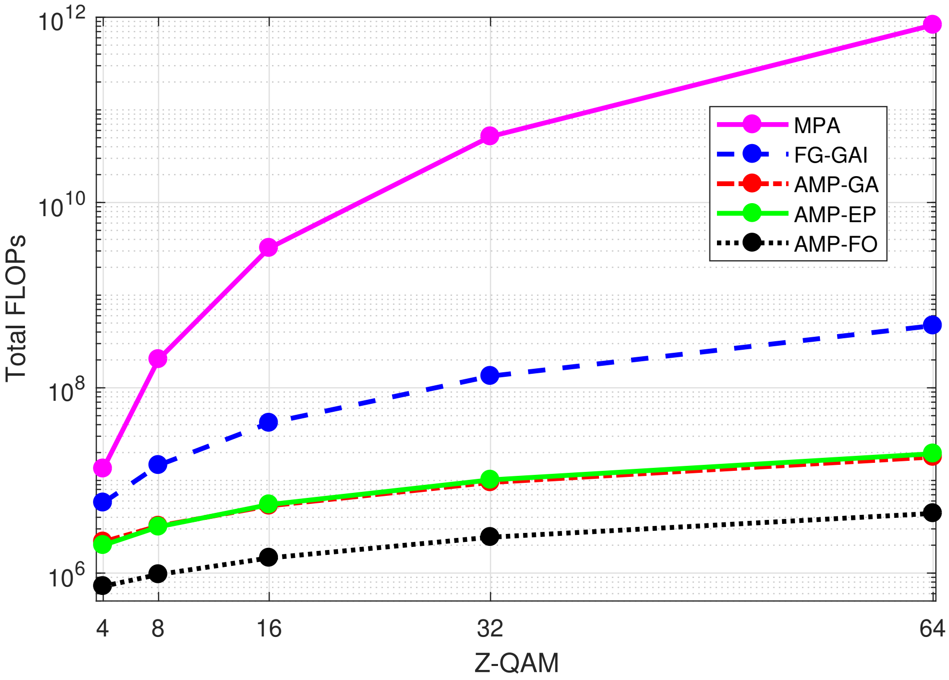

Source: the author.

As expected, Figure 15 shows that the MPA algorithm is the most complex, with its complexity considerably increasing as Z grows. In contrast, AMP-FO is the least complex, with its complexity increasing more slowly with increasing constellation size. FG-GAI, which replaces $\mu_{f_j \to x_i}$ with means and variances, significantly reduces complexity, achieving a complexity reduction factor of 75 at $Z = 16$ compared to MPA. The AMP algorithms further reduce complexity by replacing messages with means and variances. AMP-GA offers a complexity reduction factor of 10 compared to FG-GAI, and finally, AMP-FO achieves the lowest complexity, with its complexity being approximately 30% of that of the EP algorithm. AMP-FO does this by computing only mean and variance information at the VN and FN nodes.

4.7 Extension to MIMO systems

Multiple-Input Multiple-Output (MIMO) systems are employed by using multiple transmit and receive antennas, which can significantly increase capacity and enhance performance in digital communication systems. MIMO systems have the capability to boost data rates through multiplexing and enhance performance and reliability through diversity techniques (GOLDSMITH, 2005). More recently, massive MIMO has emerged as a critical technology to meet the demands of users in terms of performance and Quality of Service (QoS) for next-generation communication systems (ALBREEM *et al.*, 2019).

Given that the OFDM technique permits parallel transmission over multiple subchannels, the combination of OFDM and MIMO technologies results in what is known as a MIMO-OFDM system (TAROKH *et al.*, 2007). Depending on the system configuration, this combination can lead to improvements in signal detection and channel estimation for wireless communications (LI *et al.*, 2002).

Research has shown that the integration of MIMO techniques with OTFS modulation, referred to as MIMO-OTFS, can significantly increase spectral efficiency and robustness in fast-varying MIMO channels (HADANI; MONK, 2018). A study of signal detection and channel estimation in MIMO systems combined with OTFS (MIMO-OTFS) was presented in (RAMACHANDRAN; CHOCKALINGAM, 2018), where the authors applied the Gaussian Approximation of Interference proposed in (SOM *et al.*, 2011) to the factor graph derived from the MIMO-OTFS system model.

In this context, we extend the SISO-OTFS modulation scheme, as described in Section 3, to MIMO-OTFS, building upon the work of (RAMACHANDRAN; CHOCKALINGAM, 2018), as shown in Fig. 16.

The input-output relation of a SISO-OTFS system, as given in Eq. (3.16). , can be extended to MIMO scenarios using spatial multiplexing techniques. Let us denote the vectorized received signal at the j^{th} antenna as $\boldsymbol{y}_j$ and $\boldsymbol{x}_i$ as the vectorized signal at the i^{th} as the vectorized signal at the ith transmit antenna. Consider a MIMO system composed of n_t transmit antennas Eq. (3.16), we derive the following set of

Figure 16 – MIMO-OTFS system diagram

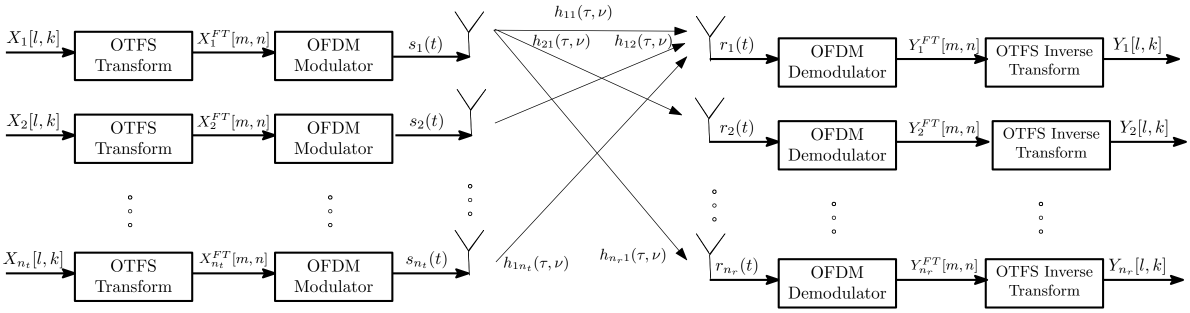

Source: adapted by author from (RAMACHANDRAN; CHOCKALINGAM, 2018).

input-output equations:

$$\begin{aligned}
\boldsymbol{y}_1 &= \boldsymbol{H}_{11}\boldsymbol{x}_1 + \boldsymbol{H}_{12}\boldsymbol{x}_2 + ... + \boldsymbol{H}_{1n_t}\boldsymbol{x}_{n_t} + \tilde{\boldsymbol{w}}_1, \\
\boldsymbol{y}_2 &= \boldsymbol{H}_{21}\boldsymbol{x}_1 + \boldsymbol{H}_{22}\boldsymbol{x}_2 + ... + \boldsymbol{H}_{2n_t}\boldsymbol{x}_{n_t} + \tilde{\boldsymbol{w}}_2, \\
&\vdots \\
\boldsymbol{y}_{n_r} &= \boldsymbol{H}_{n_r1}\boldsymbol{x}_1 + \boldsymbol{H}_{n_r2}\boldsymbol{x}_2 + ... + \boldsymbol{H}_{n_rn_t}\boldsymbol{x}_{n_t} + \tilde{\boldsymbol{w}}_{n_r},
\end{aligned} \tag{4.36}$$

where $\boldsymbol{H}_{ji}^{MN\times MN}$ represents the effective channel vector between the i^{th} transmit antenna and the j^{th} receive antenna.

We can express equation (4.36) in a compact form as:

$$\boldsymbol{y}_{mimo} = \boldsymbol{H}_{mimo}\boldsymbol{x}_{mimo} + \tilde{\boldsymbol{w}}_{mimo}, \tag{4.37}$$

where $\boldsymbol{H}_{mimo}^{n_tn_rMN\times n_tn_rMN}$ represents the MIMO effective channel matrix

$$\boldsymbol{H}_{mimo} = \begin{bmatrix} \boldsymbol{H}_{11} & \boldsymbol{H}_{12} & \cdots & \boldsymbol{H}_{1n_t} \\ \boldsymbol{H}_{21} & \boldsymbol{H}_{22} & \ddots & \boldsymbol{H}_{2n_t} \\ \vdots & \ddots & \ddots & \vdots \\ \boldsymbol{H}_{n_r1} & \boldsymbol{H}_{n_r2} & \cdots & \boldsymbol{H}_{n_rn_t}, \end{bmatrix}, \tag{4.38}$$

and $\boldsymbol{x}_{mimo} = [\boldsymbol{x}_1^T, \boldsymbol{x}_2^T ..., \boldsymbol{x}_{n_t}^T]^T$ denotes the vectorized symbols transmitted vector, $\boldsymbol{y}_{mimo} = [\boldsymbol{y}_1^T, \boldsymbol{y}_2^T ..., \boldsymbol{y}_{n_r}^T]^T$ represents the vectorized received signal vector and $\tilde{\boldsymbol{w}}_{mimo} = [\tilde{\boldsymbol{w}}_1^T, \tilde{\boldsymbol{w}}_2^T ..., \tilde{\boldsymbol{w}}_{nr}^T]^T$ is the noise vector of MIMO-OTFS systems.

Assuming $n_t = n_r = n_a$ (the number of transmit and receive antennas is equal), and considering that the matrix $\boldsymbol{H}$ is also sparse, we can represent equation (4.37) using a factor graph with MNn_a variables nodes and MNn_a factor nodes, similar to the SISO case. The number of non-zero elements in each line and column of $\boldsymbol{H}_{mimo}$ is equal to the number of paths P times n_a.

Extending the study to MIMO-OTFS systems implies a substantial increase in the complexity of the algorithms described in this chapter. This increase is mainly attributed to MPA, which considers each edge between variable nodes and factor nodes, with the complexity growing with the number of paths. Additionally, in a multipath scenario, each antenna in the MIMO system configuration will experience fading from each path.

In the next section, we will analyze the complexity of the considered algorithms for MIMO-OTFS systems by counting the required number of floating-point operations (FLOPs).

Once again, a preprocessing step is required for all message passing algorithms to compute the square norms $|h_{j,l}|^2$, which demands $3POA^2$ FLOPs. Table 4 displays the number of total FLOPs per iteration for each algorithm as a function of the constellation size (Z-QAM modulation), the number of paths P, the number of variable nodes (VNs) and factor nodes (FNs) (O).

Table 5 – Complexity by total number of FLOPs per iteration to MIMO-OTFS

Algorithm	**FLOPs**
MPA	$[(Z^{PA-1})(PA-1)+PA+12]ZPOA^2-15ZOA$
FG-GAI	$[6Z^2+(15PA-5)Z+(2Z+2)PA-5]POA^2$
AMP-GA	$(15Z+22PA-19)POA$
AMP-EP	$(7Z+16PA)OA+(10PA+11)POA^2$
AMP-FO	$(15Z+24PA+8)OA+3POA$

Source: the author.

Based on Table 5, Figure 17 illustrates the complexity in terms of FLOPs as a function of the constellation size Z for each algorithm.

Figure 17 – Complexity Evaluation to MIMO-OTFS

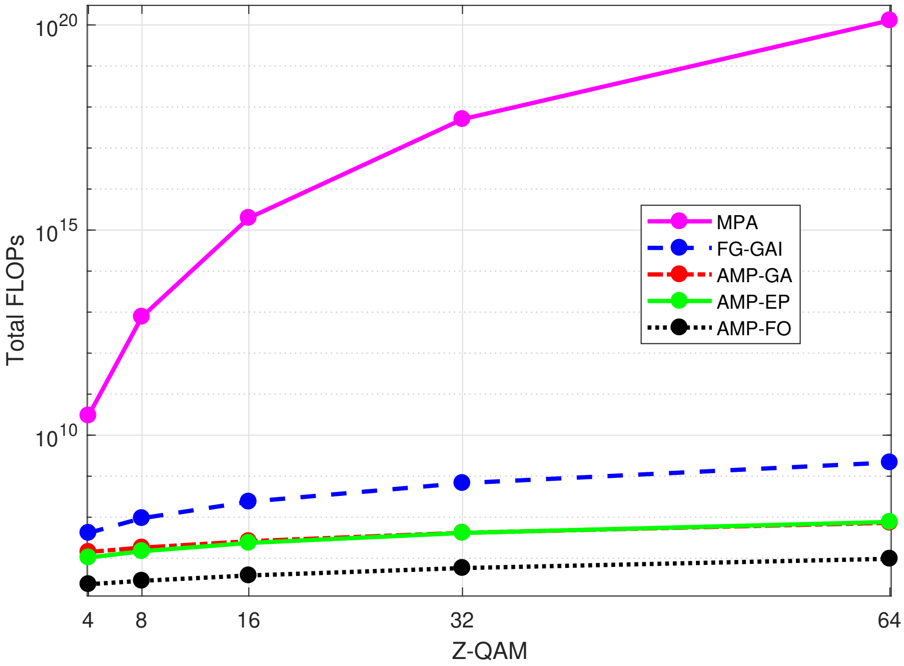

Source: the author.

In Figure 17, we have maintained the same configuration as described in subsection 4.6, which involved a single antenna (SISO-OTFS). However, in this context, we extend our analysis to include two antennas $A = 2$. We will employ the identical set of parameters to assess the bit error rate performance in our study of MIMO-OTFS systems. It is evident that there has been an exponential increase in the complexity of the MPA algorithm due to the need to consider each path P for each antenna in the MIMO-OTFS system.

4.8 Results and discussion

In this section, we will evaluate the bit error rate (BER) performance of the OTFS system, considering the various low-complexity algorithms presented in this chapter (MPA, FG-GAI, AMP-GA, AMP-EP, and AMP-FO) over a delay-Doppler channel model in a multipath scenario for both SISO-OTFS and MIMO-OTFS cases.

4.8.1 OTFS in SISO system

The simulation parameters are detailed in Table 6.

Table 6 – Simulation Parameters for SISO-OTFS

Parameter	**Value**
Carrier frequency (f_c)	4 GHz
Subcarrier spacing (Δf)	15 kHz
Number of subcarriers (M)	64
Number of OTFS symbols (N)	64
Number of paths (P)	4
Modulation scheme	4-QAM
UE speed	60, 120, 180 km/h
Channel estimation	ideal
Doppler shift	234 Hz
Delay shift	1 μ s

Source: the author.

The channel model used is the DDP multipath model (RAMACHANDRAN; CHOCKALINGAM, 2018). Based on the parameters given in Table 6, we considered two different integer case ($\tilde{k}_i = 0$) scenarios, both with four paths, where each reflector had delay shift multiple of $1\ \mu s$ and Doppler shifts multiple of 234 Hz. The delay and Doppler shifts for each path in the two considered scenarios are provided in the Table 7 and Table 8, respectively. In Scenario 1, all reflectors have different Doppler shifts but are in the same direction, while in Scenario 2, the reflectors are in different directions (two positive and two negative Doppler shifts).

Table 7 – DDP for multipath channel model - Scenario 1

Path index (i)	1	2	3	4
Delay (τ_i)	0 μ s	1 μ s	2 μ s	3 μ s
Delay tap (l_i)	0	1	2	3
Doppler (ν_i)	0 Hz	234 Hz	468 Hz	702 Hz
Doppler tap (k_i)	0	1	2	3

Source: the author.

Table 8 – DDP for multipath channel model - Scenario 2

Path index (i)	1	2	3	4
Delay (τ_i)	0 μ s	1 μ s	2 μ s	3 μ s
Delay tap (l_i)	0	1	2	3
Doppler (ν_i)	-234 Hz	468 Hz	234 Hz	-234 Hz
Doppler tap (k_i)	-1	2	1	-1

Source: the author.

First, we conducted a study of the BER performance as a function of the number of iterations for each algorithm to determine the most appropriate value for the system. Figure 18 presents the results for Scenario 2 with $SNR = 12\ dB$

Figure 18 – Analysis of number of iterations for Scenario 2

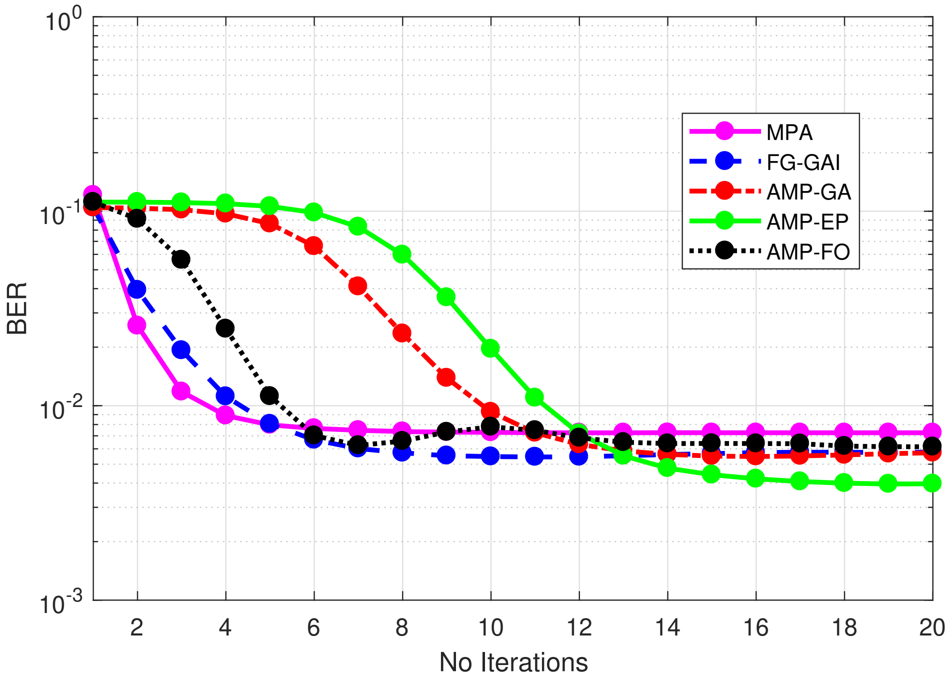

Source: the author.

Based on Figure 18, we can infer that, for the considered DDP model, the required number of iterations for each algorithm is as follows: FG-GAI requires 10 iterations, AMP-GA requires 15 iterations, AMP-EP requires 20 iterations, and AMP-FO requires 15 iterations. MPA converges faster and, therefore, only requires 5 iterations. After determining the appropriate number of iterations, we studied the impact of the damping factor for scenario 2, as Eq. (4.5), on the BER performance in the range of 0.45 to 0.75, as shown in Figure 19.

The influence of the damping factor is minimal, with each algorithm exhibiting different optimal values. FG-GAI performs best at a damping factor of 0.55, AMP-GA at 0.5, AMP-EP at 0.65, and AMP-FO at 0.6. MPA remains unaffected by variations in the damping factor, and the same number of iterations and damping factors have been used for scenario 1. A summary of the damping factors and the number of iterations for each algorithm is presented in 9.

Figure 19 – Analysis of damping factor for Scenario 2

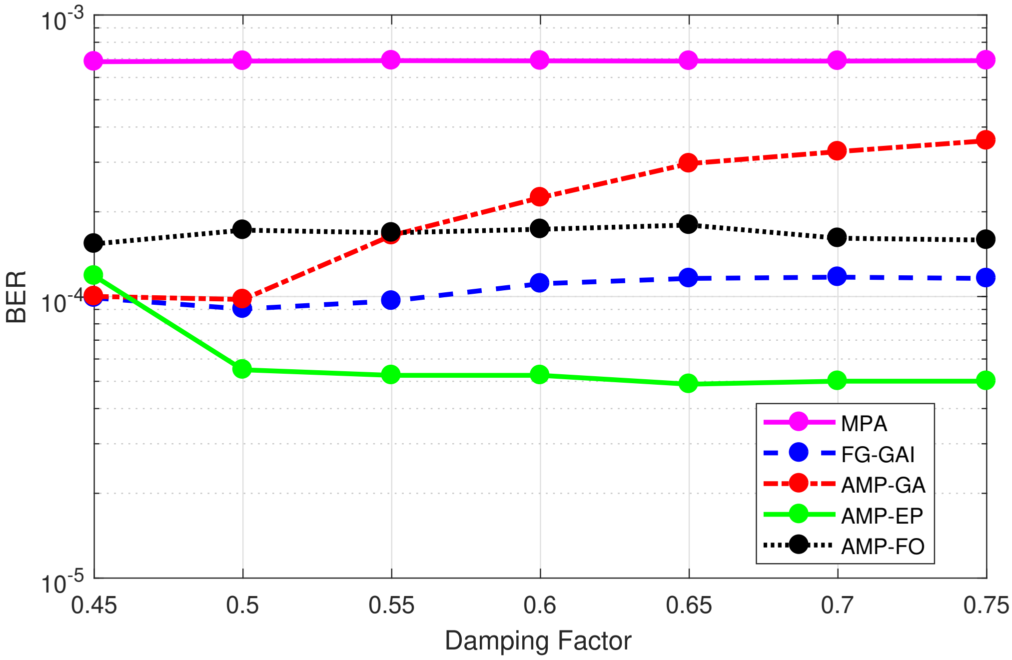

Source: the author.

Table 9 – Damping Factor and Iteration values

Algorithm	Iterations	Damping factor
MPA	5	0.6
FG-GAI	10	0.55
AMP-GA	15	0.5
AMP-EP	20	0.65
AMP-FO	15	0.6

Source: the author.

Using these parameters, we simulated the BER performance of the OTFS system for each low-complexity algorithm detector across a range of SNRs from -13 to 17 dB, for both Scenario 1 and Scenario 2. Figure 20 and Figure 21 depict the BER performance as a function of SNR for Scenario 1 and Scenario 2, respectively.

These simulations used the channel model defined by Eq. (2.9), and all graphs are based on the same $\boldsymbol{H}_{eff}$ matrix.

In both Figures 20 and 21, all algorithms perform similarly at low SNRs. However, differences become apparent above 12 dB. In Scenario 1, the MPA algorithm, despite being the most complex, achieves the best BER performance. At BER$= 10^{-3}$, the performance losses of AMP-EP and AMP-FO are 1.25 dB and 2.25 dB, respectively, compared to MPA. In Scenario 2, AMP-EP achieves the same performance as MPA,

Figure 20 – BER Performance of OTFS with Scenario 1

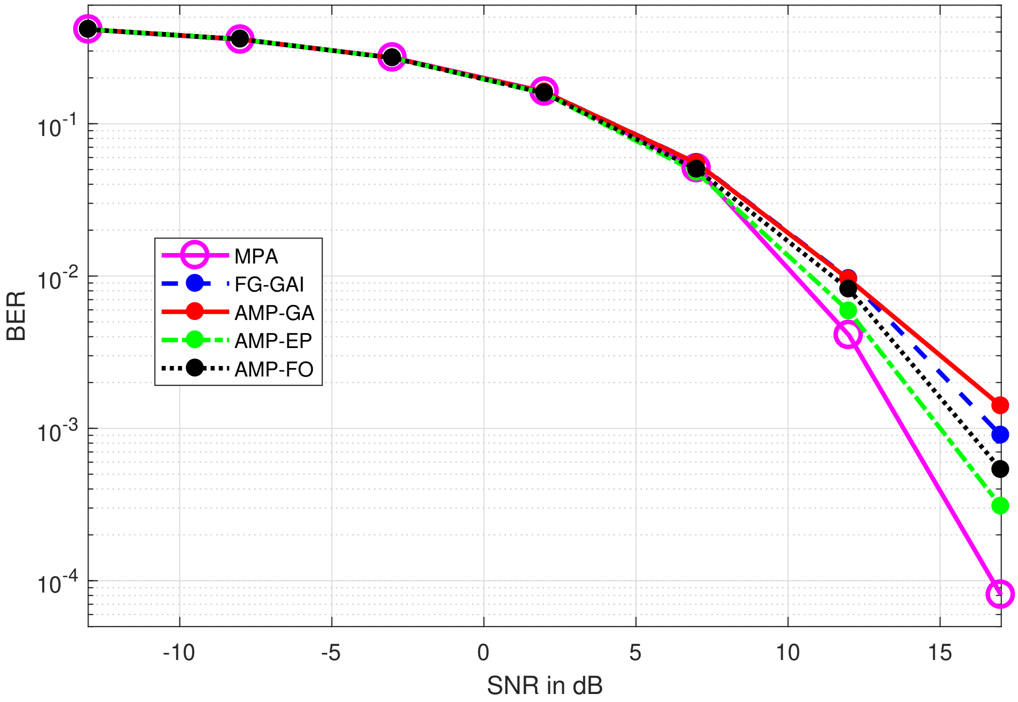

Source: the author.

Figure 21 – BER Performance of OTFS with Scenario 2

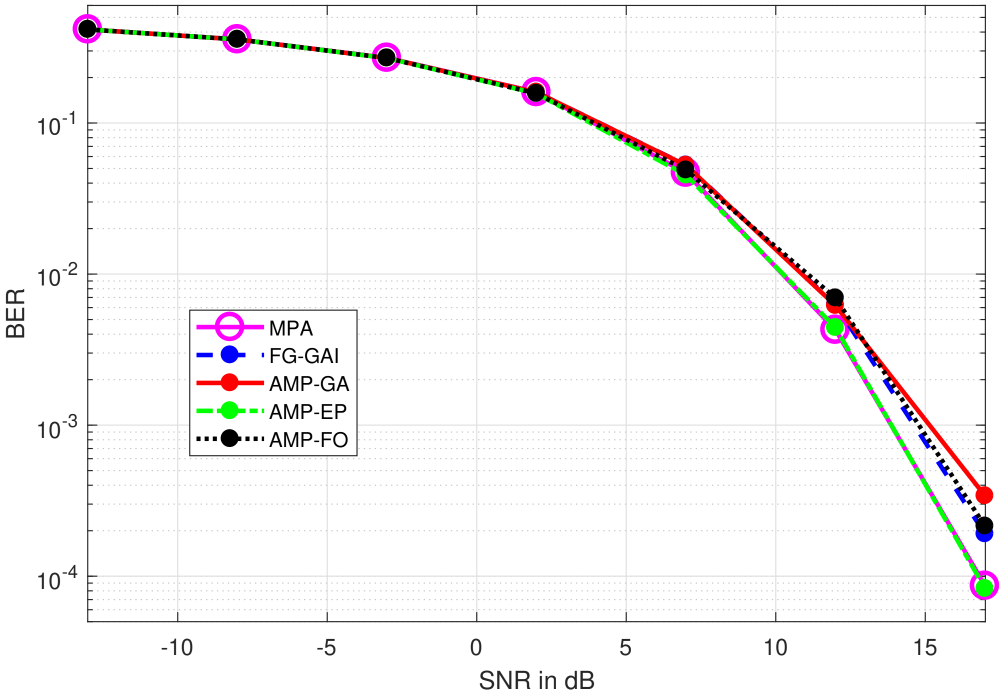

Source: the author.

while AMP-FO's performance is 0.8 dB worse at BER$= 10^{-3}$. In both scenarios, AMP-GA has the worst performance, followed by FG-GAI and AMP-FO.

In both scenarios, the BER performance of the AMP-FO algorithm closely resembles that of AMP-EP, while AMP-FO is significantly less complex. These results suggest that, in both scenarios, AMP-FO strikes a favorable balance between complexity and BER performance.

It is worth noting that in this thesis, another approach was explored for this scenario, based on a new data organization model in the received signal to enhance data detection in a continuous variable environment in the context of the quantification of uncertainties (CURSI; SAMPAIO, 2015). Appendix B presents the method and preliminary result obtained from this approach, which showed promising results, as it reduces the complexity-BER trade-off since matrix inversion is not required.

4.8.2 OTFS in MIMO system

The BER performance of the MIMO-OTFS system was evaluated over a delay-Doppler channel model in a multipath scenario, considering the low-complexity algorithms AMP-GA, AMP-EP, and AMP-FO. Their performance was compared to that of the linear Minimum Mean Square Error (MMSE) algorithm. MMSE provides a direct evaluation of the transmitted symbols using Eq. (2.19), where $\boldsymbol{H} = \boldsymbol{H}_{mimo}$ and $\boldsymbol{y} = \boldsymbol{y}_{mimo}$.

The simulation parameters are detailed in Table 10.

Table 10 – Simulation Parameters for MIMO-OTFS

Parameter	**Value**
Carrier frequency (f_c)	4 GHz
Subcarrier spacing (Δf)	15 kHz
Number of subcarriers (M)	64
Number of OTFS symbols (N)	64
Number of paths (P)	4
Number of antennas (n_a)	2
Modulation scheme	4-QAM
UE speed	60, 120 km/h
Channel estimation	ideal
Doppler shift	234 Hz
Delay shift	1 μ s

Source: the author.

The channel model used is the same delay-Doppler Profile multipath model

(RAMACHANDRAN; CHOCKALINGAM, 2018), and the delay and Doppler shifts for each path were taken from Table 10 for the more complex Scenario 2. We simulated the BER performance of the MIMO-OTFS system for each low-complexity algorithm detector across a range of SNRs from -5 to 10 dB. Figure 21 presents the BER performance as a function of SNR.

Figure 22 – BER Performance of MIMO-OTFS

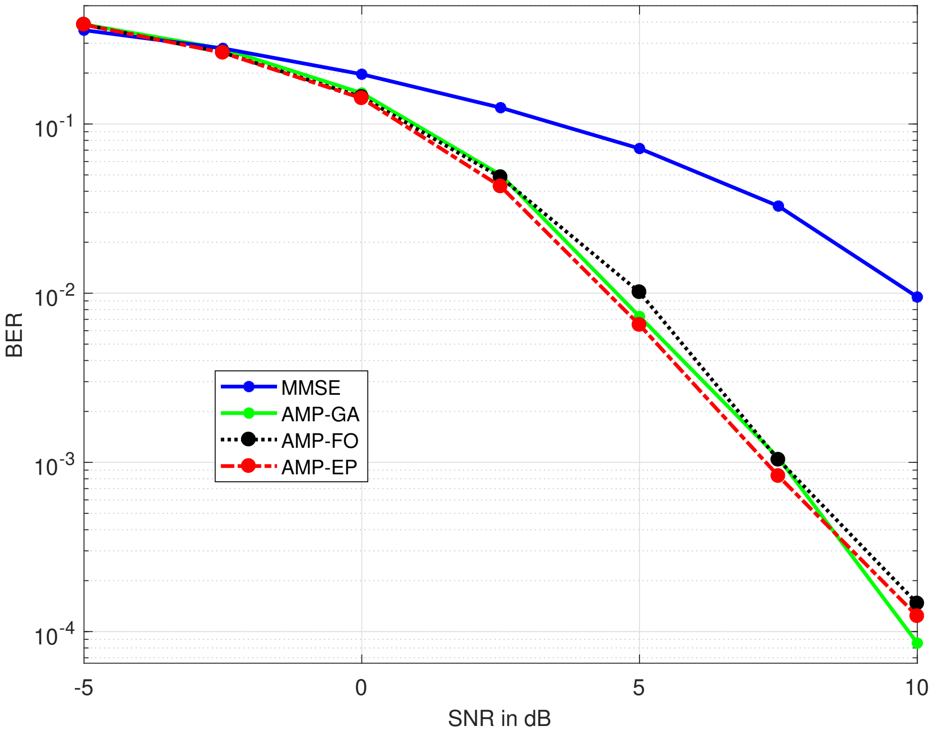

Source: the author.

All factor graphs are based on $\boldsymbol{H}_{mimo}$ matrix, which represents the MIMO effective channel matrix. As shown in Figure 22, all low-complexity MPA algorithms (AMP-GA, AMP-EP, and AMP-FO) exhibit similar performances, while the linear algorithm MMSE provides lower performance. A 5 dB difference at BER $= 10^{-2}$ is observed between MMSE and AMP algorithms. The BER performance of the AMP-FO algorithm closely resembles that of AMP-GA and AMP-EP, but AMP-FO is significantly less complex.

As expected, the MIMO-OTFS scheme outperforms the SISO-OTFS, with a 5 dB gain observed at BER $= 10^{-1}$. Due to spatial diversity, the detector algorithms exhibited similar performance behavior, with some divergence at 10 dB. The most complex AMP-GA interactive algorithm achieved the best BER performance, while the linear algorithm MMSE provided the worst BER performance. Furthermore, the complexity of the AMP-FO algorithm is significantly lower than that of the other interactive algorithms AMP-GA and AMP-EP. Therefore, AMP-FO presents the best performance-complexity tradeoff, similar to the SISO-OTFS case.

5 CHANNEL ESTIMATION

The wireless communication channel is susceptible to signal degradation caused by multipath effects. These effects result from electromagnetic wave reflections at various points along the transmission path between the digital transmitter and receiver. This multiplicity of propagation paths, referred to as multipath, can introduce interference when multiple signals reach the receiver simultaneously, degrading the quality of the received signal. One of the consequences of this interference is ISI, where digital modulation symbols overlap, leading to errors in symbol detection. In the context of wireless communication, accurate estimation and compensation of channel effects play a crucial role in the receiver's performance. The increasing demand for communication systems with higher data transmission capacities, robustness, and lower computational complexity has driven extensive research into algorithms for channel estimation and symbol detection. The OFDM transmission technique has gained prominence due to its resistance to ISI and ability to transmit high data rates. OFDM achieves this by dividing the total available bandwidth into smaller subchannels and using orthogonal subcarriers for data transmission. However, even in OFDM systems, channel estimation remains essential due to the impact of multipath wireless channels.

Additionally, OFDM is less robust when operating in rapidly time-varying multipath scenarios. In response to this challenge, researchers have recently proposed the use of OTFS (Orthogonal Time Frequency Space) modulation, particularly in scenarios with high Doppler shifts. OTFS differs from OFDM in that it multiplexes symbols in a delay-Doppler domain rather than the time-frequency domain used by OFDM, which is prevalent in current systems such as 4G and 5G networks. Studies indicate several advantages of OTFS over OFDM, including increased data rates and reduced Peak-to-Average Power Ratio (PAPR). Another significant advantage is the sparsity of the channel produced by OTFS, allowing the use of low-complexity algorithms for data detection. Nevertheless, in both OFDM and OTFS, accurate channel estimation remains crucial to minimize errors in data detection. This thesis addresses the challenge of channel estimation in the context of OTFS modulation applied to macrocell channels.

In this chapter, we will begin by reviewing the fundamentals of time-domain channel estimation using OTFS modulation in a macrocell channel. To obtain the CIR, we need to interpolate the estimated samples received at the receiver. While a previous work (DAS *et al.*, 2020) used the cubic spline method for interpolation, described in Section 5.2.1, this thesis proposes an alternative interpolation method based on solving the Poisson equation through Finite Element Method (FEM), presented in Section 5.2.2. This method offers several advantages, including the calculation of source values for the equation within each sample subinterval through an ODE of 2nd order and taking into account the signal's nature. Finally, in Section 5.3, we will present the results of a comparison between the different methods.

5.1 Time Frequency Domain Channel Estimation

In this section, we will summarize the steps involved in estimating the macrocell channel, as described in (DAS *et al.*, 2020). This process generates estimated samples of the reference CIR to obtain the complete CIR through interpolation. Estimating the CIR of a macrocell channel is particularly challenging due to the presence of fractional Doppler effects. The samples of Doppler frequencies associated with the Tap Delay Line (TDL) values of the channel may not align exactly with the grid points Γ, as defined in (3.2). To address this, we utilize the more complex overlay version of OTFS, which avoids Intersymbol Interference (ISI). Our studies indicate that this results in values distributed across N points in the impulse response for each sampled tap delay of the received signal.

Considering that $\tilde{l}_i$ denotes the fractional delay and $\tilde{k}_i$ denotes the fractional Doppler shift. For the macrocell scenario, where we set $M = 600$ e $N = 12$ (representing 600 multicarriers spaced $15\ kHz$ apart, with a fixed number of 12 OFDM symbols per frame). , the interference caused by fractional delay is considered insignificant due to satisfactory delay resolution $(1/M\Delta f)$. However, the fractional Doppler shift remains relevant, considering the low resolution $1/NT$ compared to the Doppler value associated with the speed of reflectors (e.g., $576\ km/h$). In this case, we consider T, taking into account the duration of the Cyclic Prefix (CP), as $T = T_u + T_L$, where $T = 1/\Delta f + T_L$, resulting in $T\Delta f = 1 + \Delta f T_L = 1 + L/M$.

Our goal is to estimate the impulse response of the macrocell channel in the time domain rather than the delay-Doppler domain. According to (DAS *et al.*, 2020), channel estimation in the time domain exploits the sparsity in this domain and reduces the complexity of channel impulse response estimation in the presence of fractional

Doppler. From this motivation, a method for estimating the time domain equivalent channel matrix that uses energy thresholding and spline interpolation was presented in (DAS *et al.*, 2020), with Linear Minimum Mean Square Error (LMMSE) used for detection.

Rather than employing the embedded pilot scheme proposed in (RAVITEJA *et al.*, 2019), , which involves a single high-SNR pilot surrounded by a guard band within the delay-Doppler grid, we adopt a different approach. We utilize a single high-SNR pilot while distributing the guard band across all k points, where $k \in \{0, 1, ..., N-1\}$. This modification addresses the interference caused by fractional Doppler effects affecting all symbols within the Doppler domain. In this context:

$$X[l,k] = \begin{cases} \sqrt{P_{PLT}} & if \;\; l = l_p \;\; k = k_p; \\ 0 & if \;\; lp - l_\tau < l < lp + l_\tau \\ \text{QAM-4 symbol} & else \end{cases} \tag{5.1}$$

where $\sqrt{P_{PLT}}$ represents a pilot energy, l_p signifies the pilot's delay position, k_p denotes the pilot's Doppler position, and l_τ represents the maximum delay considered.

To illustrate this pilot distribution, Figure 23 provides a 2D representation of symbol placement within the delay-Doppler domain:

Figure 23 – Example of symbol placement in the delay-Doppler domain with the embedded pilot at (l_p, k_p) and the guard interval.

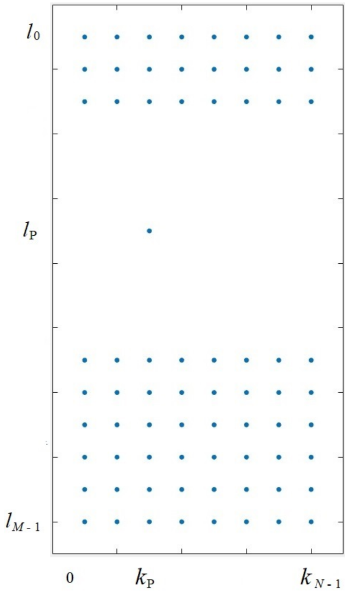

Source: the author.

Subsequently, starting with the data in the delay-Doppler domain at the transmitter, we execute the Orthogonal Time Frequency Space (OTFS) transform. This transformation entails the Inverse Short-Time Fourier Transform (ISFFT) to convert data from the delay-Doppler domain ($X[l,k]$) into the time-frequency domain $X^{FT}[m,n]$. The process involves the following steps: Firstly, we apply an Inverse Fast Fourier Transform (IFFT) in the Doppler domain to obtain $X'[l,n]$, delay-time domain.

$$X'[l,n] = \frac{1}{\sqrt{N}} \sum_{k=0}^{N-1} X[l,k] e^{j2\pi\frac{nk}{N}}. \tag{5.2}$$

Then, we apply an FFT in the delay domain to obtain $X^{FT}[m,n]$,

$$\begin{aligned} X^{FT}[m,n] &= \frac{1}{\sqrt{M}} \sum_{l=0}^{M-1} X'[l,n] e^{-j2\pi\frac{ml}{M}} \\ &= \frac{1}{\sqrt{MN}} \sum_{k=0}^{N-1} \sum_{l=0}^{M-1} X[l,k] e^{j2\pi\left(\frac{nk}{N}-\frac{ml}{M}\right)}. \end{aligned} \tag{5.3}$$

Subsequently, we employ an OFDM modulator, executed via an IFFT in the frequency domain, to yield the signal in the time domain, as shown in Eq. (5.8).

$$X''[l,n] = \frac{1}{\sqrt{M}} \sum_{m=0}^{M-1} X^{FT}[m,n] e^{j2\pi\frac{ml}{M}}. \tag{5.4}$$

Hence, this IFFT compensates for the FFT applied in the delay domain to $X'[l,n]$, as a consequence of signal processing, as described in Eq. (5.5)

$$X''[l,n] = X'[l,n] = \frac{1}{\sqrt{N}} \sum_{k=0}^{N-1} X[l,k] e^{j2\pi\frac{nk}{N}}. \tag{5.5}$$

Consider a scenario where we transmit a frame containing only one non-zero element, the pilot element P_{PLT}. In this case:

$$X[l,k] = \begin{cases} \sqrt{P_{PLT}} & if \;\; l = l_p \;\; k = k_p; \\ 0 & else \end{cases} \tag{5.6}$$

Then we have:

$$\begin{aligned} X''[l,n] &= \frac{1}{\sqrt{N}} \sqrt{P_{PLT}} \sum_{k=0}^{N-1} \delta(l-l_p)\delta(k-k_p) e^{j2\pi\frac{nk}{N}} \\ X''[l,n] &= \begin{cases} \frac{1}{\sqrt{N}} \sqrt{P_{PLT}} \; e^{j2\pi\frac{nk_p}{N}} & if \;\; l = l_p; \\ 0 & else \end{cases} \end{aligned} \tag{5.7}$$

This implies that the pilot symbol will experience scattering across the N points within the time domain. This scattering behavior forms the foundation for collecting pilot samples from the impulse response of the channel, ultimately leading to the estimation of channel coefficients.

Given that we are utilizing CP-OTFS modulation to mitigate ISI, a CP of length L is added to the beginning of each block of N symbols for each M subcarrier from the output of the OFDM modulator. The total duration T must account for the symbol duration T_u and the CP duration T_L, calculated as $T = T_u + T_L$. Following this procedure, the time-domain output signal $s(t)$ after the OFDM modulator is expressed as:

$$s(t) = \sum_{m=0}^{M-1} \sum_{n=0}^{N-1} X^{FT}[m,n]\; e^{j2\pi m\Delta f(t-nT_u)}\; g_{tx}(t-nT_u) \tag{5.8}$$

This signal, referred to as $s_{cp}(t)$, is the signal transmitted in the time domain.

$$s_{cp}(t) = \frac{1}{\sqrt{M}} \sum_{m=0}^{M-1} \sum_{n=0}^{N-1} X^{FT}[m,n]\; e^{j2\pi m\Delta f(t-nT)}\; g_{tx}(t-nT). \tag{5.9}$$

To convert $s_{cp}(t)$ into the delay-time domain, we incorporate a CP with a length $L = \lceil T_{cp}B \rceil$, where $B = M\Delta f$, resulting in $X''_{cp}[l', n]$, with $l' \in \{0, 1, ..., M+L-1\}$:

$$X''_{cp}[l', n] = \frac{1}{\sqrt{N}} \sum_{k=0}^{N-1} x[l', k]\; e^{j2\pi \frac{nk}{N}}. \tag{5.10}$$

Suppose we assume the transmission of a single non-zero element, the 2D impulse pilot located at position $x(l_p, k_p)$ with a value of $\sqrt{P_{PLT}}$:

$$X^{FT}[m,n] = \frac{1}{\sqrt{MN}} \sqrt{P_{PLT}}\; e^{j2\pi\left(\frac{nk_p}{N} - \frac{ml_p}{M}\right)}. \tag{5.11}$$

In this scenario:

$$s_{cp}(t) = \frac{1}{\sqrt{M}} \sum_{m=0}^{M-1} \sum_{n=0}^{N-1} \frac{1}{\sqrt{MN}} \sqrt{P_{PLT}}\; e^{j2\pi\left(\frac{nk_p}{N} - \frac{ml_p}{M}\right)}\; e^{j2\pi m\Delta f(t-nT)} g_{tx}(t-nT). \tag{5.12}$$

In essence, the initial spread impulse pilot results from the time delay proportional to l_p added to the time of T_{cp}, after which we only have the pilot impulse recurring every T. Consequently, scattering occurs throughout every considered symbol time, reflecting a dispersion across the entire time domain but confined to the pilot's delay location. This dispersion manifests as a scattering in the delay domain, contingent on l_p. To visualize this behavior more clearly, consider $s_{cp}(t)$ in the delay-time domain, $X''_{cp}[l', n]$, where the pilot positions across all N points are given by: $l' = l_p + L + (M+L)n$, as shown in Eq. (5.13):

$$X''_{cp}[l_p + L + (M+L)n, n] = \frac{1}{\sqrt{N}} \sum_{k=0}^{N-1} \sqrt{P_{PLT}}\; e^{j2\pi \frac{nk}{N}}. \tag{5.13}$$

Figure 24 exemplifies the behavior of the 2D pilot transmitted by $s_{cp}(t)$ considering samples in the delay-time domain.

Figure 24 – Transmitted signal $X''_{cp}[l', n]$ with pilot samples in the delay-time domain

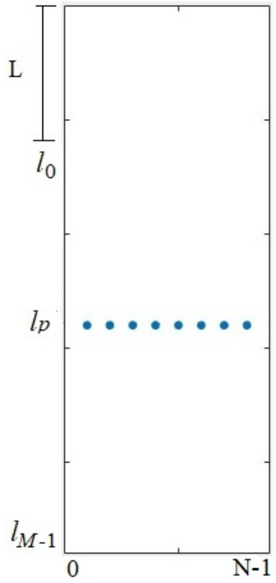

Source: the author.

For a baseband time-varying channel, it is imperative to consider the maximum delay (τ_{max}) and Doppler (ν_{max}) spread to express the channel delay length $l_\tau = \lceil \tau_{max} M \Delta f \rceil$ and channel Doppler length $k_\nu = \lceil \nu_{max} N T \rceil$, respectively. The CP length ($L = \lceil T_L B \rceil$) must exceed or equal the maximum delay to enable the detection of channel taps by observing the shifts experienced by the pilot symbol due to macrocell channel interference from the received signal $r_{cp}(t)$. Consequently, factoring in the transmitted signal $s_{cp}(t)$, channel impulse response $h(\tau, \nu)$, and g_{tx} (a rectangular pulse), the processing of the time-domain received signal on the baseband is described by:

$$r_{cp}(t) = \int_{\tau=0}^{\tau_{max}} \int_{\nu=-\nu_{max}}^{\nu_{max}} h(\tau,\nu) s_{cp}(t-\tau)\; e^{j2\pi\nu(t-\tau)} d\tau d\nu + w(t), \tag{5.14}$$

In the case of the macrocell channel, where the gain paths of each tap vary smoothly over time, this variation directly influences the Doppler domain, as outlined in Eq. (2.9) for a time-varying channel such as the macrocell channel. Utilizing Eq. (2.10), the signal received in (5.14) can be reformulated as:

$$r_{cp}(t) = \int_{\tau=0}^{\tau_{max}} h(\tau,t) s_{cp}(t-\tau) d\tau + w(t), \tag{5.15}$$

In the context of discrete paths and assuming negligible noise due to a high SNR, we can simplify Eq. (5.15) as follows:

$$r_{cp}(t) = \sum_{i=1}^{P} h_i(\tau_i, t)\; s_{cp}(t-\tau_i)\; e^{j2\pi\nu_i(t-\tau_i)}, \tag{5.16}$$

Thus, as discussed in (DAS *et al.*, 2020), , by sampling the received signal (5.16) at a rate of $fs = (M+L)/T$, we obtain $r_{cp}[a']$,

$$r_{cp}[a'] = \sum_{i=1}^{P} h_i[l_i, a']\; x_{cp}[a'-l_i]\; e^{j2\pi \frac{k_i(a'-l_i)}{(M+L)N}}, \tag{5.17}$$

where $a' \in \{0, 1, ..., (M+L)N-1\}$. These samples collected from $r_{cp}[a']$ correspond to observations of the pilot's delay position (l_p), which was transmitted with a high SNR (e.g., $30dB$). To achieve this, a threshold method is employed. This method retains only those samples exceeding a positive detection threshold, ranging from the pilot's delay position to the maximum delay ($l_\tau \leq L-1$) considered for all N points in the time domain. A detailed description of the threshold method, based on (RAVITEJA *et al.*, 2019), is available in Appendix C, providing a matrix analysis of the received signal in the delay-Doppler domain for enhanced clarity. In this thesis, we adopt the same threshold value Υ as the original authors, i.e., $\Upsilon = 3\sigma_d^2$, where σ_d^2 represents the variance of the transmitted signal.

As evident from Eq.(5.7), the transmitted 2D impulse pilot scatters across N time points. Consequently, after passing through the channel, each tap will spread the pilot across n time points. However, the spread in the delay domain is limited to $l_p + l_\tau$ from the l_p position. Thus, for each delay position l_i relative to l_p, where the received sample exceeds the threshold, we normalize this sample by the gain path associated with the respective scattered samples of the transmitted pilot signal. This process yields the coefficients of the channel spread at n points. Subsequently, we calculate $l_i = l - l_p$ to determine the first delay position of each path. The sample at each of these positions is then normalized by the respective position of the pilot transmitted in $X''_{cp}[l', n]$. By performing these steps, we obtain the taps of the estimated channel. A cubic spline interpolation within the range $[0 \;\; (M + L)N - 1]$ is applied to these samples, denoted as $\hat{\boldsymbol{h}}_{l_i} = r_{cp}[a']/x''_{cp}[a']$. Consequently, considering all samples a' above the threshold ($r_{cp}[a'] > \Upsilon$) as pilot samples, we obtain the vector of variations in estimated path gains in the time domain of the estimated channel. This can be expressed as:

$$\begin{aligned} \hat{\boldsymbol{h}}_{l_i} =& spline(\{\hat{h}(l_i + l_p + L + a', a' \; |a' \in [0 \;\; (M + L)N - 1]\}, \\ & [L + l_p + l_i : M + L : (M + L)N], [0 : (M + L)N - 1]). \end{aligned} \tag{5.18}$$

where "spline" refers to the Matlab function "interp1" for cubic spline interpolation. It takes three input vectors: the first indicates the sample points, the second contains the values of the sample coefficients, and the third defines the desired interpolation interval. Using these estimated values, we obtain the Channel Impulse Response (CIR) of the estimated channel, denoted as $\hat{\boldsymbol{H}}$ following Eq. (3.11). In this case, we consider $h_i \boldsymbol{\Delta}_{l_i} = diag[\hat{\boldsymbol{h}}_{l_i}]$ as the diagonal matrix of coefficients for each path, resulting in $\hat{\boldsymbol{H}} \in \mathbb{C}^{(M+L)N \times (M+L)N}$, representing the estimated channel matrix in the time domain.

After eliminating the CP samples, we can apply the same procedure as described in (3.17) to obtain $\hat{\boldsymbol{H}}_{eff}$. This enables the processing of data detection based on the estimated effective channel. For data detection, we also remove the CP samples from $r[a']$ to obtain $r[n']$, where $n' = 0, ..., N - 1)$. Subsequently, the time-frequency data is obtained as:

$$Y^{FT}[m', n'] = \frac{1}{\sqrt{M}} \sum_{m=0}^{M-1} r[n'] e^{-j2\pi \frac{m'm}{M}}, \tag{5.19}$$

Following this, the delay-Doppler signal is acquired by applying the OTFS inverse transform (SFFT) as presented in equation Eq. (5.19).

$$Y[l',k'] = \frac{1}{\sqrt{MN}} \sum_{m'=0}^{M-1} \sum_{n'=0}^{N-1} Y^{FT}[m',n'] e^{-j2\pi(\frac{n'k'}{N} - \frac{m'l'}{M})}, \tag{5.20}$$

5.2 Channel estimation by interpolation

As previously mentioned, channel estimation involves applying the threshold method to the pilot scatter position samples and estimating these samples based on high SNR pilot samples used during transmission. This results in N samples for each tap, which collectively constitute the CIR. Consequently, the problem at hand can be addressed through interpolation techniques applied to each pair of estimated samples derived from the received signal.

In our channel estimation approach, we have employed a supervised method. However, it is important to note that the CIR of the macrocell channel involves complex values. Consequently, we need to interpolate both the real and imaginary parts of each data point over time, bridging the gaps between the collected samples.

The interpolation technique initially chosen by the authors in (DAS *et al.*, 2020) is the cubic spline method. We will provide a concise summary of this method in Section 5.2.1. . Additionally, we will introduce another interpolation method for CIR estimation, one that utilizes a numerical solution of the Poisson equation. In Section 5.2.2.2, we will elaborate on our approach, which employs the FEM for this purpose. Given that the estimated samples are in the form of complex symbols, we perform the interpolation of the real part $\{Re\}$ independently from the imaginary part $\{Im\}$. This separation allows us to concatenate these two parts to obtain the complete complex value: $\{Re\}+j\{Im\}$, as suggested in (BROWN; CHURCHILL, 2009). For those readers unfamiliar with these methods of estimating complex variables, we recommend referring to(BARTELS *et al.*, 1998), (JOHNSON, 1988) and (PINA, 2010), where the authors delve into the intricacies of working with complex variables. The Sections 5.2.1 and 5.2.2 support the estimation of complex variables through the spline and FEM methods, respectively.

5.2.1 Estimation by cubic spline method

Instead of attempting to model a set of observations with a single polynomial, this method selects distinct points within the range of observations, often referred to as "knots," and defines a separate polynomial for each segment. This approach is particularly valuable when dealing with complex curves, as it enables the modeling of intricate shapes by employing simpler polynomial functions. In essence, the principle behind spline interpolation is that, if a function possesses a certain degree of smoothness, typically indicated by having at least a continuous derivative, the piecewise interpolating polynomial can effectively approximate the observed function. This holds true even when the individual polynomial segments themselves are not inherently smooth (BARTELS *et al.*, 1998).

In this context, given a set of N points $\mathcal{J} = (x_j, y_j)_{j=1}^{n}$ such that $x_{j+1} > x_j$ and abscissa values arranged in ascending order, a cubic spline $\mathcal{P}_3$ can interpolate these points. A cubic spline is a piecewise function consisting of third-degree polynomials within each subinterval $[x_{k-1}, x_k]$. This spline ensures continuous first and second-order derivatives within the interval $[x_0, x_n]$. Specifically, each subinterval features piecewise cubic polynomials:

$$p_k(x) = a_k(x - x_k)^3 + b_k(x - x_k)^2 + c_k(x - x_k) + d_k \tag{5.21}$$

A cubic spline is determined by $4n$ parameters: $a_1, b_1, c_1, d_1, a_2, b_2, c_2, d_2, ..., a_n,$ b_n, c_n, d_n. To maintain continuity of $\mathcal{P}_3$, $\mathcal{P}_3^{'}$ and $\mathcal{P}_3^{''}$, we must ensure: $p_k(x_k) = p_{k+1}(x_k)$, $p_k^{'}(x_k) = p_{k+1}^{'}(x_k)$, and $p_k^{''}(x_k) = p_{k+1}^{''}(x_k)$, for all $k = 0, 1, ..., n-1$.

In an interpolation problem, we also have $\mathcal{P}_3(x_k) = y_k$, meaning $p_0(x_0) = y_0$ and $p_k(x_k) = y_k, \forall k = 1, ..., n$. With this, we obtain: $3(n-1) + (n+1) = 4n-2$ equations to determine $4n$ variables. Consequently, two additional open conditions need to be imposed, typically resulting in a choice of natural cubic splines to minimize curvature. Often, the conditions $\mathcal{P}_3^{''}(x_0) = 0$ and $\mathcal{P}_3^{''}(x_n) = 0$ are employed. By manipulating these equations, we find that the parameters $a_1, b_1, c_1, d_1, a_2, ..., d_n$ of a natural cubic spline are determined by solving a classic system of linear equations to find k values of the third-degree polynomial for each of the $n-1$ subintervals.

Thus, it is an interpolation model with good flexibility, enabling the representation of atypical data behaviors that would be unattainable with a singular function or model. The number and placement of nodes play a pivotal role in ensuring the accuracy of the adjustment (SCHUMAKER, 2007). On the flip side, it presents a drawback in the form of potential overfitting. This drawback can detrimentally impact the model's predictive capacity, as an excessive number of nodes can lead to a deterioration in model fit and pose challenges in determining the optimal number and location of these nodes. In essence, it serves as a fundamental interpolation method, regardless of the underlying behavior of the signal.

5.2.2 Estimation by the Finite Element Method (FEM)

It is essential to note that both cubic spline and FEM interpolation methods deal with the estimation of complex CIR values. As per (BROWN; CHURCHILL, 2009), we independently estimate the real $\{Re\}$ and imaginary $\{Im\}$ parts before combining them into a complex variable $\{Re\} + j\{Im\}$. For a deeper understanding of complex variable estimation, please refer to Appendix D.

Considering that the Cauchy-Riemann conditions, outlined in Appendix D, are not met for the channel impulse response of the macrocell channel, we propose a unique behavior for the CIR through the Poisson equation. Our method involves solving the Poisson equation within each of the $N-1$ sampled and estimated subintervals of the channel for each tap. We achieve this by applying the FEM method for interpolation. FEM is chosen due to its stability and accuracy, which are supported by mathematical theories, making it a robust tool for various fields of science and engineering (JOHNSON, 1988).

5.2.2.1 Finite elements method

FEM is a numerical technique applicable to a broad spectrum of problems encompassing diverse physical phenomena subject to various interactions with their surroundings. Its stability and accuracy are well-established and supported by rigorous mathematical theories, enhancing its applicability in science and engineering. FEM is primarily used to solve boundary-value problems based on a differential equation and a set of boundary conditions. (SOLíN, 2005).

The fundamental concept of FEM involves partitioning the domain into smaller subdomains, referred to as finite elements. The unknown quantity's distribution within an element is interpolated based on values at its nodes. Typically, two widely used topologies in FEM are nodal, where scalar unknowns are calculated at element nodes, and edge formulation, where vectorial unknowns are calculated along element edges. The interpolation functions (shape functions) are selected to be a complete set of polynomials. The accuracy of the FEM depends on factors such as the order of these polynomials, among others. Two common approaches include linear and quadratic interpolations; in this context, we use linear interpolation for simplicity. The numerical solution corresponds to the values of the unknown quantity at the nodes of the discretized domain. These values are then determined by solving a classical system of equations, typically represented as $\boldsymbol{Ax} = \boldsymbol{b}$. The construction of this equation system involves converting the governing differential equations and boundary conditions into an integro-differential formulation. This is achieved by minimizing a functional (KOSHIBA, 1993), which is expressed as an integral function with functions as arguments.

This functional can be constructed based on either the variational or weighted-residual method, with the Galerkin method being the chosen approach for this study. In this formulation, the method is applied to a single element, with appropriate weight and interpolation functions employed to derive the corresponding element equations. In the specific context of our one-dimensional problem, which is the primary focus, the equations for each linear element (comprising only 2 nodes) necessitate the determination of both a matrix and a vector for every element (elementary), denoted as $\boldsymbol{A}_e$ and $\boldsymbol{b}_e$, respectively. In the case of a linear element, the interpolation function employed to calculate $\boldsymbol{A}_e$ is expressed as follows:

$$\boldsymbol{A}_e = \frac{1}{l_e}\begin{bmatrix} 1 & -1 \\ -1 & 1 \end{bmatrix} \tag{5.22}$$

$$\boldsymbol{b}_e = \frac{\rho l_e}{2}\begin{bmatrix} 1 \\ 1 \end{bmatrix} \tag{5.23}$$

where l_e signifies the length of the element, which corresponds to the distance between nodes (in our case, l_e is equal one unit), and the elementary vector $\boldsymbol{b}_e$ is computed by considering the element's length, which is distributed across the two nodes, adjusted by a value indicative of the slope of the line. In our specific scenario, this value is determined by the source ρ of the Poisson equation, a topic to be elaborated upon in subsection 5.2.2.2. Specifically, it follows the form of $(\rho l_e)/2$ for each adjacent node. The set of all these individual elements results in the formation of a matrix denoted as $\boldsymbol{A}$ and a global vector designated as $\boldsymbol{b}$. These elements collectively facilitate the derivation of the interpolation solution. This global matrix encompasses the complete spectrum of boundary condition values within the domain under consideration.

The preference for adopting the Galerkin method in this study is rooted in its inherent simplicity when compared to the variational method. Additionally, it commences its approach by starting from the governing differential equation. The initial step in this methodology involves the formulation of a residual derived from the partial differential equation governing the problem at hand. This residual is inherently linked to the boundary values relevant to the problem under analysis. The residual is obtained by transferring all terms of the Partial Differential Equation (PDE) on one side. Subsequently, the residual is subjected to multiplication by a weight function and integrated over the domain of an individual element.

The key steps in applying FEM using Galerkin for solving problems with known boundary conditions in synthetic form are as follows (POLYCARPOU, 2006):

1. Discretize the domain into finite elements;
2. Select appropriate interpolation functions;
3. Formulate the integro-differential equation;
4. Derive the linear equations for each element;
5. Assemble the global matrix system of equations for all elements and solve it using linear algebra techniques. This method is versatile and can be applied to problems of any order, including one-dimensional and two-dimensional cases. The higher the dimensionality of the problem, the more computationally complex it becomes.

In our problem, we need to interpolate $Q = (M + L)N$ values of a function from N estimated samples of the channel impulse response for each multipath. As these values are complex, both the real ($\{Re\}$) and imaginary ($\{Im\}$) components must be interpolated independently. The use of FEM simplifies this process, especially because it is a one-dimensional problem. We use a nodal formulation with linear basis functions in a Cartesian coordinate system. Additionally, observing the smooth and continuous variation over time of each multipath in the channel's impulse response allows us to find a source value in each of the $N-1$ subintervals. This value is essential for solving the Poisson equation, which forms the basis of our interpolation technique using one-dimensional FEM.

5.2.2.2 Poisson equation and FEM

In this section, we address the numerical challenges posed by rapid variations in the macrocell channel. In such cases, the traditional Laplace equation-based formulation does not effectively capture these variations, as it relies on elements optimized for smooth transitions. To overcome this limitation, we introduce a perturbation into this equation by incorporating a source term. This perturbation corresponds to the Poisson equation, which alleviates the need to meet the Cauchy-Riemann conditions, as discussed in Section 5.2.

The Poisson equation is a PDE used to determine physical quantities in various fields, including electromagnetism and engineering. It is named after the French mathematician and physicist Siméon Denis Poisson.

In a general context, the Poisson equation, in conjunction with the specified boundary conditions and constraints, facilitates the determination of values within defined regions.

Before delving into the topic, it is beneficial to provide some context. Figure 25 offers a more detailed insight into our approach. In this figure, the lower section serves as a close-up of the upper view, focusing on a subinterval between φ_n and φ_{n+1}. The upper view, on the other hand, represents $N-1$ subintervals corresponding to time instances derived from estimated samples of the response impulse of the channel. The φ index aligns with time instances within each frame, which are estimated for only a few moments, depending on the chosen symbol number. Our objective is to determine an additional $M+L-1$ values for each subinterval, as depicted in the lower section. This lower part represents one of the $N-1$ subintervals derived from the N samples of a single tap of the estimated macrocell channel impulse response. These estimates originate from the threshold method applied to the received signal. In the application of FEM in one dimension, the topology consists of $(M+L-2)$ interconnected elements, denoted as e interconnected with each other. In our one-dimensional scenario, each element corresponds to the values of the respective abscissas within each $(M+L-1)$ subinterval, as shown in the lower part of Figure 25. The set of these interconnected elements within each subinterval forms a linear FEM mesh, encompassing all the nodes in the considered subinterval. Within this mesh, we aim to estimate values as a function of φ. Consequently, in each subinterval, we have have $(M+L)$ values or nodes available for interpolation using the FEM method. These interpolations originate from a source value (referred to as Poisson's source), calculated using the values of the abscissas $x_1 = (M+L)n+1$ and $x_2 = x_1 + (M+L)$ (corresponding to the abscissa positions of φ_n and φ_{n+1}, respectively, for $n = 1, 2, ..., N$) in conjunction with the respective functions φ_n and φ_{n+1} at each point on the endpoints of each subinterval. Additionally, we take into account the value of $\varphi_n^{'}$, as we will elucidate, by commencing the method from points where the derivative is zero.

Figure 25 – Discretization by subinterval

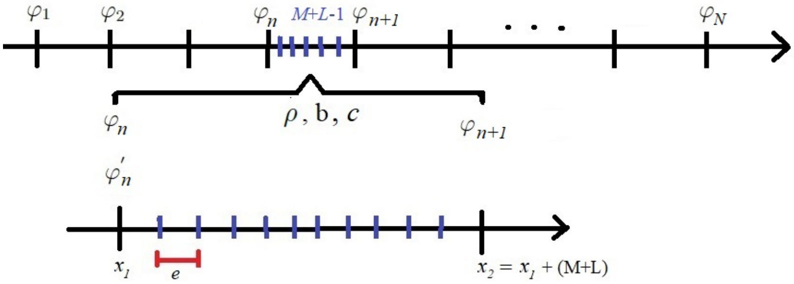

Source: the author.

Now, with respect to boundary conditions, we consider the domain $\Omega = (0, Q)$. The one-dimensional Poisson equation can be expressed as follows:

$$\nabla^2\varphi = \frac{d^2\varphi}{dx^2} = \rho \tag{5.24}$$

where $\partial\Omega = \{(x)|x = 1, 2\}$ and $\rho \subset \mathbb{R}$ is a function called the source term. The Laplacian operator, denoted as ∇^2, is equivalent to $\nabla^2 = \nabla \cdot \nabla$, where ∇ represents the gradient (a measure of a function's variation in each of its variables).

The formulation in Eq. (5.24) is known as the strong formulation in finite element theory, or the original ordinary differential equation (ODE) formulation. However, as FEM can be employed to solve arbitrary ODEs, it is beneficial to first reformulate the ODE into an equivalent form, referred to as the weak formulation. Consequently, the

Poisson problem possesses both a strong and a weak formulation.

The weak formulation essentially represents a rephrased version of the strong form (the original ODE). The final finite element approach is determined based on this weak form (SINGH, 2009). To derive the weak form of ODE Eq. (5.24), we multiply it by an arbitrary function (weight-function), denoted as $a(x)$, and integrate it over Ω, yielding:

$$\int_{\Omega} a\nabla^2\varphi = \int_{\Omega} a\rho \tag{5.25}$$

By defining a function space $A$where all functions are bounded and quadratically integrable, we can derive the global matrix $\boldsymbol{A}$ for each element. The choice of $a(x)$ can be adjusted to enhance results, and we can define operations on these functions within the rules of integration. First, we determine a subspace of A where we can find the solution φ. Considering this solution as $D = \{a \in A(\Omega) : a|_{\partial\Omega} = 0\}$ and letting $\varphi, a \in \Omega$, we carry out the integration in Eq (5.25) according to rule: $\nabla(a\nabla\varphi) = \nabla a \cdot \nabla\varphi + a\nabla^2\varphi$, as follows:

$$\int_{\Omega} a\nabla^2\varphi = \int_{\Omega} \nabla \cdot (a\nabla\varphi) - \int_{\Omega} \nabla a \cdot \nabla\varphi \tag{5.26}$$

Applying Gauss's theorem to $\nabla \cdot (a\nabla\varphi)$, we obtain:

$$\int_{\Omega} \nabla \cdot (a\nabla\varphi) = \int_{\partial\Omega} a\nabla\varphi \cdot \hat{n}\, dx = 0 \tag{5.27}$$

$$\int_{\Omega} a\nabla^2\varphi = -\int_{\Omega} \nabla a \cdot \nabla\varphi \tag{5.28}$$

Subsequently, we obtain:

$$-\int_{\Omega} \nabla a \cdot \nabla\varphi\, dx = \int_{\Omega} a\rho\, dx \tag{5.29}$$

where dx refers to an infinitesimal line segment. Thus, Eq (5.26) reduces to Eq. (5.29), which represents the final weak formulation and is equivalent to the strong formulation. We can reverse the steps and return to the original equation. The primary advantage of the weak formulation is its transformation of the second derivative over φ into two first derivatives over weight a and φ itself.

The weak formulation (5.29) can be discretized using the global matrix (concatenation of all $\boldsymbol{A}_e$ elementary matrices (5.22)) as $\boldsymbol{A}$ and the global vector (concatenation of all $\boldsymbol{b}_e$ elementary vectors (5.23)) as $\boldsymbol{b}$ for all domain Ω. The interpolated solution comprises the points in the vector $\boldsymbol{\varphi}$, which contains the values of the estimated ordinates, as shown below:

$$\boldsymbol{A}\boldsymbol{\varphi} = \boldsymbol{b} \tag{5.30}$$

To clarify the difference between the strong and weak formulations, our motivation for applying the Poisson equation arises from this approach. Considering that the data within the sample space exhibit these dynamics, Eq. (5.29) represents the sampled data of the macrocell channel through the received signal ($\varphi(x)$), and ρ serves as the source to be determined for each subinterval of sampling.

Based on this principle, we need to determine ρ, which can be solved through an ordinary differential equation ($\frac{d^2}{dx^2}$), adhering to the conditions below:

$$\varphi = \frac{\rho x^2}{2} + bx + c \tag{5.31}$$

$$\varphi^{'} = \rho x + b \tag{5.32}$$

$$\varphi^{''} = \rho \tag{5.33}$$

According to Eq. (5.31), Eq. (5.32), and Figure 25, we can establish the following equations within each subinterval:

$$\begin{gathered} \rho x_1^2 + 2bx_1 + 2c = 2\varphi_n \\ \rho x_2^2 + 2bx_2 + 2c = 2\varphi_{n+1} \\ \rho x_1 + b = \varphi_n^{'} \end{gathered} \tag{5.34}$$

Subsequently, we obtain a straightforward system of linear equations to determine ρ:

$$\begin{pmatrix} x_1^2 & 2x_1 & 2 \\ x_2^2 & 2x_2 & 2 \\ x_1 & 1 & 0 \end{pmatrix} \begin{pmatrix} \rho \\ b \\ c \end{pmatrix} = \begin{pmatrix} 2\varphi_n \\ 2\varphi_{n+1} \\ \varphi_n^{'} \end{pmatrix} \tag{5.35}$$

A solution to this problem can be obtained for each subinterval, provided that we know the three conditions specified in Eq. (5.34). In this context, the values of the first two expressions in Eq. (5.35) are predefined, and the third can be assigned at either of the two points. For simplification and approximation of the analytical solution, after identifying the points where the derivative is zero ($\varphi^{'} = 0$) among the N samples, we opt to commence with the local maximum or minimum points closest to the domain's extreme points $\Omega = [1, Q]$.

Once the source value ρ or the subinterval under examination is determined, we employ the FEM solver, which models Poisson's equation, to compute all $(M + L)$ values within that subinterval. For the subsequent subinterval, we use the values of ρ and b previously obtained as solutions to Eq. (5.34) to calculate the new condition for $\varphi_n^{'}$, consequently obtaining the three conditions for that subinterval. This process is iteratively repeated for each subinterval, with the discovery of the source ρ for each initiating the solution of Poisson's equation through FEM, leading to an interpolation closer to the analytical solution.

Algorithm 6 outlines the steps for interpolating the real part using the FEM-Poisson method. A similar procedure is executed for the imaginary part of the Channel Impulse Response (CIR).

Algorithm 6: FEM-Poisson algorithm

```
Input;
// sample abscissa points vector of length N
$\boldsymbol{x}$;
// real part of estimated value of the channel vector in the respective abscissa points
   of length N
$\hat{\boldsymbol{\varphi}}_{Re}$;
// total amount of points to interpolate
$Q$;
Output;
// ordinate vector with the $Q$ values of the interpolation points
$\boldsymbol{\varphi}$;
Initialization;
1. From $\boldsymbol{x}$ and $\hat{\boldsymbol{\varphi}}_{Re}$ extract all the points where the derivative is zero and find the $x_i$ abscissa point closest
  to the extremes points ($x_1$ or $x_Q$);
2. Set the length of the element: $l_e = x_Q - x_{Q-1} = 1$;
Start the forward interpolation;
for $j = i$ to $N - 1$ do
    3. Initialize $\boldsymbol{A}_j$ as an empty matrix, $\boldsymbol{b}_j$ as an empty vector and $\boldsymbol{\varphi}_j$ as an empty vector;
    4. Find $\rho_j$, $b_j$ and $c_j$ this subinterval by computing Eq. (5.35);
    // From $\rho_j$, apply the FEM to solve Poisson's equation and interpolate the $M + L - 1$
       points (nodes)
    for $n = i$ to $(M + L - 1)$ do
        Identify the elements of subinterval: $x_n$ and $x_{n+1}$;
        Compute the elementary matrix $\boldsymbol{A}_{en}$ (5.22) and the elementary vector $\boldsymbol{b}_{en}$ (5.23);
        Update the global matrix $\boldsymbol{A_j} = [\boldsymbol{A}_j \ ; \ \boldsymbol{A}_{en}]$ and the global vector $\boldsymbol{b_j} = [\boldsymbol{b_j} \ ; \ \boldsymbol{b}_{en}]$ ;
    end
    5. Find $\boldsymbol{\varphi}_j$ by computing Eq. (5.30);
    6. Update $\boldsymbol{\varphi} = [\boldsymbol{\varphi} \ ; \ \boldsymbol{\varphi}_j]$ ;
end
Start the backward interpolation;
for $j = i$ to $1$ do
    7. Initialize $\boldsymbol{A}_j$ as an empty matrix, $\boldsymbol{b}_j$ as an empty vector and $\boldsymbol{\varphi}_j$ as an empty vector;
    8. Find $\rho_j$, $b_j$ and $c_j$ this subinterval by computing Eq. (5.35);
    // From $\rho_j$, apply the FEM to solve Poisson's equation and interpolate the $M + L - 1$
       points (nodes)
    for $n = (M + L - 1)$ to $i$ do
        Identify the elements of subinterval: $x_n$ and $x_{n+1}$;
        Compute the elementary matrix $\boldsymbol{A}_{en}$ (5.22) and the elementary vector $\boldsymbol{b}_{en}$ (5.23);
        Update the global matrix $\boldsymbol{A_j} = [\boldsymbol{A}_{en} \ ; \ \boldsymbol{A}_j]$ and the global vector $\boldsymbol{b_j} = [\boldsymbol{b}_{en} \ ; \ \boldsymbol{b_j}]$ ;
    end
    9. Find $\boldsymbol{\varphi}_j$ by computing Eq. (5.30);
    10. Update $\boldsymbol{\varphi} = [\boldsymbol{\varphi}_j \ ; \ \boldsymbol{\varphi}]$ ;
end
```

In the formulation of the mathematical model, the transition from $\nabla^2\varphi = 0$ to $\nabla^2\varphi = \rho$, considering both the real $\{Re\}$ and imaginary $\{Im\}$ parts, is essential. This transition allows for the incorporation of a singularity, reflecting the conjecture that rapid variations occur in the mobile environment while maintaining continuity up to the second derivative of the CIR. Moreover, it introduces a disconnection between h_{Re} and h_{Im}. In essence, various interpolation methods could be applied without considering the inherent nature of the $\varphi(x)$ function. However, the substantiation of the hypothesis regarding the smooth and continuous variation of the function within subintervals, with dynamics that can be effectively described by a Poisson equation, simplifies the problem to the resolution of an Ordinary Differential Equation (ODE) as in (5.24). This ODE can be efficiently tackled using one-dimensional Finite Element Method (FEM). This approach stands in contrast to a purely data-driven interpolation, which can become considerably more complex due to the open treatment of data in each subinterval and the disregard for the inherent nature of the problem. In Section 5.3, we present the results of our study.

5.3 Results and Discussion

Utilizing the parameters detailed in Table 11, we implement OTFS modulation within a SISO system operating under a macrocell channel, employing 4-QAM and 16-QAM constellations. To detect data, we employ approximating message passing (AMP-FO), MMSE, and ZF, utilizing the received signal $\boldsymbol{y}$ and the estimated effective channel $\hat{\boldsymbol{H}}_{eff}$. We then compare the outcomes under two scenarios: the first assumes a known channel (ideal case), while the second relies on the channel estimation through the spline method and the FEM.

Table 11 – Simulation Parameters for Macrocell Estimation

Parameter	Value
Carrier frequency (f_c)	4 GHz
Subcarrier spacing (Δf)	15 kHz
Number of subcarriers (M)	600
Number of symbols (N)	12
CP length (L)	255
Channel model	Urban macrocell
Maximum delay (l_τ)	50
Modulation scheme	4-QAM and 16-QAM
UE speed	330 km/h
Channel estimation	FEM and Spline
Pilot position ($x_p[l_p, k_p]$)	$x_p[300, 6]$
Guard interval ($[l, k]$)	$[(l_p + l_\tau)$-$(l_p - l_\tau), \forall k]$

Source: the author.

Before delving into the BER vs SNR results to assess the system's performance using the spline and FEM methods, we find it insightful to demonstrate the quality of CIR approximation achieved by these methods. We particularly focus on the most complex case involving 16-QAM modulation, examining both the real and imaginary parts of the CIR. This is evident in 26 and 27, respectively.

Figure 26 – Real part interpolation using 16-QAM

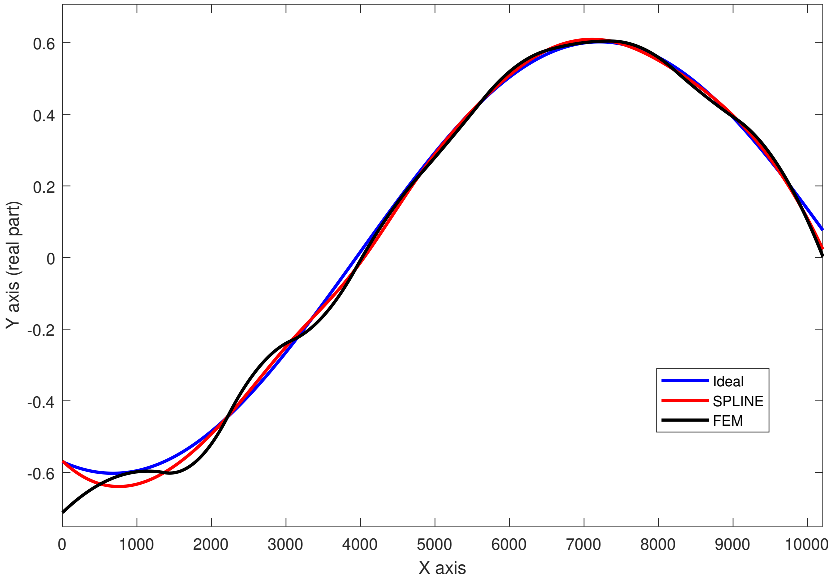

Source: the author.

As observed in Figures 26 and 27, the CIR estimation obtained through the spline and FEM methods closely aligns with the known (ideal) channel. Nonetheless, both methods exhibit slightly larger errors at the extreme points, as they attempt to

Figure 27 – Imaginary part interpolation using 16-QAM

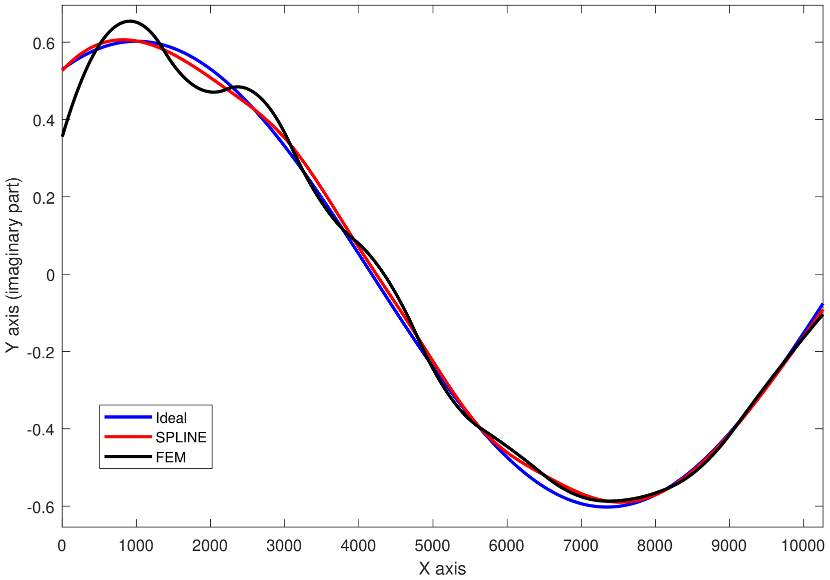

Source: the author.

estimate without full knowledge of the function behavior at those specific locations. Nevertheless, the values remain comparable to the ideal case.

This context helps us better appreciate the quality of approximation achieved by these methods in relation to the system's performance. Figure Figure 28 illustrates the performance comparison among MMSE (dashed line), ZF (continuous line), and AMP-FO (dotted line) for both known channel conditions (blue line) and channels estimated using the spline (red line) and FEM (black line). The system configuration assumes $M = 600$ subcarriers, $N = 12$ symbol numbers, CP lenght $L = 255$ and a maximum delay $l_\tau = 150$. This analysis is based on 1000 frames for each SNR value, ranging from 5 to 25 dB.

In Fig. 28, it is evident that the BER curves achieved using FEM or spline estimation closely match the curve obtained using the known channel. An exception is the curve using the ZF detection method, which is a straightforward method that does not adapt to the SNR used. The highlighted area indicates that spline interpolation outperforms FEM, albeit the difference in results is on the order of 10^{-3}. This justifies the use of the one-dimensional FEM-Poisson method since it is practical and less complex, involving first-degree equations compared to the cubic degree used in spline interpolation.

Figure 28 – BER Performance considering $M = 600$, $N = 12$, $L = 255$ 4-QAM

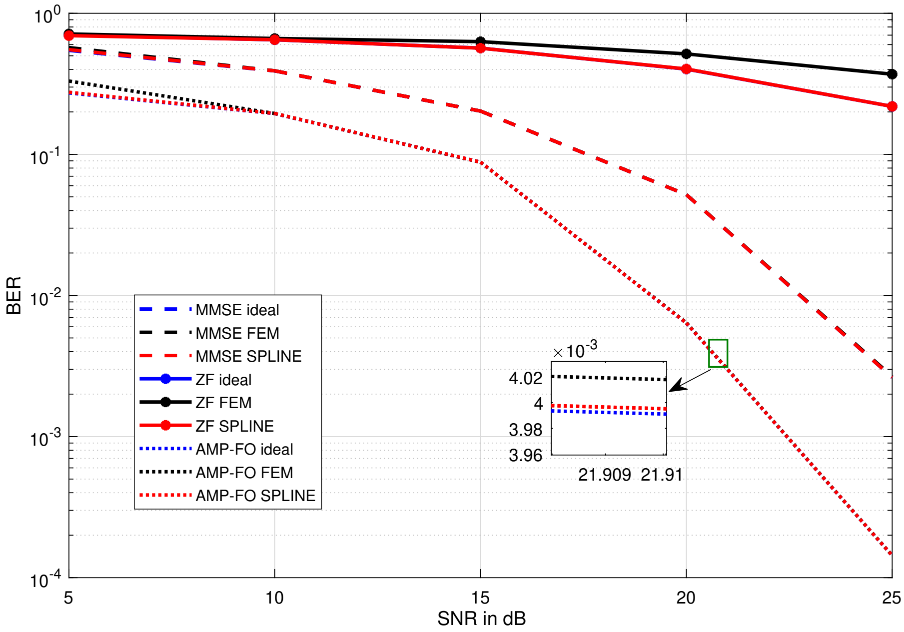

Source: the author.

Regarding data detection methods, AMP-FO performs better than MMSE and ZF, with a BER difference of approximately 10^{-2} between 20 and 25 dB SNR. This result supports the use of AMP-FO in OTFS modulation, as it accounts for channel sparsity and employs an iterative method to refine node means and variances, all while being less complex, as demonstrated in Chapter 4.

To assess the approximation quality of the estimated channels obtained via FEM and spline interpolation compared to the original channel, we employ the NMSE measure, as shown in Eq. (5.36) below, with the results presented in Figures 29 and 31, for 4-QAM and 16-QAM, respectively.

$$NMSE = \frac{||\boldsymbol{H}_{eff} - \hat{\boldsymbol{H}}_{eff}||^2}{||\boldsymbol{H}_{eff}||^2} \tag{5.36}$$

where $\hat{\boldsymbol{H}}_{eff}^{MN \times MN}$ is estimated effective matrix.

Figure 29 confirms that spline interpolation provides a superior estimation compared to FEM, achieving an NMSE of 10^{-5} from 10 dB onwards. In contrast, FEM-Poisson maintains an NMSE of 10^{-4}, still considered a good channel estimation, albeit with a 10^{-1} difference at the same SNR level. However, spline interpolation reaches an

Figure 29 – NMSE measure to channel estimation for system $M = 600$, $N = 12$, $L = 255$, 4-QAM

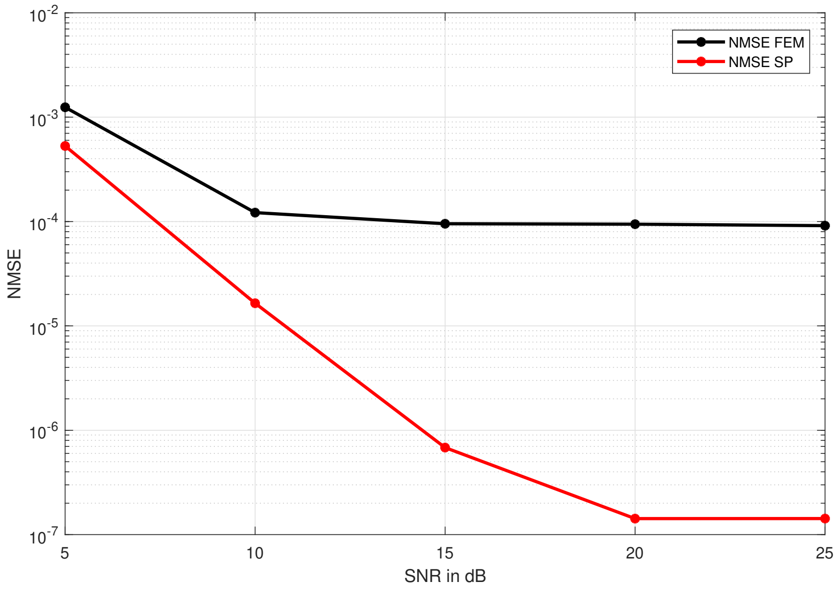

Source: the author.

order greater than 10^{-6} from 15 dB, whereas the FEM method saturates at 10^{-4}.

A similar analysis for a 16-QAM constellation is presented in Figure 30, demonstrating that the BER performance is lower than that of 4-QAM due to the increased complexity. For example, at 25dB SNR, AMP-FO achieves a BER of 10^{-4}, while it reaches about 10^{-3} for 16-QAM.

Comparing to Figure 29, Figure 31 depicts the NMSE results for channel estimation using spline and FEM with the 16-QAM constellation. Here, FEM reaches an NMSE saturation of about 10^{-4} from 20dB, while spline interpolation maintains an approximation order of 10^{-7} at 20dB. Notably, the NMSE measure is less influenced by constellation size, with differences primarily attributed to the CIR estimation of components using the threshold-based method.

Considering the favorable NMSE results and the similarity between the BER performance of the proposed FEM-Poisson method, spline interpolation, and the known channel, it is apparent that these methods offer performance close to the ideal case. However, with the inclusion of guard intervals and pilots within the QAM symbol arrangement on the delay-Doppler grid, the number of effective symbols is impacted, leading to increased BER. Performance calculations consider only the data bits, which represent the useful data in this context.

Figure 30 – BER Performance considering $M = 600$, $N = 12$, $L = 255$, 16-QAM

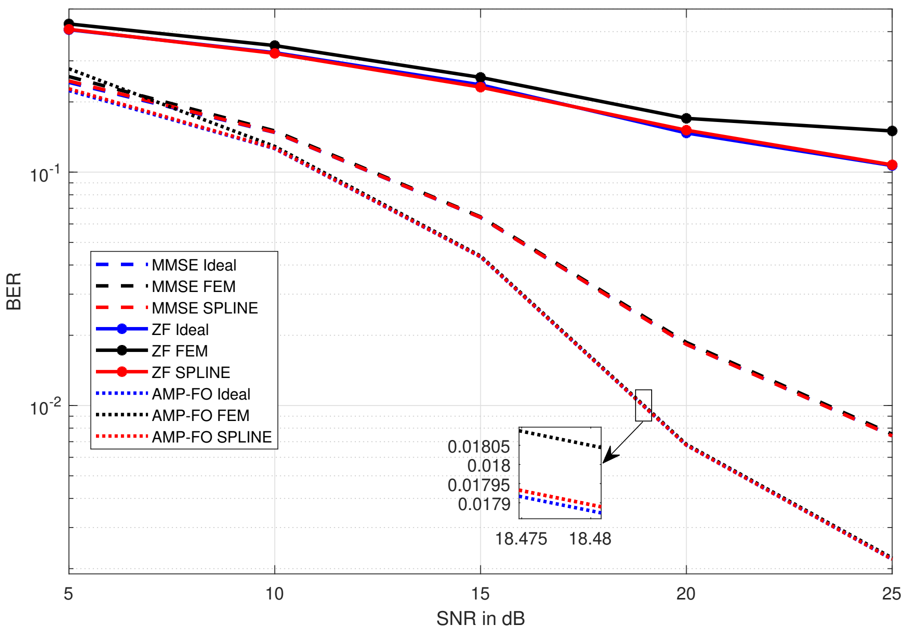

Source: the author.

Figure 31 – NMSE measure to channel estimation for system $M = 600$, $N = 12$, $L = 255$, 16-QAM

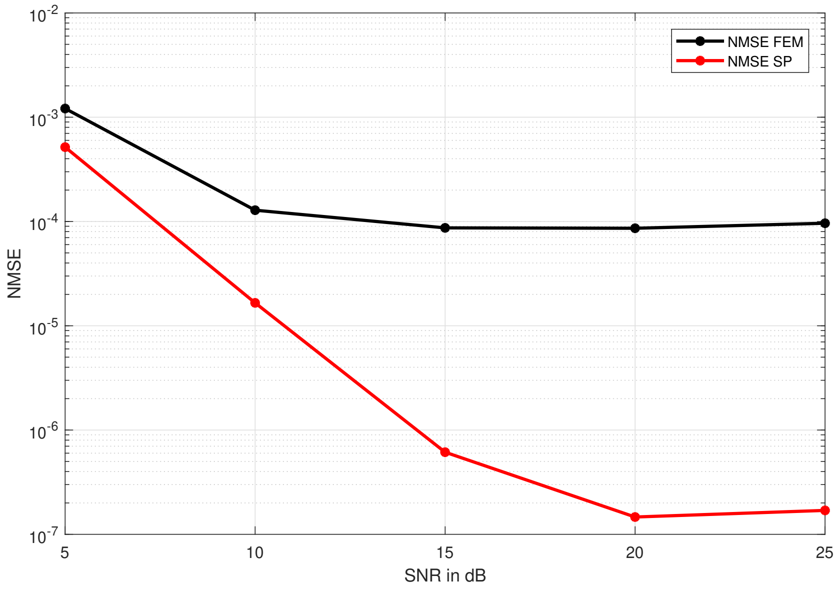

Source: the author.

6 CONCLUSIONS

6.1 Final considerations

Throughout this thesis, we have extensively investigated, evaluated, and compared four low-complexity MPA-based detectors designed for OTFS systems operating over time-frequency selective channels with high Doppler effects, focusing on BER performance and complexity analysis. As anticipated, the MPA and AMP-EP algorithms exhibit the best BER performance. However, the AMP-FO algorithm offers significantly lower complexity, amounting to only about 30$\%$ of the AMP-EP algorithm's complexity. In fact, the AMP-FO algorithm is the least complex among the studied algorithms, yet it results in a BER performance degradation of less than 1 dB and 2.25 dB at BER $= 10^{-3}$ when compared to the AMP-EP and MPA algorithms, respectively. Consequently, the AMP-FO algorithm gives the best performance-complexity trade-off in both SISO-OTFS and MIMO-OTFS systems.

Regarding channel estimation, the proposed one-dimensional FEM-Poisson method has demonstrated strong NMSE approximations, achieving a difference of approximately 10^{-4} in the coefficients of the original channel. While spline interpolation yields better estimation results, the choice of the FEM-Poisson method is justified by its reduced complexity. It transitions from a computational complexity of cubic order to a one-dimensional approach, exclusively involving ODE solutions. Considering the level of approximation provided by these methods, the BER results align closely with the MMSE and AMP-FO detectors, with the latter exhibiting superior performance.

6.2 Future opportunities

6.2.1 Channel estimation using Compressive Sensing

As previously mentioned, practical high-speed channel estimation presents challenges associated with fractional Doppler effects. In this context, channel estimation techniques based on compressive sensing (CS) have gained prominence (SHEN *et al.*, 2019; ZHANG *et al.*, 2018). For instance, authors in (GAUDIO *et al.*, 2022) have employed the Least Absolute Shrinkage and Selection Operator (LASSO), which is equivalent to l_1-norm regularization via least squares minimization. They used a sensing matrix that exploits channel sparsity and employed a soft-thresholding iterative algorithm.

Another approach involves channel estimation in the presence of fractional Doppler effects in the delay-Doppler domain through a deterministic pilot design, as proposed in (SHI *et al.*, 2021). This method relies on a deterministic pilot matrix structure to reduce pilot overhead, with a modified sensing matrix-based channel estimation (MSMCE) algorithm used to obtain channel estimation based on Channel State Information (CSI) acquisition.

6.2.2 Selection vector estimation techniques

Initially, it was believed that organizing the symbol vector $\boldsymbol{x}$ as $\boldsymbol{Az}$ would result in significantly improved performance when using a simple adaptive estimator such as LMS for data detection compared to MMSE. However, such assumption did not hold. The primary advantage of LMS lies in its ability to provide estimations without requiring matrix inversion. Yet, the effective channel matrix in OTFS modulation is rather large, typically $MN \times MN$. The reduction in complexity, however, impacts estimation quality. Therefore, the next steps include investigating a better tradeoff between the step factor's value and the number of iterations for LMS. Additionally, exploring other LMS variations, such as the Normalized LMS (NLMS) (KANEKO; YUKAWA, 2020) and the Proportionate Normalized LMS (PNLMS) (DUTTWEILER, 2000), as well as examining other least squares-based solutions, such as Alternating Least Square (ALS) (ZACHARIAH *et al.*, 2012) and Recursive Least Square (RLS) (BHOTTO; ANTONIOU, 2013).

Achieving an improvement in data detection using a known channel will pave the way for effective estimation of the effective channel matrix, with it being rearranged as a channel vector to ensure compatibility with the implemented algorithm. Subsequently, exploring blind channel estimation and data estimation techniques will be a natural progression.

6.2.3 Applications filtering in OTFS

Filtering has been a key technique for reducing side lobes in waveforms. In OFDM, several filtering methods have been applied to enhance spectral efficiency without significantly affecting performance, such as the ones described in (FARHANG-

BOROUJENY, 2011) and (FAULKNER, 2000). Post-OFDM waveforms, such as Filter Bank-based Multi-Carriers (FBMC) (BELLANGER *et al.*, 2010), Universal-Filtered OFDM (UF-OFDM) or Universal-Filtered Multicarrier (UFMC) (WILD *et al.*, 2013), sub-band filtering of the zero prefix (ZP)-OFDM (VAKILIAN *et al.*, 2014) and filtered OFDM (f-OFDM) (ABDOLI *et al.*, 2015) have been proposed to reduce out-of-band energy.

Given that OTFS can be seen as a modified OFDM system with preprocessing and postprocessing steps, it is worth exploring how different types of filtered OFDM could impact OTFS.

REFERENCES

ABDOLI, J.; JIA, M.; MA, J. Filtered OFDM: a new waveform for future wireless systems. In: **IEEE 16th International Workshop on Signal Processing Advances in Wireless Communications (SPAWC)**. Stockholm, Sweden: IEEE, 2015. p. 66–70.

AL., C. L. et. Intelligent blind source separation technology based on OTFS modulation for LEO satellite communication. **China Communications**, v. 19, n. 7, p. 89–99, 2022.

AL-JZARI, A.; IVIVA, K. Cyclic prefix length determination for orthogonal frequency division multiplexing system over different wireless channel models based on the maximum excess delay spread. **American Journal of Engineering and Applied Sciences**, v. 8, n. 1, p. 82–93, 2015.

AL., R. H. et. Orthogonal time frequency space (otfs) modulation for millimeter-wave communications systems. In: **2017 IEEE MTT-S International Microwave Symposium (IMS)**. Honololu, HI, USA: IEEE, 2017. p. 681–683.

ALBATAINEH, Z.; HAYAJNEH, K.; SALAMEH, H.; DANG, C.; DAGMSEH, A. Robust massive MIMO channel estimation for 5G networks using compressive sensing technique. **International Journal of Electronics and Communications**, v. 120, p. 1–7, 2020.

ALBREEM, M. A.; JUNTTI, M.; SHAHABUDDIN, S. Massive MIMO detection techniques: a survey. **IEEE Transactions on Information Theory**, v. 14, n. 8, p. 1–24, 2019.

AN, C.; RYU, H. G. High throughput mobile communication based on OTFS system with the delay-Doppler compensation. **Wireless Personal Communications**, v. 106, p. 473–486, 2019.

ANJU; AHLAWAT, A. A review on orthogonal frequency division multiplexing (OFDM). **International Journal of Recent Research Aspects**, v. 3, n. 2, p. 112–115, 2016.

ANN, P.; PREENU; JOSE, R. Comparison of PAPR reduction techniques in OFDM systems. In: **2016 International Conference on Communication and Electronics Systems (ICCES)**. Coimbatore, India: IEEE, 2016. p. 1–5.

ARORA, M.; GUPTA, A. PAPR reduction in OFDM systems using higher order prediction filter. In: **11th International Conference on Intelligent Systems and Control (ISCO)**. Coimbatore, India: IEEE, 2017. p. 306–310.

BAHAI, A. R. S.; SALTZBERG, B. R. **Multi-carrier digital communications**: theory and applications of OFDM. [*New York*]: Kluwer Academic/Plenum Publishers, 1999.

BARTELS, R. H.; BEATTY, J. C.; BARSKY, B. A. **An introduction to splines for use in computer graphics and geometric modelling**. [*San Mateo, CA*]: Elsevier Science, 1998.

BELLANGER, M.; RENFORS, M.; IHALAINEN, T.; ROCHA, C. A. F. OFDM and FBMC transmission techniques: a compatible high performance proposal for broadband power line communications. In: **IEEE - ISPLC2010**. Rio de Janeiro, Brazil: IEEE, 2010. p. 154–159.

BHOTTO, M. Z. A.; ANTONIOU, A. New improved recursive least-squares adaptive-filtering algorithms. **IEEE Transactions on Circuits and Systems I: Regular Papers**, v. 60, n. 6, p. 1548–1558, 2013.

BLAZEK, T.; RADOVIC, D. Performance evaluation of otfs over measured v2v channels at 60 ghz. In: **2020 IEEE MTT-S International Conference on Microwaves for Intelligent Mobility (ICMIM)**. [S.l.]: IEEE, 2020. p. 1–4.

BOCUS, M. J.; DOUFEXI, A.; AGRAFIOTIS, D. Performance of OFDM-based massive MIMO OTFS systems for underwater acoustic communication. **IET Communications**, v. 14, n. 4, p. 588–593, 2019.

BROWN, J.; CHURCHILL, R. **Complex Variables and Applications**. [*California*]: McGraw-Hill Education, 2009. (Brown and Churchill series).

CAO, B.; XIANG, Z.; REN, P. Low complexity transmitter precoding for MU MIMO-OTFS. **Digital Signal Processing**, v. 115, p. 1–9, 2021.

CARMON, Y.; SHAMAI, S.; WEISSMAN, T. Comparison of the achievable rates in OFDM and single carrier modulation with i.i.d. inputs. **IEEE Transactions on Information Theory**, v. 61, n. 4, p. 1795–1818, 2015.

CHANG, R. W.; GIBBY, R. A. A theoretical study of an orthogonal multiplexing data transmission scheme. **IEEE Trans. on. Communications**, v. 16, n. 4, p. 529–540, 1968.

CHENG, J.; GAO, H.; XU, W. **Low-complexity linear equalizers for OTFS exploiting two-dimensional fast Fourier transform**. 2019. Arxiv. Available at: <https://arxiv.org/pdf/1904.02783v1.pdf>. Accessed on: 15 Apr. 2020.

CHENG, J.; JIA, C.; GAO, H.; XU, W.; BIE, Z. **OTFS based receiver scheme with multi-antennas in high-mobility V2X systems**. 2020. Arxiv. Available at: <https://arxiv.org/pdf/2003.01400.pdf>. Accessed on: 12 Jan. 2022.

CHO, Y. S.; YONSEI, J. K.; YANG, W. Y.; KANG, C. G. **MIMO-OFDM wireless communications with Matlab**. [*Noida, India*]: John Wiley Sons, 2010.

CRUZ-ROLDáN, F.; MARTINS, W. A.; GARCíA, F.; MOONEN, M.; DINIZ, P. S. R. **Intersymbol and intercarrier interference in OFDM systems: unified formulation and analysis**. 2020. Arxiv. Available at: <https://doi.org/10.48550/arXiv.2012.04527>. Accessed on: 15 Feb. 2021.

CURSI, E. S.; SAMPAIO, R. **Uncertainty Quantification and stochastic modeling with Matlab**. London: elsevier, 2015.

DAS, S. S.; RANGAMGARI, V.; S.TIWARI; MONDAL, S. C. Time domain channel estimation and equalization of CP-OTFS under multiple fractional dopplers and residual synchronization errors. **IEEE Access**, v. 9, p. 10561–10576, 2020.

DEHKORDI, S. K.; GAUDIO, L.; KOBAYASHI, M.; COLAVOLPE, G.; CAIRE, G. Beam-space MIMO radar with OTFS modulation for integrated sensing and communications. In: **2022 IEEE International Conference on Communications Workshops (ICC Workshops)**. Seoul, Republic of Korea: IEEE, 2022. p. 509–514.

DEKA, K.; THOMAS, A.; SHARMA, S. **OTFS-NOMA based on SCMA**. 2020. Arxiv. Available at: <https://arxiv.org/pdf/2005.03216.pdf>. Accessed on: 15 Jul. 2021.

DEKA, K.; THOMAS, A.; SHARMA, S. OTFS-SCMA: a code-domain NOMA approach for orthogonal time frequency space modulation. **IEEE Transactions on Communications**, v. 69, n. 8, p. 5043–5058, 2021.

DING, Z. Robust beamforming design for OTFS-NOMA. **IEEE Open Journal of the Communications Society**, v. 1, p. 33–40, 2020.

DING, Z.; SCHOBER, R.; FAN, P.; VINCENT, H. OTFS-NOMA: an efficient approach for exploiting heterogenous user mobility profiles: an efficient approach for exploiting heterogenous user mobility profiles. **IEEE Transactions on Communications**, v. 67, n. 11, p. 7950–7965, 2019.

DINIZ, P. S. R.; MARTINS, W. A.; LIMA, M. V. S. **Block transceivers**: OFDM and beyond. [S.l.]: William Tranter, 2012.

DIXIT, S.; KATIYAR, H. Performance of OFDM in time selective multipath fading channel in 4G systems. In: **IEEE 2015 Fifth International Conference on Communication Systems and Network Technologies**. [S.l.]: IEEE, 2015. p. 421–424.

DUTTWEILER, D. L. Proportionate normalized least-mean-squares adaptation in echo cancelers. **IEEE Transactions on Speech and Audio Processing**, v. 8, n. 5, p. 508–518, 2000.

ENKU, Y. K.; BAI, B.; WAN, F.; GUYO, C. U.; TIBA, I. N. Two-dimensional convolutional neural network-based signal detection for OTFS systems. **IEEE Wireless Communications Letters**, v. 10, n. 11, p. 2514–2518, 2021.

ERCEG, e. a. V. Channel models for fixed wireless applications. In: **IEEE transaction**. [S.l.]: IEEE, 2001. p. 1–36.

FARHANG-BOROUJENY, B. OFDM versus filter bank multicarrier. **IEEE Sig. Proc. Mag.**, v. 28, n. 3, p. 92–112, 2011.

FAULKNER, M. The effect of filtering on the performance of OFDM systems. **IEEE Trans. Veh. Tech.**, v. 49, n. 5, p. 1877–1884, 2000.

GAUDIO, L. **Multi-carrier modulations over sparse channels: communication, channel estimation, and radar sensing** 2022. 160f. Phd Thesis (PhD Thesis) — Fakultat IV: Elektrotechnik und Informatik, University of Parma, 2022.

GAUDIO, L.; COLAVOLPE, G.; CAIRE, G. OTFS vs. OFDM in the presence of sparsity: a fair comparison. **IEEE Transactions for Wireless Communicationns**, v. 21, n. 6, p. 4410–4423, 2022.

GAUDIO, L.; KOBAYASHI, M.; BISSINGER, B.; CAIRE, G. Performance analysis of joint radar and communication using OFDM and OTFS. In: **2019 IEEE International Conference on Communications Workshops (ICC Workshops)**. Shanghai, China: IEEE, 2019. p. 1–6.

GAUDIO, L.; KOBAYASHI, M.; CAIRE, G.; COLAVOLPE, G. On the effectiveness of OTFS for joint radar parameter estimation and communication. **IEEE Transactions on Wireless Communicationns**, v. 19, n. 9, p. 5951–5965, 2022.

GE, Y.; DENG, Q.; CHING, P. C.; DING, Z. Receiver design for OTFS with a fractionally spaced sampling approach. **IEEE Transactions on Wireless Communications**, v. 20, n. 7, p. 4072–4086, 2021.

GERZAGUET, R.; BARTZOUDIS, N.; BALTAR, L. G. The 5G candidate waveform race: a comparison of complexity and performance. **EURASIP Journal on Wireless Communications and Networking**, v. 13, p. 1–14, 2017.

GHOSH, A.; ZHANG, J.; ANDREWS, J. G.; MUHAMED, R. **Fundamentals of LTE**. [S.l.]: Prentice Hall, 2010.

GOLDSMITH, A. **Wireless communications**. [*New York, USA*]: Cambridge University Press, 2005.

GOLUB, G. H.; LOAN, C. F. V. **Matrix computations**. [*London, UK*]: The Johns Hopkins University Press, 1996.

GOPALA, K.; SLOCK, D. Doppler compensation and beamforming for high mobility OFDM transmissions in multipath. In: **EURECOM**. Sophia-Antipolis, France: [s.n.], 2014. p. 1–13.

GOPIKRISHNAN, C.; VENKATACHALAM, S.; MANIGANDAN, T. Design and performance analysis of OFDM system. **International Journal of Computing Science and Communication Technologies**, v. 2, n. 1, p. 349–352, 2009.

GUPTA, P.; MEHRA, D. K. A novel technique for channel estimation and equalization for high mobility OFDM systems. **Wireless Pers Commun.**, v. 49, p. 613–631, 2008.

GóMEZ-CUBA, F. Compressed sensing channel estimation for OTFS modulation in non-integer delay-Doppler domain. In: **2021 IEEE Global Communications Conference (GLOBECOM)**. Atlanta, GA, USA: IEEE, 2021. p. 1–6.

HADANI, R.; MONK, A. **OTFS: a new generation of modulation addressing the challenges of 5G**. 2018. Arxiv. Available at: <https://arxiv.org/ftp/arxiv/papers/1802/1802.02623.pdf>. Accessed on: 12 Sep. 2019.

HADANI, R.; RAKIB, S.; TSATSANIS, M.; MONK, A.; GOLDSMITH, A.; MOLISCH, A.; CALDERBANK, R. Orthogonal time frequency space modulation. In: **IEEE 29th Annual International Symposium on Personal, Indoor, and Mobile Radio Communications (PIMRC)**. San Francisco, USA: IEEE, 2017. p. 1558–2612.

HARDAS, B. M.; POKLEB, S. B. Optimization of peak to average power reduction in OFDM. **Journal of Communications Technology and Electronics**, v. 62, n. 12, p. 1388–1395, 2017.

HARDAS, M.; POKLE, B. Optimization of peak to average power reduction in OFDM. **Journal of Communications Technology and Electronics**, v. 62, n. 12, p. 1388–1395, 2017.

HASHIMOTO, N.; OSAWA, N.; YAMAZAKI, K.; IBI, S. Channel estimation and equalization for CP-OFDM-based OTFS in fractional Doppler channels. In: **2021 IEEE International Conference on Communications Workshops (ICC Workshops)**. [S.l.]: IEEE, 2021. p. 1–7.

HAYKIN, S.; MOHER, M. **Modern wireless communication**. [*New Jersey*]: Pearson Prentice Hall, 2005.

HE, Q.; SCHMEINK, A. Comparison and evaluation between FBMC and OFDM systems. In: **19th International ITG Workshop on Smart Antennas**. Ilmenau, Germany: VDE, 2015. p. 1–7.

JAIN, R. Channel models: a tutorial. In: **Wimax Forum**. [S.l.: s.n.], 2007. p. 1–21.

JING, L.; ZHANG, N.; HE, C.; J.SHANG; LIU, X.; YIN, H. OTFS underwater acoustic communications based on passive time reversal. **Applied Acoustics**, v. 185, p. 1–8, 2022.

JOHNSON, C. **Numerical solution of ODEs by the finite element method**. [*New York*]: Cambridge University Press, 1988.

KANEKO, H.; YUKAWA, M. Normalized least-mean-square algorithms with minimax concave penalty. In: **ICASSP 2020 - 2020 IEEE International Conference on Acoustics, Speech and Signal Processing (ICASSP)**. [S.l.]: IEEE, 2020. p. 5445–5449.

KESKIN, M. F.; WYMEERSCH, H.; ALVARADO, A. **Radar sensing with OTFS: embracing ISI and ICI to surpass the ambiguity barrier**. 2021. Arxiv. Available at: <https://arxiv.org/abs/1802.00929.pdf>. Accessed on: 20 Feb. 2022.

KIM, M.; LEE, W.; CHO, D. A novel PAPR reduction scheme for OFDM system based on deep learning. **IEEE Communications Letters**, v. 22, n. 3, p. 510–513, 2018.

KOSASIH, A.; QU, X.; HARDJAWANA, W.; YUE, C.; VUCETIC, B. **Bayesian neural network detector for an orthogonal time frequency space modulation**. 2022. Arxiv. Available at: <https://arxiv.org/pdf/2206.13235v1.pdf>. Accessed on: 10 Jul. 2022.

KOSHIBA, M. **Optical waveguide theory by the finite element method**. [*Tokyo*]: KTK Scientific Publishers, 1993.

KSCHISCHANG, F. R.; FREY, B. J.; LOELIGER, H.-A. Factor graphs and the sum-product algorithm. **IEEE Transactions on Information Theory**, v. 47, n. 2, p. 498–519, 2001.

LI, F.; YUAN, Z.; GUO, Q.; WANG, Z.; SUN, P. Message passing-based structured sparse signal recovery for estimation of OTFS channels with fractional doppler shifts. **IEEE Transactions on Wireless Communications**, v. 20, n. 12, p. 7773–7785, 2021.

LI, J.; KAVEHRAD, M. Effects of time selective multipath fading on OFDM systems for broadband mobile applications. **IEEE Commun. Lett.**, v. 3, p. 332–334, 1999.

LI, L.; XIAO, L.; ZHANG, X.; LIU, G.; LI, S.; JIANG, T. An efficient symbol-by-symbol aided expectation propagation detector for otfs with index modulation. In: **2017 IEEE Wireless Communications Letters**. [S.l.]: IEEE, 2022. p. 1–5.

LI, M.; ZHANG, S.; GE, Y.; GAO, F.; FAN, P. Joint channel estimation and data detection for hybrid ris aided millimeter wave otfs systems. **IEEE Transactions on Communications**, p. 1–17, 2022.

LI, Y. G.; WINTERS, J. H.; SOLLENBERGER, N. R. MIMO-OFDM for wireless communications: signal detection with enhanced channel estimation. **IEEE Transactions on Communications**, v. 50, n. 9, p. 1471–1477, 2002.

LIU, F.; Z.YUAN; GUO, Q.; WANG, Z.; SUN, P. Multi-block UAMP-based detection for OTFS with rectangular waveform. **IEEE Wireless communications Letters**, v. 11, n. 2, p. 323–327, 2022.

LIU, L. Comprehensive study on coded modulation schemes for future communication. **IOP Conf. Series: Materials Science and Engineering**, v. 782, p. 1–10, 2020.

LONG, F.; NIU, K.; LIN, J. Low complexity block equalizer for otfs based on expectation propagation. **IEEE Wireless Communications Letters**, v. 11, n. 2, p. 376–380, 2022.

MA, Y.; MA, G.; WANG, N.; ; ZHONG, Z.; AI, B. OTFS-TSMA for massive internet of things in high-speed railway. **IEEE Transactions on Wireless Communications**, v. 21, n. 1, p. 519–531, 2022.

MACDONALD, V. H. The cellular concept. **The Bell systems technical journal**, v. 58, n. 1, p. 15–43, 1979.

MALIK, P. K.; TRIPATHI, M. P. OFDM: A mathematical review. **Journal on Today's Ideas – Tomorrow's Technologies**, v. 5, n. 2, p. 97–111, 2017.

MISHRA, H. B.; SINGH, P.; PRASAD, A. K.; BUDHIRAJA, R. OTFS channel estimation and data detection designs with superimposed pilots. **IEEE Transactions on Wireless Communications**, v. 21, n. 4, p. 2258–2274, 2022.

MURALI, K. R.; CHOCKALINGAM, A. **On OTFS modulation for high-doppler fading channels**. 2017. Arxiv. Available at: <https://arxiv.org/abs/1802.00929.pdf>. Accessed on: 10 Sep. 2019.

NESS, R.; LINNARTZ, J.; PERRE, L. V. der; ENGELS, M. **Wireless OFDM systems**: how to make them work? [*New York*]: Springer, 2002.

NOBLE, D. The history of land-mobile radio communications. In: **IEEE vehicular technology transactions**. [S.l.]: IEEE, 1962. p. 1406–1416.

NOGUEIRA, L. R.; MOTA, J.; RUYET, D. L.; CURSI, E. S. de. Noise, channel and message identification on MIMO channels with general noise. In: **5th International Symposium on Uncertainty Quantification and Stochastic Modelling**. [S.l.]: Springer, 2020. p. 1–36.

PAN, J. Cramer-rao low bound of channel estimation for orthogonal time frequency space modulation system. **IEEE Trans. Veh. Tech.**, v. 70, n. 10, p. 9646–9658, 2021.

PATENT 3488445. **Orthogonal frequency division multiplexing**: United States Patent. USA, 1970.

PATENT EP2346223. **Calculation of log-likelihood ratios in a demodulator**: European patent application. Duisburg (DE), 2011.

PATRA, J. P.; SINGH, P. Efficient signal detection methods for high mobility OFDM system with transmit diversity. **Arabian Journal for Science and Engineering**, v. 44, p. 1769–1778, 2017.

PINA, H. **Métodos numéricos**. [S.l.]: Escolar Ed., 2010.

POLYCARPOU, A. C. **Introduction to the finite element method in electromagnetics**. [*San Rafael, CA*]: Morgan Claypool, 2006.

PRASAD, R.; NEE, R. V. **OFDM for wireless multimidia communications**. [S.l.]: Artech House, 2000.

PROAKIS, J. G.; SALEHI, M. **Digital communications**. [*New York*]: McGraw-Hill, 2008.

R1- 1610397. **OTFS PAPR analysis**: 3GPP TSG RA WG1 Meeting. Lisbon, Portugal, 2002.

RAMACHANDRAN, M. K.; CHOCKALINGAM, A. MIMO-OTFS in high-doppler fading channels: signal detection and channel estimation. In: **2018 IEEE Global Communications Conference**. Abu Dhabi, United Arab Emirates: IEEE, 2018. p. 206–212.

RAPPAPORT, T. S. **Wireless communications**: principles and practice. [S.l.]: Prentice Hall, 2002.

RAVITEJA, e. a. P. Interference cancellation and iterative detection for orthogonal time frequency space modulation. **IEEE Trans. Wireless Commun.**, v. 17, n. 10, p. 6501 – 6515, 2018.

RAVITEJA, P.; HONG, Y.; VITERBO, E.; BIGLIERI, E. Practical pulse-shaping waveforms for reduced-cyclic-prefix OTFS. **IEEE Transactions on Vehicular Technology**, v. 68, n. 1, p. 957–961, 2018.

RAVITEJA, P.; PHAN, K. T.; HONG, Y. **Embedded pilot-aided channel estimation for OTFS in delay-Doppler channels**. 2019. Arxiv. Available at: <https://doi.org/10.48550/arXiv.1808.08360>. Accessed on: 27 Apr. 2020.

RAVITEJA, P.; PHAN, K. T.; HONG, Y.; VITERBO, E. **Low-complexity iterative detection for orthogonal time frequency space modulation**. 2017. Arxiv. Available at: <https://arxiv.org/pdf/1709.09402.pdf>. Accessed on: 25 Apr. 2020.

RAVITEJA, P.; PHAN, K. T.; HONG, Y.; VITERBO, E. Orthogonal time frequency space (OTFS) modulation based radar system. In: **2019 IEEE Radar Conference (RadarConf)**. Boston, MA, USA: IEEE, 2019. p. 1–6.

RAVITEJA, P.; PHAN, K. T.; JIN, Q.; HONG, Y.; VITERBO, E. Low-complexity iterative detection for orthogonal time frequency space modulation. In: **2018 IEEE Wireless Communications and Networking Conference (WCNC)**. Barcelona, Spain: IEEE, 2018. p. 1–6.

REYHANI, A. R.; FARHANG, A.; JI, M.; CHEN, R. R.; FARHANG-BOROUJENY, B. **Analysis of discrete-time MIMO OFDM-based orthogonal time frequency space modulation**. 2017. Arxiv. Available at: <https://arxiv.org/abs/1710.07900v1.pdf>. Accessed on: 30 Jun. 2019.

ROHLING, H. **OFDM**: concepts for future communication systems. [*New York*]: Springer, 2011.

SCHUMAKER, L. L. **Spline functions basic theory**. [*New York*]: Cambridge University Press, 2007.

SHAH, D.; RINDHE, B.; NARAYANKHEDKAR, S. Effects of cyclic prefix on OFDM system. In: **International Conference and Workshop on Emerging Trends in Technology**. New York: ACM, 2010. p. 420–424.

SHAN, Y.; WANG, F. **Low-complexity and low-overhead receiver for OTFS via large-scale antenna array**. 2020. Arxiv. Available at: <https://arxiv.org/pdf/2005.07910v1.pdf>. Accessed on: 18 Jan. 2021.

SHEN, W.; DAI, L.; AN, J.; FAN, P.; HEATH, R. W. Channel estimation for orthogonal time frequency space (OTFS) massive MIMO. **IEEE Transactions on Signal Processing**, v. 67, n. 16, p. 4204–4217, 2019.

SHI, D.; WANG, W.; YOU, L.; SONG, X.; HONG, Y.; GAO, X.; FETTWEIS, G. **Deterministic pilot design and channel estimation for downlink massive MIMO-OTFS systems in presence of fractional Doppler**. 2021. Arxiv. Available at: <https://arxiv.org/pdf/2105.09628v1.pdf>. Accessed on: 22 Dez. 2021.

SHI, J.; HU, J.; YUE, Y.; XUE, X.; LIANG, W.; LI, Z. Outage probability for OTFS based downlink LEO satellite communication. **IEEE Transactions of Vehicular Technology**, v. 71, n. 3, p. 3355–3360, 2022.

SINGH, G. **Short introduction to finite element method**. [*Norwerge*]: Norwergian University of Science and Technology, 2009.

SOLíN, P. **Partial differential equations and the finite element method**. [*New Jersey*]: Willey, 2005.

SOM, P.; DATTA, T.; SRINIDHI, N.; CHOCKALINGAM, A.; RAJAN, B. S. Low-complexity detection in large-dimension MIMO-ISI channels using graphical models. **IEEE J. Sel. Topics in Signal Processing**, v. 5, n. 8, p. 1497–1511, 2011.

SOULEYMANE, B.; MONDOL, S. I.; WEI, Z. Comparative performance study of LS and MMSE channel estimation over time varying channel in OFDM system. **International Journal of Engineering Research Technology (IJERT)**, v. 5, n. 3, p. 847–850, 2016.

SRIVASTAVA, S.; SINGH, R. K.; JAGANNATHAM, A. K.; CHOCKALINGAM, A. Otfs transceiver design and sparse doubly-selective csi estimation in analog and hybrid beamforming aided mmwave mimo systems. **IEEE Transactions on Wireless Communications**, p. 1–15, 2022.

TAROKH, V.; ALAMOUTI, S. M.; KOIVUNEN, V.; KIM, K. MIMO-OFDM and its application. **Journal of communications and Networks**, v. 9, n. 2, p. 109–111, 2007.

THAJ, T.; VITERBO, E. **Low complexity iterative rake detector for orthogonal time frequency space modulation**. 2020. Arxiv. Available at: <https://arxiv.org/pdf/2001.10703v1.pdf>. Accessed on: 5 Oct. 2021.

TIWARI, S.; DAS, S. S. **Circularly pulse shaped orthogonal time frequency space modulation**. 2019. Arxiv. Available at: <https://arxiv.org/pdf/1910.10457.pdf>. Accessed on: 22 Aug. 2021.

TIWARI, S.; DAS, S. S.; RANGAMGARI, V. Low complexity LMMSE receiver for OTFS. **IEEE Communications Letters**, v. 23, n. 12, p. 2205–2209, 2019.

TSE, D.; VISWANATH, P. **Fundamentals of wireless communication**. [S.l.]: Cambridge University Press, 2004.

TUSHA, A.; ALTHUNIBAT, S.; HASNA, M. O.; QARAQE, K.; ARSLAN, H. Exploiting user diversity in OTFS transmission for beyond 5G wireless systems. **IEEE Wireless Communications Letters**, v. 11, n. 8, p. 1689–1693, 2022.

VAKILIAN, V.; WILD, T.; SCHAICH, F.; BRINK, S. T.; FRIGON, J. F. 5G air interface design based on universal filtered (UF-)OFDM. In: **Int. Conf. Dig. Sig. Proc. (DSP)**. Hong Kong, China: IEEE, 2014. p. 699–704.

WANG, T.; FAN, S.; CHEN, H.; XIAO, Y.; GUAN, X.; SONG, W. Generalized approximate message assing detector for GSM-OTFS systems. **IEEE Access**, v. 10, p. 22997–23007, 2022.

WEI, Z.; YUAN, W.; LI, S.; YUAN, J.; NG, D. W. Transmitter and receiver window designs for orthogonal time-frequency space modulation. **IEEE Transactions on Communications**, v. 69, n. 4, p. 2207–2223, 2021.

WEN, M.; LI, Q.; CHENG, X. **Index modulation for OFDM communications systems**. [*Singapore*]: Spinger, 2021.

WIFFEN, F.; SAYER, L.; BOCUS, M.; DOUFEXI, A.; NIX, A. Comparison of OTFS and OFDM in ray launched sub-6 GHz and mmwave line-of-sight mobility channels. In: **2018 IEEE 29th Annual International Symposium on Personal, Indoor and Mobile Radio Communications (PIMRC)**. Bologna-Italy: IEEE, 2018. p. 73–79.

WILD, T.; SCHAICH, F.; CHEN, Y. Universal-filtered multi-carrier technique for wireless systems beyond LTE. In: **IEEE Globecom Workshops**. Atlanta, GA, USA: IEEE, 2013. p. 223–228.

WU, S.; KUANG, L.; NI, Z.; LU, J.; HUANG, D.; GUO, Q. Low-complexity detection for large-scale multiuser MIMO-OFDM systems using approximate message passing. **IEEE Journal Sel. Topics in Signal Processing**, v. 8, n. 5, p. 902–915, 2014.

WU, Z.; ANDREW, J.; GUO, X.; JAY, Y. OTFS-based joint communication and sensing for future industrial IoT. **IEEE Internet of Things Journal**, p. 1–1, 2021.

YALCIN, M.; AKAN, A.; DOGAN, H. Low-complexity channel estimation for OFDM systems in high-mobility fading channels. **Elec. Eng. Comp. Sci.**, v. 20, n. 4, p. 583–592, 2008.

YUAN, W.; LI, S.; WEI, Z.; YUAN, J.; NG, D. W. K. Data-aided channel estimation for OTFS systems with a superimposed pilot and data transmission scheme. **IEEE Wireless Communications Letters**, v. 10, n. 9, p. 1954–1958, 2021.

YUAN, W.; WEI, Z.; LI, S.; YUAN, J.; NG, D. K. Integrated sensing and communication-assisted orthogonal time frequency space transmission for vehicular networks. **IEEE Journal of Selected Topics in Signal Processing**, v. 15, n. 6, p. 1515–1528, 2021.

YUAN, W.; WEI, Z.; YUAN, J.; NG, D. K. **A simple variational Bayes detector for orthogonal time frequency space (OTFS) modulation**. 2019. Arxiv. Available at: <https://arxiv.org/pdf/1911.12538v1.pdf>. Accessed on: 01 Mar. 2020.

YUAN, X. **Comb-type pilot-aided OFDM channel estimation for underground WLAN communications** 2007. 107f. Phd Thesis (PhD Thesis) — Faculte des Sciences et de Génie: génie électrique, University of Laval, 2007.

ZACHARIAH, D.; SUNDIN, M.; JANSSON, M.; CHATTERJEE, S. Alternating least-squares for low-rank matrix reconstruction. **IEEE Signal Processing Letters**, v. 19, n. 4, p. 231–234, 2012.

ZEMEN, T.; HOFER, M.; LOESCHENBRAND, D. **Low-complexity equalization for orthogonal time and frequency signaling (OTFS)**. 2017. Arxiv. Available at: <https://arxiv.org/pdf/1710.09916v1.pdf>. Accessed on: 4 Aug. 2019.

ZHANG, M.; WANG, F.; YUAN, X.; CHEN, L. 2D structured turbo compressed sensing for channel estimation in OTFS systems. In: **2018 IEEE International Conference on Communication Systems (ICCS)**. [S.l.]: IEEE, 2018. p. 45–49.

ZHANG, Y.; LIU, H. Impact of time-selective fadingon the performance of quasi-orthogonal space-timecoded OFDM systems. **IEEE Trans. Commun.**, v. 54, p. 251–260, 2006.

ZHOU, Z.; LIU, L.; XU, J.; CALDERBANK, R. Learning to equalize OTFS. **IEEE Transactions Wireless Communications**, v. 21, n. 9, p. 7723–7736, 2022.

APPENDIX A – VETORIAL ANALYSIS FOR OFDM

In subsection 3.3.1 for OTFS standalone, following the same steps, with the exception of the OTFS transforms (ISFFT/SFFT) processing, we obtain an analysis for a modified OFDM modulation to derive the $\boldsymbol{H}_{eff}$ expression for OFDM. The process unfolds as follows:

Starting at the transmitter, and excluding the OTFS transform step, we have the following:

$$\boldsymbol{S}_{ofdm} = \boldsymbol{F}_M^H \boldsymbol{G}_{tx} \boldsymbol{X} = \boldsymbol{G}_{tx} \boldsymbol{X} \boldsymbol{F}_N^H, \tag{A.1}$$

In the case of applying a rectangular pulse, we can treat $\boldsymbol{G}_{tx}$ as an identity matrix of size M ($\boldsymbol{I}_M$). Therefore, $\boldsymbol{S}_{ofdm} = \boldsymbol{F}_M^H \boldsymbol{X}$. By utilizing the corollary $vec(\boldsymbol{AB}) = (\boldsymbol{I} \otimes \boldsymbol{A})\boldsymbol{b}$ o, a property of the Kronecker product, we can derive the vector $\boldsymbol{s}_{ofdm}$, as follows:

$$\boldsymbol{s}_{ofdm} = vec(\boldsymbol{F}_M^H \boldsymbol{X}) = (\boldsymbol{I} \otimes \boldsymbol{F}_M^H)\boldsymbol{x}, \tag{A.2}$$

Afterward, the $\boldsymbol{s}_{ofdm}$ signal traverses the channel and experiences the addition of AWGN noise:

$$\begin{aligned} \boldsymbol{r}_{ofdm} &= \boldsymbol{H}\boldsymbol{s}_{ofdm} + \boldsymbol{w} \\ &= \boldsymbol{H}(\boldsymbol{I} \otimes \boldsymbol{F}_M^H)\boldsymbol{x} + \boldsymbol{w}, \end{aligned} \tag{A.3}$$

By applying OFDM demodulation to the $\boldsymbol{r}_{ofdm}$ signal, considering $\boldsymbol{G}_{tx} = \boldsymbol{G}_{rx} = \boldsymbol{I}$ and the matrix $\boldsymbol{R}_{ofdm} = invec(\boldsymbol{r}_{ofdm})$, we obtain :

$$\begin{aligned} \boldsymbol{Y}_{ofdm} &= \boldsymbol{F}_M \boldsymbol{G}_{rx} \boldsymbol{R}_{ofdm} \\ &= \boldsymbol{F}_M \boldsymbol{R}_{ofdm}, \end{aligned} \tag{A.4}$$

Applying the corollary in A.4 to $vec(\boldsymbol{Y}_{ofdm})$, we have:

$$\boldsymbol{y}_{ofdm} = (\boldsymbol{I} \otimes \boldsymbol{F}_M)\boldsymbol{r}_{ofdm} \tag{A.5}$$

$$\begin{aligned} &= (\boldsymbol{I} \otimes \boldsymbol{F}_M)[\boldsymbol{H}(\boldsymbol{I} \otimes \boldsymbol{F}_M^H)\boldsymbol{x} + \boldsymbol{w}] \\ &= (\boldsymbol{I} \otimes \boldsymbol{F}_M)\boldsymbol{H}(\boldsymbol{I} \otimes \boldsymbol{F}_M^H)\boldsymbol{x} + (\boldsymbol{I} \otimes \boldsymbol{F}_M)\boldsymbol{w} \\ &= \boldsymbol{H}_{eff}^{ofdm}\boldsymbol{x} + \hat{\boldsymbol{w}}, \end{aligned} \tag{A.6}$$

where $\boldsymbol{H}_{eff}^{ofdm}$ represents the effective channel matrix for OFDM, and $\hat{\boldsymbol{w}} = (\boldsymbol{I} \otimes \boldsymbol{F}_M)\boldsymbol{w}$.

APPENDIX B – DATA DETECTION USING THE UNCERTAINTY QUANTIFICATION APPROACH IN OTFS

In the Single-Input Single-Output (SISO) case with OTFS modulation, we have classically processed the general received signal Eq. (3.16) during the first year for data detection and performance evaluation, utilizing the classic processing model $\boldsymbol{y} = \boldsymbol{H}\boldsymbol{x} + \boldsymbol{w}$. In the Uncertainty Quantification (UQ) approach for data detection in OTFS, we employ the concept of a selection matrix and a source vector to process the vector symbols $\boldsymbol{y}$, as outlined in (NOGUEIRA *et al.*, 2020). The source vector $\boldsymbol{a}$ encompasses every possible symbol combination for a specific constellation, such as Quadrature Amplitude Modulation (QAM). In the context of 4-QAM modulation, the source vector $\boldsymbol{a}^{4\times 1}$ is defined as follows:

$$\boldsymbol{a} = [(-1+j)\ \ (-1-j)\ \ (1+j)\ \ (1-j)]^T. \tag{B.1}$$

Subsequently, based on the vector symbols $\boldsymbol{x}^{MN\times 1}$, we construct the selection matrix $\boldsymbol{Z}^{MN\times 4}$, inserting the number 1 in the position corresponding to the respective QAM symbol in each row, with the other values in each row set to zero. As a result, it possesses certain properties: the elements of each row sum up to 1, and the elements are limited to $\in \{0, 1\}$. With this, we rewrite $\boldsymbol{x}$ as follows:

$$\boldsymbol{x} = \boldsymbol{Z}\boldsymbol{a}, \tag{B.2}$$

One plausible solution for data detection is to treat this problem as a least squares problem. In this scenario, instead of finding the selection matrix $\boldsymbol{Z}$, we obtain the selection vector z in terms of the vectorized version of $\boldsymbol{Z}$, as follows:

$$\boldsymbol{x} = \boldsymbol{A}\boldsymbol{z}, \tag{B.3}$$

where $\boldsymbol{A}$ contains every possible symbol combination for a specific constellation QAM, distributed in diagonal blocks.

By expanding Eq. (3.16) into its real ($\{Re\}$) and imaginary ($\{Im\}$) parts, as outlined in (CURSI; SAMPAIO, 2015), we arrive at:

$$\begin{bmatrix} \boldsymbol{y}_{re} \\ \boldsymbol{y}_{im} \end{bmatrix} = \begin{bmatrix} \boldsymbol{H}_{re} & -\boldsymbol{H}_{im} \\ \boldsymbol{H}_{im} & \boldsymbol{H}_{re} \end{bmatrix} \begin{bmatrix} \boldsymbol{A}_{re} & -\boldsymbol{A}_{im} \\ \boldsymbol{A}_{im} & \boldsymbol{A}_{re} \end{bmatrix} \begin{bmatrix} \tilde{\boldsymbol{z}}_{re} \\ \tilde{\boldsymbol{z}}_{im} \end{bmatrix} + \begin{bmatrix} \boldsymbol{w}_{re} \\ \boldsymbol{w}_{im} \end{bmatrix} \tag{B.4}$$

In this context, instead of detecting all symbol vectors $\boldsymbol{x}$ as per conventional methods, we determine the most likely $\tilde{\boldsymbol{z}}_{re}$, as $\tilde{\boldsymbol{z}}_{im}$ is a vector of zeros, by solving a quadrically constrained least squares problem, akin to a Least Mean Squares (LMS) adaptive filter.

Rewriting Eq. (3.16) and considering the expansion in (B.4) for the 4-QAM constellation, we have:

$$\begin{aligned} \boldsymbol{y} &= \boldsymbol{H}\boldsymbol{x} + \widetilde{\boldsymbol{w}} \\ &= \boldsymbol{H}\boldsymbol{A}\boldsymbol{z} + \widetilde{\boldsymbol{w}} \\ &= \boldsymbol{B}\boldsymbol{z} + \widetilde{\boldsymbol{w}}, \end{aligned} \tag{B.5}$$

where $\boldsymbol{z}^{8MN\times 1}$ represents a selection vector for 4-QAM and where $\boldsymbol{B} = \boldsymbol{H}\boldsymbol{A}$ of size $2MN \times 8MN$.

Utilizing the LMS algorithm to estimate $\boldsymbol{z}$ under the assumption that the channel is known, the received signal $\boldsymbol{y} = \boldsymbol{B}\boldsymbol{z} + \widetilde{\boldsymbol{w}}$ serves as the basis for computing the cost function J:

$$\begin{aligned} J &= \frac{1}{2}||\boldsymbol{e}||^2 = \frac{1}{2}||\boldsymbol{y} - \hat{\boldsymbol{y}}||^2 \\ &= \frac{1}{2}||\boldsymbol{y} - \boldsymbol{B}\hat{\boldsymbol{z}}||^2. \end{aligned} \tag{B.6}$$

where $\hat{\boldsymbol{z}}^{8MN\times 1}$ is estimated selection vector.

Taking into account the estimated vector $\hat{\boldsymbol{y}} = \boldsymbol{B}\hat{\boldsymbol{z}}$, the estimated selection vector is updated as follows:

$$\begin{aligned} \hat{\boldsymbol{z}}^{t+1} &= \hat{\boldsymbol{z}}^t - \mu \nabla J^t \\ &= \hat{\boldsymbol{z}}^t - \mu \frac{\partial J^t}{\partial \hat{\boldsymbol{z}}^t} \\ &= \hat{\boldsymbol{z}}^t - \mu \frac{\partial J^t}{\partial \boldsymbol{e}^t} \frac{\partial \boldsymbol{e}^t}{\partial \hat{\boldsymbol{y}}^t} \frac{\partial \hat{\boldsymbol{y}}^t}{\partial \hat{\boldsymbol{z}}^t} \\ &= \hat{\boldsymbol{z}}^t - \mu \boldsymbol{e}^t (-1) \boldsymbol{B}^t \\ &= \hat{\boldsymbol{z}}^t + \mu (\boldsymbol{B}^T)^t \boldsymbol{e}^t. \end{aligned} \tag{B.7}$$

where t denotes the iteration number, $(.)^T$ represents the transport matrix and ∇J is the gradient of the cost function. In our simulation, we set the step factor $\mu = 0.005$ and the iteration number t = 500.

Subsequently, considering that the imaginary part of the selection vector $\boldsymbol{z}$ consists of zeros, we impose this restriction on the reception stage to reduce estimation complexity. Now that all values are treated as real, we apply the second restriction, ensuring that the sum of each row in the selection matrix $\boldsymbol{Z}$ is 1. In the real part of the selection vector $\boldsymbol{z}$, we set the maximum value to 1, and the other values are set to zero.

For comparison purposes, we also compute an estimated vector $\hat{\boldsymbol{z}}$ based on the estimation from Eq. (B.5) without noise, i.e., applying the zero forcing technique, yielding:

$$\begin{aligned} \boldsymbol{y} &= \boldsymbol{B}\hat{z} \\ \boldsymbol{B}^H\boldsymbol{y} &= \boldsymbol{B}^H\boldsymbol{B}\hat{\boldsymbol{z}} \\ \hat{\boldsymbol{z}} &= (\boldsymbol{B}^H\boldsymbol{B})^{-1}\boldsymbol{B}^H\boldsymbol{y}. \end{aligned} \tag{B.8}$$

However, since the matrix $(\boldsymbol{B}^H\boldsymbol{B})$ is singular, rendering it non-invertible, to compensate for the neglected noise effects in Eq. B.5, we adopt a strategy akin to the Minimum Mean Square Error (MMSE) estimator to compute $\hat{\boldsymbol{z}}$. This is expressed as: $\hat{\boldsymbol{z}} = (\frac{\sigma_v^2}{\sigma_d^2}\boldsymbol{I} + \boldsymbol{B}^H\boldsymbol{B})^{-1}\boldsymbol{B}^H\boldsymbol{y}$. One notable advantage of the LMS algorithm is that it obviates the need for matrix inversion, thereby reducing complexity.

In conclusion, we compare the performance obtained through these methods with the results from traditional Wiener processing using the MMSE estimator. The results are presented in Figure 32.

The LMS_z curve represents the performance obtained using the estimated selection vector $\boldsymbol{z}$ $(\boldsymbol{y} = \boldsymbol{HAz} + \boldsymbol{w})$ from the LMS algorithm. Notably, we achieve slightly better results compared to the MMSE estimator up to an SNR of 15 dB. Above 15 dB, the LMS performance starts to deteriorate, and at an SNR of 20 dB, the MMSE performance reaches an order of 10^{-4} while the LMS performance stands at 10^{-3}.

Figure 32 – BER Performance with estimation vector z

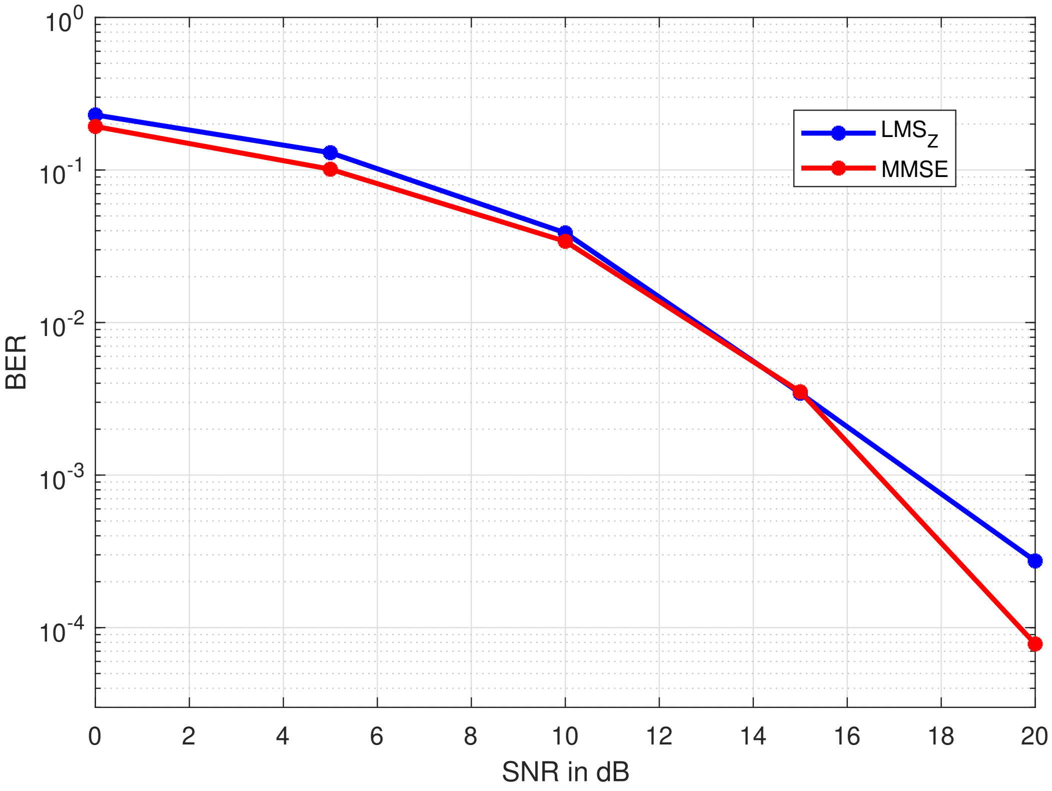

Source: the author.

The obtained results motivate further exploration of solutions based on least square methods to enhance the estimation of the selection vector and reduce complexity in data detection.

APPENDIX C – THRESHOLD METHOD

The threshold method, based on (RAVITEJA *et al.*, 2019), provides a straightforward approach to determine the taps of the time-varying channel. Consider the $MN \times 1$ vector $\boldsymbol{y}$, which represents the signal received in the delay-Doppler domain of the OTFS system, following the removal of the cyclic prefix (CP) and the application of the OFDM and SFFT demodulator.

To execute the threshold method, a single pilot must be transmitted with higher energy compared to the other data symbols and with a guard length sufficient to facilitate its identification within this length. In our approach, we consider scanning the pilot symbols from the respective delay position at which the pilot was transmitted up to the guard length, which is associated with the maximum delay l_τ considered and spans the entire time domain. This entails considering all positions of k. Thus, we consider $k \in \{0, 1, \ldots, N-1\}$ and $l \in \{l_p, l_p+1, \ldots, l_\tau\}$.

Upon converting the vector $\boldsymbol{y}$ into a matrix, we obtain $\boldsymbol{Y}$ with dimensions $M \times N$, where the M rows pertain to the delay positions l and the N columns correspond to positions k. By considering $y[l,k]$ as the coefficient of the matrix $\boldsymbol{Y}$, we define a channel tap if, for the pilot delay position l_p, $|y[l,k]| \geq \Upsilon$. We then adopt the entire row to estimate the N samples of the channel coefficients, as follows:

$$\hat{h}[l - l_p, \forall k] = y[l,k]/x_p. \tag{C.1}$$

where $x_p = x[l_p, k_p]$ represents the coefficient value of the pilot position of transmitted symbols on delay-Doppler grid, and $l - l_p = l_i$ signifies the channel tap of the estimated channel, as defined in Eq. (3.11).

The threshold value Υ is influenced by variations in detection and, therefore, relies on the choice of a pilot with ample energy for easy identification by the method. In this thesis, we consider a pilot with 20 dB more energy than the evaluated SNR and the same threshold as adopted in (RAVITEJA *et al.*, 2019): $\Upsilon = 3\sigma_d^2$

As the OTFS channel takes the form of a square matrix with dimensions $(M+L)N$, we obtain the from the $k \implies N$ samples of each estimated delay point. Subsequently, we proceed with an interpolation process to estimate the $M+L$ intermediate values among the N sampled points from the channel.

APPENDIX D – ESTIMATION OF COMPLEX FUNCTIONS

The methods employed are grounded in Cauchy's Theorem (BARTELS *et al.*, 1998), , which applies to analytic or holomorphic functions of the form: $f(z) = f_R(x,y) + jf_I(x,y)$, where:

a) $z = x + jy$, $x, y \in \mathbb{R}$ and j is the imaginary part: $j^2 = -1$;

b) $f_R(x,y)$ and $f_I(x,y)$ are real functions;

c) $\oint_c f(z)dz = 0$, where c by definition is the boundary in the domain of the Cartesian plane R;

d) The Cauchy-Riemann conditions hold true in R;

e) As a result of item d), it is possible to show that: $\nabla^2 f_R(x,y) = 0$ and $\nabla^2 f_I(x,y) = 0$.

Given these conditions (a-e), it is confirmed that $f(z)$, $f_R(x,y)$, and $f_I(x,y)$ exhibit smooth behavior (without poles) within the region R, indicating the absence of singularities or poles within this domain. Drawing an association between the estimated channel function $h(z)$ and $f(z)$, such that $h_R(x,y) = f_R(x,y)$ and $h_I(x,y) = f_I(x,y)$, it is possible to conjecture that $h(z)$ is a continuous and smooth function concerning x and y. Therefore, the function $\hat{h}(z) = \hat{h}_R(x,y) + j\hat{h}_I(x,y)$ is the estimated version of $h(z)$ and can be obtained through an interpolation method.

Various numerical methods are available to obtain $\hat{h}(z)$, including discretization of (c), utilizing the known values of $h(z)$ on the boundary c of R, $z \in R$. In practice, the points z' over c where $h(z')$ is known can be leveraged to derive $\hat{h}(z), z \in R$. It is worth noting that functions of systems $g(z)$ with singularities or poles within the observed $z = z_0$ domains can be estimated using numerical methods rooted in the Cauchy integral formula, where $g(z) = \frac{f(z)}{z-z_0}$, $f(z)$ analytic:

f) $f(z_0) = \frac{1}{2\pi j}\oint_c \frac{f(z)}{z-z_0}dz$, $z_0 \in R$, and their derivatives in $z_0 \in R$ (PINA, 2010):

g) $f^{(n)}(z_o) = \frac{1}{2\pi j}\oint_c \frac{f(z)}{(z-z_0)^{n+1}}dz$, and using the Taylor series over $f(z)$:

h) $f(z) = \sum_{n=0}^{\infty} a_n(z-z_0)^n$, $a_n = \frac{1}{n!}f^n(z_0)$.

Analytical solutions can be approximated by addressing the Laplace equation, assuming constant or non-existent independent variables. In this context, considering item (e), we express $\frac{d^2 f_R}{dx^2} = 0$ and the same conditions apply to y. Alternative solutions for f_R and f_I encompass linear functions whose slopes depend on specified (known) points or initial boundary conditions.

Importantly, known values of the functions highlight significant variations within certain areas of the observation domain, suggesting the presence of singularities in these regions. These singularities can be represented in a mathematical model, introducing localized or persistent perturbations in the Laplace equation within the regions R, $\in \mathbb{R}$, denoted as :

i) Punctual or impulsive perturbations: $\frac{d^2 g_R(x)}{dx^2} = a\delta(x - x_0)$ and $\frac{d^2 g_I(x)}{dx^2} = b\delta(x - x_0)$, a and b are constants $\in \mathbb{R}$ and $\delta(x)$ is an impulsive function, x_0 represents a point with solution in linear functions.

ii) Persistent perturbations: $\frac{d^2 g_R(x)}{dx^2} = a$ and $\frac{d^2 g_I(x)}{dx^2} = b$, a and b are constants $\in \mathbb{R}$ whose solutions are obtained from quadratic functions, $g_R(x)$ and $g_I(x)$.

The observation domain can comprise several subdomains associated, interconnected through known points. The precision of interpolating functions is enhanced if values of derivatives are known at these points or if these values are equal, ensuring smoother transitions between adjacent subdomains. The accuracy of estimation also hinges on the geometric dimensions of these subdomains, determined by the number of known points.

The perturbed solutions of the Laplace equation, of impulsive or persistent types, lead to linear or parabolic functions within each observation subdomain. Other localized perturbations give rise to different types of functions, which can be generalized and represented by: $g_R(x) = \sum_{n \in \mathbb{Z}} g_R(nx_s) i_R(\frac{x - nx_s}{x_s})$, $x \in \mathbb{R}$, the same for imaginary part: $g_I(x) = \sum_{n \in \mathbb{Z}} g_I(nx_s) i_I(\frac{x - nx_s}{x_s})$, here $i_R(x)$ or $i_I(x)$ are interpolating functions belonging to a Hilbert space, for the case of uniformly distributed points, with spacing $x_s \in \mathbb{R}$, and $i_R(x)$ or $i_I(x)$ equals: 1 for $x = 0$ and 0 for $x = nx_s$, with $n \neq 0$ and $\in \mathbb{Z}$. A similar expression is derived for non-uniform spacing.

The finite element method, for example, is aligned with this approach. It considers factors such as the regularity of interpolating functions, the fulfillment of boundary conditions (or nodes), and the careful selection of the trade-off between subdomain dimensions, interpolating functions, and the convergence of approximation errors.